TENMAK BOR ARAŞTIRMA ENSTİTÜSÜ
TENMAK BORON RESEARCH INSTITUTE

ISSN: 2149-9020
e-ISSN: 2667-8438

BOR DERGİSİ
JOURNAL OF BORON

CİLT/VOL 06 | SAYI/ISSUE 02 | YIL/YEAR 2021

boren

ISSN: 2149-9020
e-ISSN: 2667-8438

BOR DERGİSİ

JOURNAL OF BORON

CİLT VOL **06** **SAYI** ISSUE **02** **YIL** YEAR **2021**

Sorumlu Yazı İşleri Müdürü
Manager of Publication
Dr. Sedat Sürdem
Enstitü Başkan V.
e-mail: sedat.surdem@tenmak.gov.tr

Editoryal Teknik Personel/Editorial Technical Staff
Dr. Abdulkadir Solak
Sema Akbaba
Sinem Erdemir Guran

Yayıncı/Publisher
TENMAK Bor Araştırma Enstitüsü (BOREN)

Yayın İdare Adresi/Adress of Publication Manager
Dumlupınar Bulvarı (Eskişehir Yolu 7. km), No:166, D Blok,
06530, Ankara, Türkiye
Tel: (0312) 201 36 00
Fax: (0312) 219 80 55
boren.journal@tenmak.gov.tr
https://dergipark.org.tr/boron

Yayın Türü/Type of Publication: Yaygın süreli yayın
Yayın Aralığı/Range of Publication: 3 Aylık
Basım Tarihi/Publication Date: 30/06/2021
Matbaa/Printing: Kuban Matbaacılık Yayıncılık

ANKARA
HAZİRAN 2021 / JUNE 2021

BOR DERGİSİ
JOURNAL OF BORON
https://dergipark.org.tr/boron

İÇİNDEKİLER/CONTENTS

BOR DERGİSİ
JOURNAL OF BORON
https://dergipark.org.tr/boron

A Comparative study on the effect of acute toxicity of nano and micro boron particles in *Lemna minor* (Linneaus 1753)

Yeşim Dağlıoğlu[1*], Sevda Türkiş[2]

[1]Ordu University, Department of Molecular Biology and Genetics, Ordu, 52200, Turkey
ORCID orcid.org/0000-0001-8740-1162
[2]Ordu University, Faculty of Education, Department of Primary Education, Ordu, 52200, Turkey
ORCID orcid.org/0000-0002-1853-8437

ARTICLE INFO

Article History:
Received April 26, 2020
Accepted April 4, 2021
Available online June 30, 2021

Research Article

DOI: 10.30728/boron.727172

Keywords:
Antioxidant activity
Boron
Lipid peroxidation
Nanoparticles
Oxidative stress

ABSTRACT

In recent years, research on the fate of engineering nanoparticles on plants and their toxicity mechanisms have indicated that there are knowledge gaps and significant uncertainties. In this study, the toxicity, physiological effects, and basic factors of nano and micro boron particles treated to duckweed (*Lemna minor*) under experimental conditions were investigated. This study reports that the chlorophyll concentration of treated nano boron is higher than the control group and the treated micro boron. Malondialdehyde and superoxide dismutase levels were recorded higher in micro boron. Catalase and hydrogen peroxide level was recorded higher in nano boron. Pearson's correlation analysis indicated negative correlations between hydrogen peroxide and malondialdehyde levels in all doses of nano boron; Positive correlations were found between malondialdehyde and catalase levels at 100 mgL^{-1} of micro boron. As the concentration of the treated nano boron increased, the rate of accumulation in the leaf tissues of duckweed decreased. On the contrary, micro boron was observed to be the opposite. When all these data are evaluated, it is understood that micro boron is more toxic than nano boron.

1. Introduction

The behaviors of nanoparticles (NPs) in different environmental risks, such as natural waters, sediment, and soils are complex. Once in the environment, NPs suffer transformations such as aggregation that can affect ecotoxicity [1-4]. Today, there are many types of NPs and their industrial uses have increased rapidly. Consequently, the potential biological effect and environmental end of NPs raise concerns. In the last decades, scientists have investigated nanoparticle ecotoxicity to learn more about the risks and benefits of NPs [4].The likelihood of exposure of plants to NPs has increased with the use of NPs in a production of various tools and goods [5-6]. The access of the NPs to the plants is through direct application, accidental release, contaminated soil/sedimentation, or atmospheric precipitation. As plants interact strongly with atmospheric, terrestrial and aquatic environments, they are exposed to NPs [7]. Based on the literature, it has been stated that properties such as the uptake, displacement, and accumulation of NPs in plants depend on the size, type, chemical compound, functionality, and determination of the NPs [6,8,9]. In addition, the plant cell wall serves as a barrier for any foreign substance, including NPs can not easily enter the plant cells since the pore diameter is between 5-20 nm [10]. However, by affecting cell walls, NPs can cause the formation of large and new pores that allow large NPs to pass through the cell wall [11,12]. Thus, NPs or NP aggregates can easily pass through the cell walls and reach plasma membranes as they have a smaller diameter than the pore diameter of the cell walls [13,14].

The world's boron (B) minerals' (about 230 kinds of) approximately 62% of reserves are in Turkey. B compounds having a very wide and widespread use area are increasingly used. It is used in a wide variety of areas, from fertilizer to the pharmaceutical industry, from cleaning material to the nuclear industry [15]. In recent years, boron has become a more popular field of use and has a a broad range of practices in protective coatings, high-density fuels, cancer treatments, and semiconductor fields [16,17]. So, plants are exposed to B at a higher rate. The beneficial role of Micro B against plant growth was recorded in earlier studies. The most important role that bor plays in plant metabolism is the protection of hormone levels [18]. Although, the effect of nano B on plant development is not well known yet. Therefore, in this study, photosynthesis (chlorophyll fluorescence), oxidative stress, antioxidant defense system, and accumulation of nano and

*Corresponding author: yozkan52@gmail.com

micro B particles in *Lemna minor* were compared in the same conditions. As a result, the ecotoxicity of the micro and the nanoparticles therefrom was evaluated as comparative. Nowadays, we think that our study will contribute to the literature and present a different point of view to the ecotoxicity experiments, as there are very few studies comparing the toxicity of materials at nano and micro sizes.

Chloroplasts are the main source of reactive oxygen species (ROS) in plants. The main types of ROS are superoxide ($O_2^{\bullet -}$), hydrogen peroxide (H_2O_2), and hydroxyl radicals ($OH^{\bullet}$) [19]. The transformation of superoxide into hydrogen peroxide can cause problems for plants because it causes the Calvin cycle to be blocked [20]. This prevents the formation of carbohydrates. The most significant photosynthetic pigments in plants are Chlorophyll a and b. Light energy is stored as chemical energy for the production of oxygen [21]. The quantity of sunlight absorbed by a plant is largely a function of the concentrations of chlorophyll pigment. For this reason, poor concentrations of photosynthetic pigment can limit direct photosynthesis potential and therefore main production [22]. Under environmental stress of plants, chlorophyll content and photosynthetic structure behavior may change and thus affect whole plant metabolism [23]. The most widespread indicator of oxidative stress occurring in plants is lipid peroxidation causing disruption in membrane integrity [24]. In addition, cell membrane permeability and the activities of antioxidant enzymes (SOD and CAT) indicate the tolerance of plants to stress. Previous studies have documented that metal and metal oxide NPs reason oxidative stress [25,26]. For example, a significant reduction in frond numbers and a decrease in plant cellular viability of Lemna gibba applied to AgNP concentration of 0.1-10 mgL^{-1} have been detected.This effect is highly correlated with intracellular reagent production [27]. Abiotic stress conditions cause the formation of highly toxic and reactive molecules called ROS in plants. Thus, ROS causes oxidative stress by disrupting the protein, lipid, carbohydrate and DNA structure of cells. Oxidative stress caused by ROS production is deteriorated in the cell membrane due to lipid peroxidation, which is evaluated by measurement of malondialdehyde (MDA) [28]. When ROS increases, chain reactions begin, that is, catalyze the conversion of superoxide dismutase (SOD) superoxide radicals to molecular oxygen and H_2O_2. The plants have antioxidant defense systems to prevent these damages. These antioxidant systems are divided into enzymatic and non-enzymatic [29]. Factors that play a key role in the formation of NP-derived ROS are active redox cycling and particle cell interactions on nanoparticle surfaces due to the passage of pro-oxidant functional groups and metal-based NPs on the reactive surface of NPs [30,31]. Various NPs have been indicated to form ROS both *in vitro* and *in vivo*. For example, in one study, cellular ROS production was observed to be caused by various NPs such as C_{60}, single-walled carbon nanotube (SWCNT), quantum dots, and ultrafine particles [32].

In this study, *Lemna minor*, an aquatic plant, has used to assess the potential risk of nano and micro B particle suspension. *L. minor* is a suitable indicator water organism for toxicological investigations. It is proven that the water plant is highly sensitive to the toxic effects of pollutants and prevents photosynthesis and plant growth by pollutants [27,33-36]. The comparative toxic effect of nano and micro B particle suspension has been investigated in relation to the modify in the physiological state of *L. minor* and the bioaccumulation in intracellular B particles. The physiological case of *L. minor* which was exposed to nano and micro B particle under stress conditions was determined by the concentration of chlorophyll a (chl-a), chlorophyll b (chl-b) and a+b (photosynthetic pigments), hydrogen peroxide (H_2O_2), and malondialdehyde (MDA) with antioxidant enzyme activity such as superoxide dismutase and catalase. The effects of bulk material (micro boron) and nano boron materials on the plant have been investigated. The data obtained were evaluated by comparing these two forms (nano and micro). In this respect, it contains differences from many studies that are currently available in the literature. In addition, it is different from the studies in the literature as the studies conducted are evaluated not from a single aspect but from several different aspects. These different aspects are accumulation, cell damage, and chlorophyll concentration, and antioxidant enzyme activities. All these analyzes have been evaluated and interpreted together.

2. Materials and Methods

2.1. Materials

2.1.1. Plant materials

Lemna minor used in the bioassay experiment was gathered in Muğla from Turkey. The *L. minor* was kept at 23°C and 14/10 (light/dark) photoperiod for experimental studies.

2.1.2. Boron materials

Commercially available micro boron was provided as a powder of 95% purity, average size> 100 nm, and nano boron 95% purity average size <90 nm. Boron particles, boron particles were obtained from Pavezyum Chemicals, Turkey.

2.2. The Preparation of the Test Solution

An aqueous suspension of nano and micro B particles at concentrations of 0, 50, 100, and 200 mgL^{-1} was prepared with deionized water in the dispersion medium. Afterwards, this solution was vortexed for 20 seconds. While preparing aqueous suspension of the

NPs, ultrasonic water bath (Bandelin, sonorex, Berlin, Germany) was used for 30 minutes in order to boost the dispersion in water.

2.3. Treatment Procedures of Boron Particles into the Duckweed

Lemna minor grown in laboratory conditions were exposed to B particles at 23°C and 14/10 (light/dark) photoperiod in 500 ml polyethylene bottles. Since most NPs tend to aggregate in an inert media, experiments must be carried out in the mobile system to ensure the natural conditions of the plants. For these reasons, it is necessary to provide a continuous moving environment during the experiment. In this study, an aquarium air motor was used to provide the mixture in the exposure test. Plant samples were exposed to B particles for 96 hours in the modified Hoagland nutrient solution, a mineral nutrient medium [27].

2.4. Measurement of Antioxidant Activity in the Duckweed Treated with Boron Particles

Superoxide dismutase (SOD) activity was measured as defined by Beauchamp and Fridovich [37]. Briefly, one unit is described as the quantity of enzyme that causes a 50% reduction by nitro blue tetrazolium (NBT). SOD was determined by inhibition of NBT at 560 nm. Catalase (CAT) activity was defined using the method of Jebara by monitoring the early rate of the decrease in absorbance at 240 nm by the of H_2O_2 reduction over one minute [38].

2.5. Assessment of Lipid Peroxidation in the Duckweed Treated with Boron Particles

Thiobarbituric acid (TBA) was used to determine malondialdehyde (MDA), the final product of lipid peroxidation. 200 mg of the plant was homogenized in 10 ml of 0.1% trichloroacetic acid (TCA) solution. The homogenate obtained was centrifuged at 15 000 g for 15 min. The reaction mixture containing 1 ml of supernatant and 4 ml of TBA was heated in a hot water bath at 90°C for 20 minutes and right off cooled in ice bath. The absorbance of the MDA-TBA mixture centrifuged at 15 000 g for 15 minutes was then determined at a wavelength of 532 nm. This amount of the MDA-TBA mixture was calculated from the absorbance coefficient [37,39,40].

$$MDA(nmol/ml) = [(A_{532} - A_{600})/155000] \times 10^6 \quad (1)$$

2.6. Determination of H_2O_2 in the Duckweed Treated with Boron Particles

The level of H_2O_2 was identified according to the process expressed by Mukherjee and Choudhuri with minor changes [39]. Firstly, the titanium solution was prepared. For this, 1 gram of TiO_2 and 10 g of K_2SO_4 were boiled in 150 ml of concentrated H_2SO_4 on the hot plate for 2 hours and cooled. Then 1.5 liters completed. 0.5 gram of the plant was mix well with 10 ml of cold acetone and the mix filtered through glass fiber filters (Whatman GF/F, 47 mm). 4 ml of TiO_2 solution and 5 ml of concentrated NH_3 solution were joined to the extract. Then this solution centrifuged at 10 000 g for 10 min. and the supernatant poured out and the precipitate dissolved with 10 mL of 1 M H_2SO_4. Again, this process was repeated at 10 000 g for 5 minutes, the insoluble fraction was discarded and H_2O_2 at 415 nm was detected [39,40].

2.7. Chlorophyll Analysis in the Duckweed Treated with Boron Particles

10 ml 80% (v/v) acetone solution and 300 g quartz sand were added to the plant and crushed. The extract obtained was taken into a centrifuge tube and 4 ml of 80% acetone was added. After centrifugation, the extract was filtered owing to Whatman black-band filter paper and the final volume was brought to 10 ml. The Liquid was read in the spectrophotometer at 663 to 645 nm. The amount of chlorophyll pigment was calculated using Equations 2 and 3 where D is wavelength, V is 100% end volume of acetone and A is weight of leaf tissue in grams [41].

$$\mathrm{Chl-a}(mg)/Tissue(g) = [12.7(D_{663}) - 2.69(D_{645})] \times (V/100 \times A) \quad (2)$$

$$\mathrm{Chl-a}(mg)/Tissue(g) = [22.9(D_{645}) - 4.68(D_{663})] \times (V/100 \times A) \quad (3)$$

2.8. Determination and Digestion of Boron Particles

The plant samples were placed on drying papers and dried for 24 hours at 80°C in a drying oven. Dried samples were first filtered by burning in a mixture of concentrated 10 ml HNO_3 (nitric acid). All examples were examined using Perkin Elmer Elan DRC-e inductively coupled plasma-mass spectrometry (ICP-MS, Shelton, USA) for boron analysis.

2.9. Statical Analysis

SPSS 22.0 program was used to determine significant differences. Multifactor analysis of variance (ANOVA) was used to define statistical differences in the various criteria between obtained plant data. Tukey's mean separation tests were applied if F-values from the ANOVA were significant at the *P<0.05*, *P<0.01*, and *P<0.001* levels.

3. Results and Discussion

3.1. Results

3.1.1. Chlorophyll concentration in L. minor

In Figure 1, it is observed that, when the concentration of nano B increased, the Chl-a and Chl-b decreased, whereas, in the micro B treatment, opposite findings were registered. Compared with the control group, the

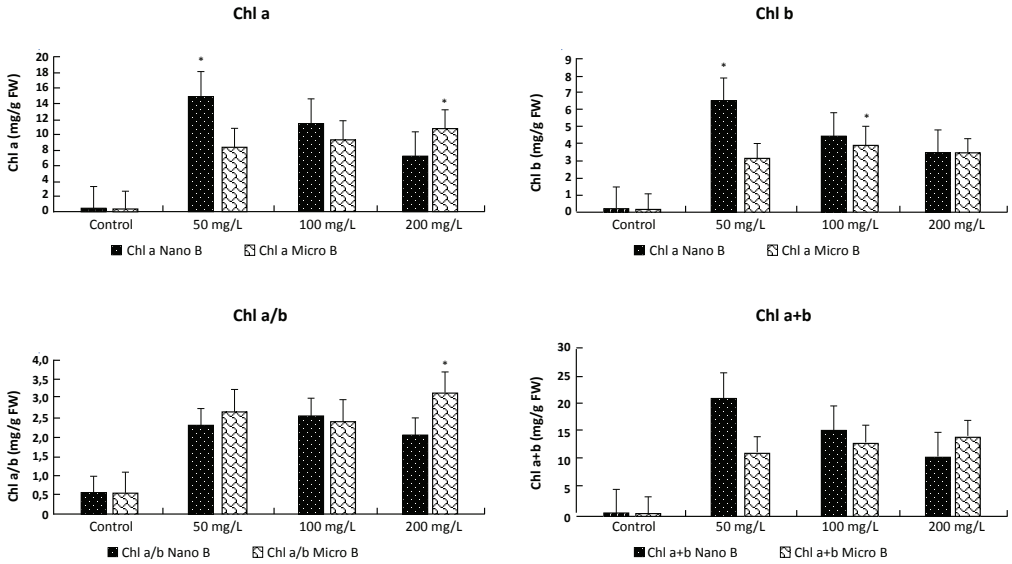

Figure 1. The assessment of pigment contents versus time in *L. minor* exposed to nano and micro B particles. Values indicate mean± standard deviation. Those with different stars on error bar are significantly different (*P<0.001*, Tukey multiple comparison).

concentration of both Chl-a and Chl-b are higher in the groups exposed to B particles. The maximum concentration of Chl-a/b was calculated at 100 mgL^{-1} in nano B and 200 mgL^{-1} in micro B. The values Chl-a+b of treatment groups were calculated to be higher than that of the control group, and it was calculated the highest as 50 mgL^{-1} for nano B and 200 mgL^{-1} for micro B.

3.1.2. Oxidative stress and tissue damage caused by boron particles

The exposure of duckweed to 50, 100, and 200 mgL^{-1} nano and micro B particles under 23°C and 14/10 (light/dark) photoperiod conditions resulted in significant differences in SOD and CAT activities, MDA and H_2O_2 levels, and both groups (nano and micro B treatment group) indicated significant differences in B particle concentrations. The maximum SOD activity in the nano B particle was recorded at 100 mgL^{-1}. At 50 and 200 mgL^{-1}, SOD activity was lower than the control group, especially at 50 mgL^{-1}, and it was measured almost half of the control group. SOD activity for nano B was low in all treatment groups compared to the control and exposed groups of micro B particles. The least SOD activity was measured in the lowest concentration group, 50 mgL^{-1} (*P<0.001*). CAT activity in nano B is much higher in treatment groups of micro B and than the control group.The highest CAT activity in exposed groups was reported 200 mgL^{-1} and the lowest CAT activity at 100 mgL^{-1}. The CAT activity of micro B was higher in all treatment groups except the 200 mgL^{-1} concentration compared to the control group.

Identification of the amount of MDA, a product that results from the oxidation of lipids as a result of destruction in cell membranes, can give information about the reaction of *L. minor* to nano and micro B particles. According to this, MDA values reached its highest value at 100 mgL^{-1} concentration in both B particles. The MDA level of micro B is higher than nano B. Whereas, 200 mgL^{-1} of micro B with 50 mgL^{-1} nano B were found to have a lower MDA value than the control group. The H_2O_2 level of the nano B was significantly lower 50 mgL^{-1} compared to the control group. The highest production was 100 mgL^{-1} and 200 mgL^{-1} was slightly higher in the control group. At all concentrations in micro B, the H_2O_2 level was higher than the control group and values were close to each other (Figure 2).

3.1.3. Correlation between test results

Correlations were executed among the MDA, SOD, H_2O_2, and CAT results of the *L. minor* leaf concentration of nano and micro B applied at different concentrations. According to the Pearson correlation results, the correlation between only the nano B concentration of different doses of nano and micro B particles in leaf tissue of the *L. minor* was determined. Accordingly, MDA indicated a positive correlation with both SOD and H_2O_2. However, a positive correlation was also found between SOD and H_2O_2 (Table 1).

3.1.4. Accumulation of B particles in L. minor

In Figure 1, as a effect of exposure to B nano and micro particles for 96 h, the accumulation in leaf tissues of the *L. minor* reduced by the increase in the concentration of nano B. On the contrary, micro B, as the concentration of micro B increases the accumulation of plant tissue. Significant differences were found at the levels of *P<0.001* in terms of accumulation between different concentrations of the nano and micro B particles in *L. minor*. According to Tukey's test results, these differences are due to the maximum accumulation in plant tissue at 50 mgL^{-1} for nano B and 200 mgL^{-1} for micro B (Figure3).

3.2. Discussion

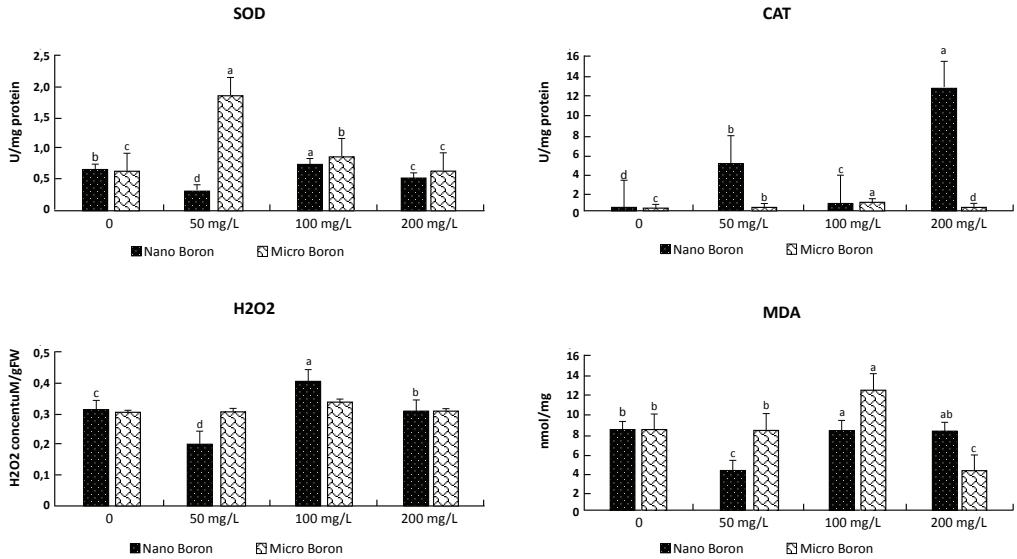

Figure 2. Activitiy of (a) SOD and (b) CAT, and levels of (c) H_2O_2, and (d) MDA in *L. minor* leaf tissue following its exposure to nano and micro B particles for 96 h. They were exposed under control group and B particle conditions; values indicate the mean and the error bars indicate standard deviation.

Macrophytes are used in laboratory tests to determine the toxicity of potential contaminants. Macrophytes such as *L. minor* are preferred species in toxicity tests. Because they are often used as a representative species for all other vascular plants [42]. Rapid and precise techniques are needed to assess the effects of NPs on *L. minor*. One of these techniques is Chl-a, which is a fast technique for measuring the photosynthetic electron transport in these plants. Due to its role in the Chl-a light collection complex and its presence

Table 1. Pearson correlation results of different doses of nano and micro B particles.

		Nano B 50 mgL^{-1}			Micro B 50 mgL^{-1}				
		MDA	SOD	H_2O_2	CAT	MDA	SOD	H_2O_2	CAT
MDA		1							
SOD	Nano B 50 mgL^{-1}	0.839	1						
H_2O_2		0.982*	0.0925	1					
CAT		-0.009	0.501	0.195	1				
MDA		0.137	0.283	0.232	0.678	1			
SOD	Micro B 50 mgL^{-1}	-0.823	-0.796	-0.821	0.043	0.330	1		
H_2O_2		0.492	0.250	0.462	0.077	0.745	0.090	1	
CAT		0.491	0.554	0.566	0.591	0.930	0.011	0.843	1
		Nano B 100 mgL^{-1}			Micro B 100 mgL^{-1}				
		MDA	SOD	H_2O_2	CAT	MDA	SOD	H_2O_2	CAT
MDA		1							
SOD	Nano B 100 mgL^{-1}	0.861	1						
H_2O_2		0.966*	0.901	1					
CAT		-0.019	0.522	0.174	1				
MDA		0.169	0.432	0.417	0.643	1			
SOD	Micro B 100 mgL^{-1}	-0.931	0.789	0.817	0.043	0.150	1		
H_2O_2		-0.426	0.776	0.430	0.769	0.192	0.526	1	
CAT		0.309	0.530	0.543	0.600	0.989*	0.015	0.220	1
		Nano B 200 mgL^{-1}			Micro B 200 mgL^{-1}				
		MDA	SOD	H_2O_2	CAT	MDA	SOD	H_2O_2	CAT
MDA		1							
SOD	Nano B 200 mgL^{-1}	0.791	1						
H_2O_2		0 .966*	0.894	1					
CAT		0.054	0.526	0.199	1				
MDA		0.113	0.371	0.337	0.744	1			
SOD	Micro B 200 mgL^{-1}	-0.857	0.787	0.794	0.058	0.247	1		
H_2O_2		-0.098	0.605	0.204	0.613	0.030	0.478	1	
CAT		0.390	0.507	0.573	0.597	0.952*	0.025	0.109	1

* Correlation is significant at the 0.05 level (2-tailed).
** Correlation is significant at the 0.01 level.

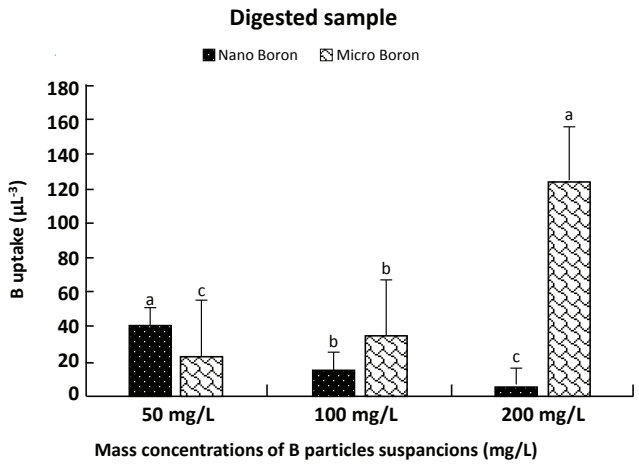

Figure 3. Comparison of ICP-MS analysis of internalized nano and micro boron particles in *Lemna minor* after exposure to 50-200 mgL^{-1} boron particles during 96 hours.

in the PSII reaction center as the electron supplier of the photovoltaic electron transport chain, it causes more photodegradation than other photosynthetic pigments [43]. In our study, Chl-a concentration was much higher in nano and micro boron treated groups compared to the control group. When nano and micro B are compared with each other, in nano B, Chl-a decreased as the concentration increases and in micro B also occurred in the opposite, and at higher concentrations Chl-a is increased. This situation has been proven in many studies by enhancing the electron transfer efficiency of the photosynthetic reaction centers of NPs [44,45]. As an example of this, Juhel et al. [46] noted that aluminum oxide (Al_2O_3) NPs enhance *L. minor* growth. However, the possible cause of the decline of the Chl-a with increasing nano B particle concentration is the surface area of the nanoparticle dose is likely to correlate well with the toxicity of the nanoparticle dose, and this is an alternative to the classical mass dose [47-49]. In addition, although the nanotoxicity mechanism is not fully known, it has been noted that the chemical composition and structure of the nanoparticles, particle size and surface area volume ratio are closely related to the toxicity. Toxicity of nanoparticles may occur as a result of chemical toxicity based on the chemical composition, such as the release of (toxic) ions, or as stresses or stimuli that are generated by factors such as the surface, size, shape of the particles. In addition, the nanoparticle surface area is an important factor that directs particle reactivity and the formation of oxidants and free radical activity [50]. In this study, the likely cause of the change in Chl-a concentration in nano B treated groups is the toxicity associated with the increasing surface area of the nano B, depending on the concentration. Because, as the nano B concentration increases, the Chl-a decreased (In groups treated with 200 mgL^{-1} nano B according to 50 mgL^{-1}, Chl-a concentration decreased by 50%). Thus, the Chl-a measurement can function as a delicate parameter in assessing growth inhibition and can be used as a stimulus to nanoparticle exposure. However, when evaluated generally, the Chl-a concentration is higher in the B treated groups than in the control group. Probably the reason for this is that boron is an indispensable nutrient for plants. Furthermore, there is a very delicate balance between boron deficiency and toxicity in plants. Plants need an very small amount of boron, which is involved in protein synthesis. The excess of B has a negative effect on the growth as in B deficiency. The excess of B (even if very little) has a negative effect on the development as in boron deficiency [51]. In our study, toxicity was not observed in the conventional B (micro B) concentrations and the high B concentration increased the Chl-a concentration (for example, micro B increased 29% at 200 mgL^{-1} compared to 50 mgL^{-1} in the treated groups. Dawis et al.) reported that leaf production in duckweed (*Spirodella polyrrhiza*) exposed to B decreased considerably in 3.55 mg B/l of B [52]. However, reductions in growth rate and percentages of abnormal leaves (chlorosis, necrosis and death percentages) were not apparent up to 18.9 and 22.4 mg B/l. The Chl-b concentration of nano B treated groups decreased at high concentration as in Chl-a. Chl b, the decrease was 16% and 49% in response to the100 and 200 mgL^{-1} nano B treatment, respectively, compared to 50 g/L nano B. However in micro B treated groups, the Chl-b concentration remained almost the same. In the case general state of chlorophyll , the increase was much higher in response to the nano and micro B treatment, respectively, compared to the control. 7y is not y in chl-a reaction centers, only in reaction centers of photosystems. However, Chl-b is found in both. The chl-a/b ratio is an indicator of the amount of light captured by the leaf (Figure 1) [21]. In some studies it has been determined hat the chlorophyll a ratio of Chl-a increases [53,54]. It is stated that Chl-b decays before Chl-a or Chl-b turns into Chl-a [53]. There are differences in enzymatic activities in plant tissues under different stress conditions. Adaptation of the plant to these conditions depends on qualitative and quantitative metabolic changes [55]. The existence of free radicals in living things was discovered almost 50 years ago [56]. Following this discovery, in 1956 Denham Herman hypothesized that oxygen radicals could come into being as products of *in vivo* enzymatic reactions [57]. The preservation of the structural unity of and tissues cells and the preserve of the current balance among the antioxidant system and oxidant the in fulfilling their normal function is of great importance. The degradation of this balance causes the oxidative stresses in the organism. Free radicals which formed and the reactive oxygen molecules which oxidative damage the fundamental structural molecules of the organisms, proteins, DNA and lipids [58,59]. Plant cells have a protective repair system that minimizes the level of oxidative damage. Antioxidants react with active oxygen derivatives, thus drawing the level of these harmful radicals below the level of damage. These damag-

es can be analyzed in the cell by the change of certain antioxidant enzymes such as SOD, CAT, POX. SOD which converts superoxide to H_2O_2. These are an indispensable component of antioxidant defense system in plants [60]. In this way, the superoxide molecule is reduced to a lower concentration. H_2O_2 is not radical because it does not include unmated electrons in its structure, but it can easily diffuse into or through cells passing through biological membranes and become a long-lived oxidant [61,62]. In biological systems, the actual production of H_2O_2 is transformed to H_2O_2 by the reaction of superoxide nonenzymatic or SOD catalysed dismutation. In addition, H_2O_2 is produced *in vivo* as a result of the action of certain oxidase enzymes such as amino acid oxidase, xanthine oxidase [63]. CAT is one of the major enzymes that scavenge reactive oxygen species in plant cells. CAT attend in the basic defense system against the backlog and toxicity of H_2O_2 and can function in the control of the amount of H_2O_2 in the cells. The CAT is destructive of H_2O_2. CAT activity, however, decreases at cold temperatures and stress conditions such as herbicide applications [64]. Peroxidation occurs in membrane lipids when the free radical level passed the antioxidant capacity of the cell [65-69]. Lipid peroxidation is terminated by the conversion of lipid hydroperoxides to aldehydes and other carbonyl compounds. Measuring the amount of malondialdehyde is a frequently used stress indicator for the detection of lipid peroxide levels [70]. Previous studies have shown that heavy metals lead to peroxidation of cell wall lipids by removing hydrogen from unsaturated fatty acids function ROS [71]. The level of MDA, an indicator of lipid peroxidation, is also an indicator of cell damage. [72]. Nanoparticles have been reported to cause oxidative stresses in various studies, such as in heavy metals. For example, Fe_3O_4 NP expose induced antioxidant enzyme and oxidative stress activities in ryegrass and pumpkin plants. Also, in both plants, oxidative stress is quite high on the roots compared to the shoots [73]. Oxidative stress in sand-grown wheat exposed with copper(II) oxide (CuO) and zinc oxide (ZnO) nanoparticles has been demonstrated by rised lipid peroxidation and decreased chlorophyll concentration in shoots [74]. Our study, a important rise in the lipid peroxidation of some treatment groups was observed when the nano and micro B particle applications were compared to the control group. At the SOD and CAT amounts, which were measured as antioxidant status indications, there was a significant increase in treatment groups (100 and 200 mgL^{-1} for nano B and 50 and 100 mgL^{-1} for micro B) when compared to the control group. It is known that ROS can quickly assault lipids and cause irreversible membrane damage. H_2O_2 in the cell acts as a signaling molecule and can also cause membrane damage due to its high permeability along the membranes. The fact that H_2O_2 is a pointing or harmful molecule depends on the sensitive balance between production and excretion in the cell [75]. In this study, H_2O_2 production increased in all treatment groups of micro B and other treatment groups except the lowest treatment group of nano B And MDA induced. Given both SOD and CAT activity, both antioxidant enzymes have eliminated the H_2O_2 surplus by avoiding potential lipid damage at a minimum level is caused by B particles. For example, the highest H_2O_2 produced a treatment group of 100 mgL^{-1} of nano B (2.7 times greater than the control group) and the activity of SOD and CAT increased in the cell to removed this H_2O_2. In particular, although CAT activity increased 3.7-fold over the control group, MDA production can not prevented. The level of H_2O_2 is very low in the treatment groups 50 mgL^{-1} for nano B and the 200 mgL^{-1} for micro B and could not initiate lipid peroxidation. In this study, MDA, H_2O_2 levels and SOD and CAT activities were evaluated together; In general, micro B is more toxic than nano B. However, the more the B toxicity in the *L. minor*, the more successfully the antioxidant defense system has been used to avoid these toxic effects. It can also be assumed here that H_2O_2 functions as a signaling molecule because there is a balance between cell production and excretion. Briefly, the level of free radicals in *L. minor* exposed to B particles have exceeded the antioxidant capacity of the cell and peroxidation occurred in membrane lipids. When we look at the previous studies on the *L. minor*, it is seen that the results are similar to our results. Some of these studies are; After *L. minor* treated to CuO NPs and bulk CuO (10-500 mgL^{-1}) the effects on the preventive enzymes (SOD, CAT, and POD) and the MDA level were examined. Accordingly, the SOD activity of the plant increased CuO NP, bulk CuO, with the increase of 2x Cu^{2+} released from CuO NP in the culture medium and the bulk CuO concentration increased remarkably until it reached 100 mgL^{-1}. *L. minor* teated to CuO NPs has accumulated a superoxide radical at low concentration and the Cu^{2+} release to the culture medium served as a crucial factor in increasing SOD activity. Again CAT activity and MDA content have increased CuO NP, bulk CuO and with the increase in 2x Cu^{2+} released from the CuO NP [76]. In studying the effect of TiO_2 NPs and bulk TiO_2 on *L. minor* preventive enzymes; SOD activity was increased by the increase of TiO_2 NP when the concentration of TiO_2 NP was below 100 mgL^{-1} and when the concentration of TiO_2 NP was higher than 100 mgL^{-1}, the SOD activity of *L. minor* reduced. It was noted that the SOD activity of *L. minor* in bulk TiO_2 environment did not indicate a significant increase compared to the control group until the bulk TiO_2 concentration reached 2000 mgL^{-1}. The level of MDA increased with the increase of TiO_2 NP in culture medium. The MDA amonut of the *L. minor* cultured in the Bulk TiO_2 medium did not differ significantly compared to the control group. In another study, the toxic effect of Ag NPs were assessed by intracellular ROS production in *L. gibba* due to the induction of oxidative stress. When the plant was exposed to 10 mgL^{-1} Ag NPs, high fluorescence emission of the ROS sensor

was observed when in proportion tothe control group. It is therefore noted that the formation of ROS is increased due to Ag NPs toxicity [27]. Again CuO NPs, CS-CuO NPs and copper sulphate have been reported to reduce in the *L. gibba* deceleration, inhibit photosynthetic activity, reduce esterase activity and induce ROS formation [77].

Malondialdehyde (MDA) is the final product ensue from the peroxidation of cellular membranes [76,78]. The increase in H_2O_2 concentration in cells under stress conditions is considered to be a general reaction to the stress. Researchers have noted that H_2O_2 induces plant defense induced defense systems, low amounts of MDA and high H_2O_2 in tolerant species [79,80]. Similar results were found in our study as in other studies. Our study, in the correlation analysis performed, the only, in the all groups of nano B was found to be negatively correlated between MDA and H_2O_2 and positive correlation between MDA and CAT at 100 mgL^{-1} of micro B. Normally it is expected that the MDA and H_2O_2 levels expected to show a positive correlation, but the likely reason for this is that the cell has other toxicities other than free radicals. Because of *L. minor* shows toxicity to 100 mgL^{-1} of micro B, increased H_2O_2 caused the increase of CAT and MDA, which is an indicator of cell membrane damage. There are several possible reasons why no correlation results will occur in other doses of micro B. This may be due to the lack of toxic effects or blocking synthesis over the dosage required for the protein synthesis mechanism due to its extreme toxicity. This has been shown in previous studies, and in soybeans, in the case of B excess, the amount of total protein decreased in the B treated groups compared to the control group [81]. Similar findings have been found in the literature regarding the content of B and plant protein [82]. It has been noted that in the B excess of Indian peas (*Cajaunus cajan*) it reduces protein content by destroying some proteins. This suggests that boron plays a role in nitrogen metabolism. In another study, the activity of nitrate reductase was reduced in B deficiency or excess, and it has been noted that the conversion of nitrate (NO_3^-) to nitrogen dioxide (NO_2) and its binding to organic compounds via ammonium (NH_4^+) is reduced.

4. Conclusions

Although *L. minor* can take up micro B particles more than the nano B, under experimental conditions, some nano B treated groups have more MDA and H_2O_2 levels (e.g., 200 mgL^{-1}). That is, although micro B are more abundant in the plant, nano B is more likely to induced oxidative stress. In addition, significantly stimulated oxidative stress indicates that exposure to high doses of B may create a risk of toxicity for nano and micro B particles. As a result of our findings, further efforts should be made to assess the risk of nanotechnology applications so that the adverse ecophysiological effects of the aquatic ecosystem and the organism's nanoparticle exposure can be reduced and controlled. Furthermore, more careful conservation of nanotechnology wastes should be made and more sensitive to release surrounding environment.

Acknowledgment

This research article was supported by the Ordu University Scientific Research Projects (BAP) with code AR-1671.

References

[1] Elimelech, M., Gregory, J., & Jia, X. (2013). *Particle deposition and aggregation: measurement, modelling and simulation*. Butterworth-Heinemann.

[2] Scientific Committee on Emerging and Newly Identified Health Risks. (2005). *Opinion on the appropriateness of existing methodologies to assess the potential risks associated with engineered and adventitious products of nanotechnologies* (SCENIHR/002/05). European Commission.

[3] Lead, J. R., & Wilkinson, K. J. (2006). Aquatic colloids and nanoparticles: current knowledge and future trends. *Environmental Chemistry, 3*(3), 159-171.

[4] Dağlıoğlu, Y., & Yılmaz Öztürk, B. (2018). Effect of concentration and exposure time of ZnO-TiO2 nanocomposite on photosynthetic pigment contents, ROS production ability, and bioaccumulation of freshwater algae (Desmodesmus multivariabilis). *Caryologia, 71*(1), 13-23.

[5] Pan, B., & Xing, B. (2010). Manufactured nanoparticles and their sorption of organic chemicals. *Advances in Agronomy, 108*, 137-181.

[6] Rico, C. M., Majumdar, S., Duarte-Gardea, M., Peralta-Videa, J. R., & Gardea-Torresdey, J. L. (2011). Interaction of nanoparticles with edible plants and their possible implications in the food chain. *Journal of Agricultural and Food Chemistry, 59*(8), 3485-3498.

[7] Monica, R. C., & Cremonini, R. (2009). Nanoparticles and higher plants. *Caryologia, 62*(2), 161-165.

[8] Yilmaz Öztürk, B., Dağlıoğlu, Y., Aşikkutlu, B., & Akköz, C. (2018). Changes in pigment content of green algae (Desmodesmus sp. and Chodatodesmus mucranulatus) exposed to alumina oxide (Al2O3) nanoparticles. *Biological Diversity and Conservation, 11*(3), 64-70.

[9] Dağlıoğlu, Y. (2018). A comparison of the acute toxicity and bioaccumulation of boron particles (nano and micro) in chodatodesmus mucronulatus. *Journal of Boron, 3*(3), 157-165.

[10] Fleischer, A., O'Neill, M. A., & Ehwald, R. (1999). The pore size of non-graminaceous plant cell walls is rapidly decreased by borate ester cross-linking of the pectic polysaccharide rhamnogalacturonan II. *Plant Physiology, 121*(3), 829-838.

[11] Navarro, E., Piccapietra, F., Wagner, B., Marconi, F., Kaegi, R., Odzak, N., Sigg L., & Behra, R. (2008). Toxicity of silver nanoparticles to Chlamydomonas re-

inhardtii. *Environmental Science&Technology, 42*(23), 8959-8964.

[12] Navarro, E., Baun, A., Behra, R., Hartmann, N. B., Filser, J., Miao, A. J., Quigg P., & Sigg, L. (2008). Environmental behavior and ecotoxicity of engineered nanoparticles to algae, plants, and fungi. *Ecotoxicology, 17*(5), 372-386.

[13] Moore, M. N. (2006). Do nanoparticles present ecotoxicological risks for the health of the aquatic environment?. *Environment International, 32*(8), 967-976.

[14] Nair, R., Varghese, S. H., Nair, B. G., Maekawa, T., Yoshida, Y., & Kumar, D. S. (2010). Nanoparticulate material delivery to plants. *Plant Science, 179*(3), 154-163.

[15] Poslu, K., & Arslan, İ. H. (1995). Dünya bor mineralleri ve bileşikleri üretiminde Türkiye'nin yeri. *Endüstriyel Hammaddeler Sempozyumu [Symposium of Industrial Raw Materials], Turkey*, 33-34.

[16] Bekish, Y. N., Poznyak, S. K., Tsybulskaya, L. S., & Gaevskaya, T. V. (2010). Electrodeposited Ni–B alloy coatings: structure, corrosion resistance and mechanical properties. *Electrochimica Acta, 55*(7), 2223-2231.

[17] Zhang, X. W., Zou, Y. J., Yan, H., Wang, B., Chen, G. H., & Wong, S. P. (2000). Electrical properties and annealing effects on the stress of RF-sputtered c-BN films. *Materials Letters, 45*(2), 111-115.

[18] Dyar, J. J., & Webb, K. L. (1961). A relationship between boron & auxin in C14 translocation in bean plants. *Plant Physiology, 36*(5), 672.

[19] Mittler, R., Vanderauwera, S., Gollery, M., & Van Breusegem, F. (2004). Reactive oxygen gene network of plants. *Trends in Plant Science, 9*(10), 490-498.

[20] Shen, M., Haggblom, C., Vogt, M., Hunter, T., & Lu, K. P. (1997). Characterization and cell cycle regulation of the related human telomeric proteins Pin2 and TRF1 suggest a role in mitosis. *Proceedings of the National Academy of Sciences, 94*(25), 13618-13623.

[21] Lin, Y. M., Zou, X. H., Liu, J. B., Guo, Z. J., & Lin, P. S. S., 2005: Nutrient, chlorophyll and caloric dynamics of Phyllostachys pubescens leaves in Yoncghun Country, Fujian. *China. Journal of Bamboo and Rattan, 4*, 369-385.

[22] Filella, I., Amaro, T., Araus, J. L., & Peñuelas, J. (1996). Relationship between photosynthetic radiation-use efficiency of barley canopies and the photochemical reflectance index (PRI). *Physiologia Plantarum, 96*(2), 211-216.

[23] Ayeni, O. O., Ndakidemi, P. A., Snyman, R. G., & Odendaal, J. P. (2012). Assessment of metal concentrations, chlorophyll content and photosynthesis in phragmites australis along the Lower Diep River, CapeTown, South Africa. *Energy and Environment Research, 2*(1), 128-139.

[24] Kumar, P., Kumar, D., Sikka, P., & Singh, P. (2015). Sericin supplementation improves semen freezability of buffalo bulls by minimizing oxidative stress during cryopreservation. *Animal Reproduction Science, 152*, 26-31.

[25] Vallyathan, V., & Shi, X. (1997). The role of oxygen free radicals in occupational and environmental lung diseases. *Environmental Health Perspectives, 105*(suppl 1), 165-177.

[26] Manke, A., Wang, L., & Rojanasakul, Y. (2013). Mechanisms of nanoparticle-induced oxidative stress and toxicity. *BioMed Research International, 2013*, 942916.

[27] Oukarroum, A., Barhoumi, L., Pirastru, L., & Dewez, D. (2013). Silver nanoparticle toxicity effect on growth and cellular viability of the aquatic plant Lemna gibba. *Environmental Toxicology and Chemistry, 32*(4), 902-907.

[28] Khataee, A., Bozorg, S., Khorram, S., Fathinia, M., Hanifehpour, Y., & Joo, S. W. (2013). Conversion of natural clinoptilolite microparticles to nanorods by glow discharge plasma: a novel Fe-impregnated nanocatalyst for the heterogeneous Fenton process. *Industrial&Engineering Chemistry Research, 52*(51), 18225-18233.

[29] Gill, S. S., & Tuteja, N. (2010). Reactive oxygen species and antioxidant machinery in abiotic stress tolerance in crop plants. *Plant Physiology and Biochemistry, 48*(12), 909-930.

[30] Knaapen, A. M., Borm, P. J., Albrecht, C., & Schins, R. P. (2004). Inhaled particles and lung cancer. Part A: Mechanisms. *International Journal of Cancer, 109*(6), 799-809.

[31] Risom, L., Møller, P., & Loft, S. (2005). Oxidative stress-induced DNA damage by particulate air pollution. *Mutation Research/Fundamental and Molecular Mechanisms of Mutagenesis, 592*(1-2), 119-137.

[32] Oberdörster, G., Oberdörster, E., Oberdörster, J. (2005). Nanotoxicolgy, an emerging discipline evolving from studies of ultrafine particles. *Health Perspective, 113*(7), 823-839, 2005.

[33] Dewez, D., Dautremepuits, C., Jeandet, P., Vernet, G., & Popovic, R. (2003). Effects of methanol on photosynthetic processes and growth of Lemna gibba. *Photochemistry and Photobiology, 78*(4), 420-424.

[34] Dağlıoğlu, Y., & Öztürk, B. Y. (2019). A novel intracellular synthesis of silver nanoparticles using Desmodesmus sp.(Scenedesmaceae): different methods of pigment change. *Rendiconti Lincei. Scienze Fisiche e Naturali, 30*(3), 611-621.

[35] Dağlıoğlu, Y., & Yılmaz Öztürk, B. (2016). The assessment of biological accumulation on exposure in boron particles of Desmodesmus multivariabilis. *Biological Diversity and Conservation, 9*(3), 204-209.

[36] Dağlıoğlu, Y., & Yılmaz Öztürk, B. (2018). Effect of concentration and exposure time of ZnO-TiO2 nanocomposite on photosynthetic pigment contents, ROS production ability, and bioaccumulation of freshwater algae (Desmodesmus multivariabilis). *Caryologia, 71*(1), 13-23.

[37] Beauchamp, C., & Fridovich, I. (1971). Superoxide dismutase: improved assays and an assay applicable to

acrylamide gels. *Analytical Biochemistry, 44*(1), 276-287.

[38] Jebara, S., Jebara, M., Limam, F., & Aouani, M. E. (2005). Changes in ascorbate peroxidase, catalase, guaiacol peroxidase and superoxide dismutase activities in common bean (Phaseolus vulgaris) nodules under salt stress. *Journal of Plant Physiology, 162*(8), 929-936.

[39] Mukherjee, S. P., & Choudhuri, M. A. (1983). Implications of water stress-induced changes in the levels of endogenous ascorbic acid and hydrogen peroxide in Vigna seedlings. *Physiologia Plantarum, 58*(2), 166-170.

[40] Sairam, R. K., & Saxena, D. C. (2000). Oxidative stress and antioxidants in wheat genotypes: possible mechanism of water stress tolerance. *Journal of Agronomy and Crop Science, 184*(1), 55-61.

[41] Heath, R. L., & Packer, L. (1968). Photoperoxidation in isolated chloroplasts: I. Kinetics and stoichiometry of fatty acid peroxidation. *Archives of Biochemistry and Biophysics, 125*(1), 189-198.

[42] Lewis, M. A. (1995). Use of freshwater plants for phytotoxicity testing: a review. *Environmental Pollution, 87*(3), 319-336.

[43] Geoffroy, L., Frankart, C., & Eullaffroy, P. (2004). Comparison of different physiological parameter responses in Lemna minor and Scenedesmus obliquus exposed to herbicide flumioxazin. *Environmental Pollution, 131*(2), 233-241.

[44] Govorov, A. O., & Carmeli, I. (2007). Hybrid structures composed of photosynthetic system and metal nanoparticles: plasmon enhancement effect. *Nano Letters, 7*(3), 620-625.

[45] Nadtochenko, V. A., Nikandrov, V. V., Gorenberg, A. A., Karlova, M. G., Lukashev, E. P., Semenov, A. Y., Bukharina N. S., Kostrov A. N., Permenova E. P., & Sarkisov, O. M. (2008). Nanophotobiocatalysts based on mesoporous titanium dioxide films conjugated with enzymes and photosynthetic reaction centers of bacteria. *High Energy Chemistry, 42*(7), 591-593.

[46] Juhel, G., Batisse, E., Hugues, Q., Daly, D., van Pelt, F. N., O'Halloran, J., & Jansen, M. A. (2011). Alumina nanoparticles enhance growth of Lemna minor. *Aquatic Toxicology, 105*(3-4), 328-336.

[47] Donaldson, K., & Tran, C. L. (2002). Inflammation caused by particles and fibers. *Inhalation Toxicology, 14*(1), 5-27.

[48] Bouwmeester, H., Poortman, J., Peters, R. J., Wijma, E., Kramer, E., Makama, S., ... & Hendriksen, P. J. (2011). Characterization of translocation of silver nanoparticles and effects on whole-genome gene expression using an in vitro intestinal epithelium coculture model. *ACS Nano, 5*(5), 4091-4103.

[49] Von Moos, N., & Slaveykova, V. I. (2014). Oxidative stress induced by inorganic nanoparticles in bacteria and aquatic microalgae–state of the art and knowledge gaps. *Nanotoxicology, 8*(6), 605-630.

[50] Brunner, T. J., Wick, P., Manser, P., Spohn, P., Grass, R. N., Limbach, L. K., ... & Stark, W. J. (2006). In vitro cytotoxicity of oxide nanoparticles: comparison to asbestos, silica, and the effect of particle solubility. *Environmental Science&Technology, 40*(14), 4374-4381.

[51] Kaçar, B. (1977). *Bitki besleme [Plant nourishment]*. Ankara University Faculty of Agriculture Publishing.

[52] Davis, S. M., Drake, K. D., & Maier, K. J. (2002). Toxicity of boron to the duckweed, Spirodella polyrrhiza. *Chemosphere, 48*(6), 615-620.

[53] Scheumann, V., Schoch, S., & Rüdiger, W. (1999). Chlorophyll b reduction during senescence of barley seedlings. *Planta, 209*(3), 364-370.

[54] Turkis, S., & Özbucak, T. B. (2010). Foliar resorption and chlorophyll content in leaves of Cistus creticus L.(Cistaceae) along an elevational gradient in Turkey. *Acta Botanica Croatica, 69*(2), 275-290.

[55] Odabaş, F. (1981). Bacchus çeşidinde (Vitis vinifera L.) yapraklarin klorofil miktari üzerine azot gübrelemesinin etkisi [Effect of nitrogen manuring on chlorophyll amount of leaves on Bacchus spp. (Vitis vinifera L.)]. *Atatürk University Journal of Agricultural Faculty, 12*(2-3), 39-50.

[56] Halliwell, B. (1994). Free radicals and antioxidants: a personal view. *Nutrition Reviews, 52*(8), 253-265.

[57] Murray, R. K., Granner, D. K., Mayes, P. A., & Rodwell, V. W. (1996). *Harper'ın Biyokimyası* (N. Dikmen, T. Özgünen, Trans.), İstanbul: Barış Kitabevi. (Original work published in 1996).

[58] Commoner, B., Townsend, J., & Pake, G. E. (1954). Free radicals in biological materials. *Nature, 174*(4432), 689-691.

[59] Harman, D. (1956). Aging: a theory based on free radical and radiation chemistry. *Journal Gerontology, 11*(3), 298-300.

[60] Paz-Elizur, T., Krupsky, M., Blumenstein, S., Elinger, D., Schechtman, E., & Livneh, Z. (2003). DNA repair activity for oxidative damage and risk of lung cancer. *Journal of the National Cancer Institute, 95*(17), 1312-1319.

[61] Halliwell, B. (1994). Free radicals and antioxidants: a personal view. *Nutrition reviews, 52*(8), 253-265.

[62] Burke, J. J. (1995). Enzyme adaptation to temperature. In N. Smirnoff (Ed.), *Environment and Plant Metabolism: Flexibility and Acclimation* (pp. 63-78). BIOS Scientific Publishers.

[63] Halliwell, B., & Gutteridge, J. M. (1990). Role of free radicals and catalytic metal ions in human disease: an overview. *Methods in Enzymology, 186*, 1-85.

[64] Caporaso, N. (2003). The Molecular Epidemiology of Oxidative Damage to DNA and Cancer. J*ournal of the National Cancer Institute, 95*(17), 1263-1265.

[65] Ames, B. N. (1983). Dietary carcinogens and anticarcinogens: oxygen radicals and degenerative diseases. *Science, 221*(4617), 1256-1264.

[66] Cross, C. E., Halliwell, B., Borish, E. T., Pryor, W. A., Ames, B. N., Saul, R. L., ... & Harman, D. (1987). Oxygen radicals and human disease. *Annals of Internal Medicine, 107*(4), 526-545.

[67] Dumitrescu, C., Belgun, M., Olinescu, R., Lianu, L., & Bartoc, C. (1993). Effect of vitamin C administration on the ratio between the pro-and antioxidative factors. *Romanian Journal of Endocrinology, 31*(1-2), 81-84.

[68] Smirnoff, N. (1995). Antioxidant systems and plant response to environment. In N. Smirnoff (Ed.), *Environment and Plant Metabolism Flexibility and Acclimation* (pp. 217-243). BIOS Scientific Publishers.

[69] Song, G., Hou, W., Gao, Y., Wang, Y., Lin, L., Zhang, Z., ... & Wang, H. (2016). Effects of CuO nanoparticles on Lemna minor. B*otanical Studies, 57*(1), 1-8.

[70] Ames, B. N., Gold, L. S., & Willett, W. C. (1995). The causes and prevention of cancer. *Proceedings of the National Academy of Sciences, 92*(12), 5258-5265.

[71] Guyton, K. Z., & Kensler, T. W. (1993). Oxidative mechanisms in carcinogenesis. *British Medical Bulletin, 49*(3), 523-544.

[72] Taulavuori, E., Hellström, E. K., Taulavuori, K., & Laine, K. (2001). Comparison of two methods used to analyse lipid peroxidation from Vaccinium myrtillus (L.) during snow removal, reacclimation and cold acclimation. *Journal of Experimental Botany, 52*(365), 2375-2380.

[73] Wang, H., Kou, X., Pei, Z., Xiao, J. Q., Shan, X., & Xing, B. (2011). Physiological effects of magnetite (Fe3O4) nanoparticles on perennial ryegrass (Lolium perenne L.) and pumpkin (Cucurbita mixta) plants. *Nanotoxicology, 5*(1), 30-42.

[74] Dimkpa, C. O., McLean, J. E., Latta, D. E., Manangón, E., Britt, D. W., Johnson, W. P., ... & Anderson, A. J. (2012). CuO and ZnO nanoparticles: phytotoxicity, metal speciation, and induction of oxidative stress in sand-grown wheat. *Journal of Nanoparticle Research, 14*(9), 1-15.

[75] Zhou, D. X., Liu, Y. F., Liu, X. B. (2009). Effects of waterlogging stress on physiological and biochemical index in Alternant phiiloxeroides Hubei, *Agricultural Sciences, 48*(3), 585-587.

[76] Sharma, P., Jha, A. B., Dubey, R. S., & Pessarakli, M. (2012). Reactive oxygen species, oxidative damage, and antioxidative defense mechanism in plants under stressful conditions. *Journal of Botany, 2012*, 217037.

[77] Perreault, F., Popovic, R., & Dewez, D. (2014). Different toxicity mechanisms between bare and polymer-coated copper oxide nanoparticles in Lemna gibba. *Environmental Pollution, 185*, 219-227.

[78] Cruz, F. J. R., Castro, G. L. S., Júnior, D. S., Festucci-Buselli, R. A., & Pinheiro, H. A. (2013). Exogenous glycine betaine modulates ascorbate peroxidase and catalase activities and prevent lipid peroxidation in mild water-stressed Carapa guianensis plants. *Photosynthetica, 51*(1), 102-108.

[79] Burzyński, M., & Kłobus, G. (2004). Changes of photosynthetic parameters in cucumber leaves under Cu, Cd, and Pb stress. *Photosynthetica, 42*(2), 505-510.

[80] Keyvan, S. (2010). The effects of drought stress on yield, relative water content, proline, soluble carbohydrates and chlorophyll of bread wheat cultivars. *The Journal of Animal and Plant Sciences, 8*(3), 1051-1060.

[81] Oluk, E. A., Latif, N. (2008). Soya fasulyesi (glycine max (l) merrill var. umut 2002) büyümesi ve gelişimi üzerine bor fazlaliğinin etkileri [Effects of excess boron on soybean (glycine max (l) merrill var. umut 2002)], *Erzincan University Journal of Science and Technology, 1*(1), 27-38.

[82] Bishnoi, S. K., Kumar, B., Rani, C., Datta, K. S., Kumari, P., Sheoran, I. S., & Angrish, R. (2006). Changes in protein profile of pigeonpea genotypes in response to NaCl and boron stress. *Biologia Plantarum, 50*(1), 135-137.

BOR DERGİSİ
JOURNAL OF BORON
https://dergipark.org.tr/boron

Bone cement formulation with reduced heating of bone cement resin

M.Özgür Seydibeyoğlu[1,2*], Müşerref Caka[3], Fulden Ulucan-Karnak[4], Günnur Onak[5], Ataç Uzel[6], Figen Ozyildiz[7], Ozan Karaman[8]

[1]Izmir Katip Celebi University, Department of Materials Science and Engineering, Izmir, 35620, Turkey
ORCID orcid.org/0000-0002-2584-7043
[2]Filinia R&D, Ege University Sciencepark, Izmir, 35040, Turkey
[3]Izmir Katip Celebi University, Department of Materials Science and Engineering, Izmir, 35620, Turkey
ORCID orcid.org/0000-0002-8688-9669
[4]Ege University, Graduate School of Natural and Applied Sciences, Biomedical Technology Department, Izmir, 35040, Turkey
ORCID orcid.org/0000-0001-5567-0261
[5]Izmir Katip Celebi University, Department of Biomedical Engineering, Izmir, 35620, Turkey
ORCID orcid.org/0000-0003-0895-4768
[6]Ege University, Department of Biology, Izmir, 35040, Turkey
ORCID orcid.org/0000-0002-1304-0509
[7]Ege University, Department of Biology, Izmir, 35040, Turkey
ORCID orcid.org/0000-0003-1006-0480
[8]Izmir Katip Celebi University, Department of Biomedical Engineering, Izmir, 35620, Turkey
ORCID orcid.org/0000-0002-4175-4402

ARTICLE INFO

Article History:
Received December 7, 2020
Accepted April 4, 2021
Available online June 30, 2021

Research Article

DOI: 10.30728/boron.835919

Keywords:
Bone cement
Boron minerals
Thermal characterization

ABSTRACT

Bone cement material is one of the key materials in bone surgery and orthopedic medicine. In this study, commercial polymethyl-methacrylate bone cement was mixed with boric acid and zinc borate to reduce the reaction temperature of the bone cement. The observation of temperature changes during the polymerization using laser thermometer and thermal camera showed that the use of boron compounds decreased the temperature of the bone cement at least 10°C which is very critical for the biomaterial uses as it affects the biocompatibility of the material. Besides temperature monitoring, microbiological tests showed that the materials have certain antibacterial effect. Water contact angle studies also supported the biocompatibility studies. In the last part, mechanical tests showed that there was not significant change in the tensile strength and tensile modulus values. Antibacterial tests exhibited thatzinc borate addition shows antimicrobial activity against *S.epidermidis* as well as boric acid addition over 5% concentration. According to the cell culture studies, boric acid can be interpreted as non-toxic up to 10%, while 10% and 20% zinc borate has toxic effect. This is the first study to use boron compounds in bone cement and it is proved that boric acid at low concentrations can be used for bone cement applications but zinc borate would not be suitable to use in medical applications due to toxic effects.

1. Introduction

Biomaterials area is attracting many different scientists from various disciplines including medical doctors, mechanical engineers, materials scientists, and polymer scientists [1]. Additive manufacturing (AM) techniques provides free-form manufacturing and clinical implementation of biomaterials. Materials scientists and engineers can combine their information's to realize of biomaterials by developing new technologies, synthesizing advanced biomaterials and improving medical-image-based digital design [2]. There have been numerous studies on biomaterials with metallic implants, ceramic materials, polymers, and composites [3-5]. Depending on the application, the load carrying capacity of the biomaterial and other medical concerns, different types of materials are preferred [6]. Among many implant surgeries, knee implant surgery has been one of the most commonly done surgeries in the world. For knee implants, a combination of metallic implant and polymeric materials are used. For metallic systems, titanium alloys and cobalt-chromium alloys are generally used. Two metal implants are joint with a polymeric material, ultrahigh molecular weight polyethylene [7]. In knee surgery, metallic implants are supported with certain polymeric materials named as bone cement and this cement layer has been used to provide better compatibility of the metallic implant with bone structure. Furthermore, it provides certain viscoelasticity for the bone replacement [8].

Orthopedic infections can be occurred during or after surgery, especially when foreign material is implanted. Bacteria, mostly staphylococci, are responsible of the-

*Corresponding author: seydibey@gmail.com

se infections by binding damaged tissue and implanted material with immediate formation of biofilms. They can be chronic and last several days or months. These infections are one of the main problems in orthopedic surgery, both for surgeons and patients. They also known with their persistency and resulted with long-term disablement of the patients. All of these problems can cause reducing the patient health quality and remarkable costs [9]. Several different strategies have been utilized to avoid orthopedic infection such as antimicrobial implant coatings and drug delivery systems. But in order to optimize and use these technologies in clinical approaches, there is still great interest and requirement of research. These researches focused on especially developing antibiotic carrier systems like drug loaded polymethyl-methacrylate (PMMA) cement beads or bio-absorbable bone substitute (BBS). With the aid of these novel methodologies, the incidence and severity of infections will reduce [10].

Polymethylmethacrylate (PMMA), is also named as bone cement, and is widely used for fixation of various implants [11]. Bone cement has been used since 1950's [12]. For bone cement, polymethyl-methacrylate has been commonly used polymer and it is a two component system with certain curing conditions and exothermic reaction. This exothermic reaction is quite dangerous for various surgery implants that cause heating and problems for the tissues during the implantation [13].

Boron minerals with a variety of compounds offer numerous solutions for polymeric materials [14-16]. Some boron minerals and compounds have been used as flame retardant and smoke suppressant for different polymers [17,18]. Moreover, anti-microbial properties of the boron compounds have been studied for several years since 1980's [19-21]. Some studies of boron minerals for medical applications show promising results for the biomedical materials in the area of anti-microbial and anti-flammatory uses [22,23]. Boric acid and zinc borate are well known for antimicrobial and heat resistant properties. Moreover, they are produced in Turkey [24].

In this study, new types of bone cement materials were prepared using commercial bone cement materials and different boron compounds. The aim of the study was to investigate the effect of boron compounds on the thermal properties of the bone cement. Bone cement is a thermosetting polymer that is cured. During curing, polymer gets heated and while applying to the human, it has a lot of potential harm for the human at high temperature. Morever, anti-microbial effects of boron minerals and chemicals have been well known and this could be additional effect for the new bone cement. Advanced characterization studies were carried out. Microbial properties were measured to understand the effect of the boron compounds. Furthermore, biocompatibility tests were conducted to understand the boron compounds with bone cement.

2. Materials and Methods

2.1. Materials

Bone cement branded AF Cement-1 was used in the study. One packet of bone cement contains 40 grams of powder and 20 ml of liquid parts. Powder part includes 35.04 grams of polymethyl methacrylate, 0.96 gram benzoyl peroxide, 4 grams of barium sulphate and liquid part includes 19.76 milliliters of methyl methacrylate, 0.24 milliliters N, N dimethylmethyl p-toluidine and 18-20 ppm hydroquinone.

Zincborate and boric acid were used as boron derivatives in the experiments. Boric acid were obtained from Eti Maden Affairs General Directorate. Zinc borate (TK.030110.01002) was obtained from Tekkim. MTT (M5655) and DMSO were obtained from Sigma.

2.2. Methods

2.2.1. Mixing bone cement and boron derivatives

Samples containing boric acid and zinc borate were produced with a mass of 1%, 5%, 10% and 20%. Boron mixtures were added to the powder part of the ready-made bone cement and then the liquid part of the bone cement was added and polymerized by mixing.

2.2.2. Characterization of developed bone cement formulations

2.2.2.1. Monitoring of the polymerization temperature

Samples containing 1%, 5%, 10% boron additive (boric acid and zinc borate) were produced. The polymerization process was monitored by measuring with a laser thermometer 30 seconds from the center of the samples. In the next experiment, samples were prepared by adding 1%, 5%, 10% and 20% of boron (zinc borate and boric acid) to the mass of the samples. Thermal images were taken every minute during the polymerization. The highest temperature at the time of curing was determined.

2.2.2.2. Fourier transform infrared spectroscopy analysis

Analysis was performed using the Perkin Elmer BX-II FTIR (UK) device. Samples were analyzed in ATR-IR mode in the spectral range of 400-4000 cm^{-1} at 2 cm^{-1} resolutions.

2.2.2.3. Dynamic mechanical analysis

The samples were examined by Perkin Elmer Instruments DMA Q800 (UK), with a 1 Hz frequency scan at

a heating rate of 3°C/min. from room temperature to 180°C. The samples had 4 cm length and 1 cm width with a 0.5 cm thickness.

2.2.2.4. Tensile test

The tensile strength and elasticity modulus were determined using a Shimadzu (Japan) brand universal tensile tester. Experiments were carried out at a draw speed of 0.1 mm/min. The samples according to the standard were prepared. At least 5 samples were tested. The test specimens were prepared according to ASTM D-638 (Tenstile testing for plastics). The load cell was 5 kN.

2.2.2.5. Contact angle

For the contact angle test, the specimens were produced with care that the surfaces are flat. Contact angle measurements were carried out at room temperature with a manual optical tensiometer Attension Theta. The liquid used was pure water and a microsyringe was used to obtain a volume of about 5 µL drop. The contact angle measurements are repeated at least five different points.

2.2.2.6. Scanning electron microscope (SEM) analysis

Scanning electron microscopy Carl Zeiss 300VP (SEM) was used to observe the polymer microstructure in 500 kV. The fracture surfaces were covered with gold and SEM images were taken.

2.2.3. Antibacterial tests

Antibacterial analysis experiments were carried out in accordance with JIS Z 2801 with slight modification. Bone cement samples with 5%, 10% and 20% zinc borate added (3) and 5%, 10% and 20% boric acid added (3) bactericidal activity tests were performed [25].

S. epidermidis [ATCC® 12228™] culture was used. The samples were prepared in the form of a thin plate 5x5 cm^2. withal materials were subjected to surface sterilization with ethanol (70% v/v). Bacteria were added to the sample surface and the tops were sealed with film and allowed to incubate for 24 hours (h) in a humidified atmosphere. Samples were than diluted serially and inoculated with Nutrient agar. After incubation at 35±1°C for 24 h bacterial counts were calculated. Additive-free cements were used as controls.

2.2.4. In vitro cytotoxicity test with MTT

The cytotoxicity test of bone cements were performed according to ISO 10993-5 standards at Katip Celebi University Biomedical Engineering Cell Culture Laboratories. The samples were incubated in serum-free Dulbecco's Modified Eagle Medium (DMEM) cell culture medium for 24 h at 5% CO_2 37°C. After 24 h, the extracts were taken from the media for cell proliferation analysis. L929 cells were seeded on 24 well plates and incubated in DMEM medium supplemented by 10% Fetal Bovine Serum (FBS), 1% Penicillin Streptomycin for 24 h. The extract of the material was added to the cells. MTT (3-(4,5-dimethyl-2-thiazolyl)-2,5-diphenyl-2Htetrazolium bromide) assay was applied for evaluating the cell proliferation of bone cements for day1, day4, and day7. At each time point, proliferation assay was performed. Briefly, the MTT solution was added to each well and incubated for 2 h at 5% CO_2 37°C. After 2 h, the MTT solution was removed from the cells and 500 µL Dimethyl Sulfoxide (DMSO) was put on the cells. The cell numbers were obtained by absorbance reading at 570 nm by using a plate reader [26,27]. The cell number for all samples were compared to negative control which contains no FBS to calculate the percentage of viable cells.

3. Results and Discussion

3.1. Thermal Measurements

During thermal measurements, reproducible measurements were obtained. In Figure 1, maximum temperature values are given. The maximum temperature value seen in unadulterated sample is 84°C. It was observed that with increased content of boric acid and zinc borate additives, the curing temperature of the bone cement decreased. With the addition of 20% boric acid and zinc borate, the temperature during this curing time has been reduced to 59.7°C and 56.5, respectively. The thermal stability and flame retardancy of the zinc borate has been quite well known and this finding has also supports this important impact of the boron minerals in the bone cement. This finding is very critical for the biomedical materials. The bone cement is a two-component curing material but the high temperature for this material can cause severe problems for the body to accept the material. It can create various problems as infections and other diseases. This

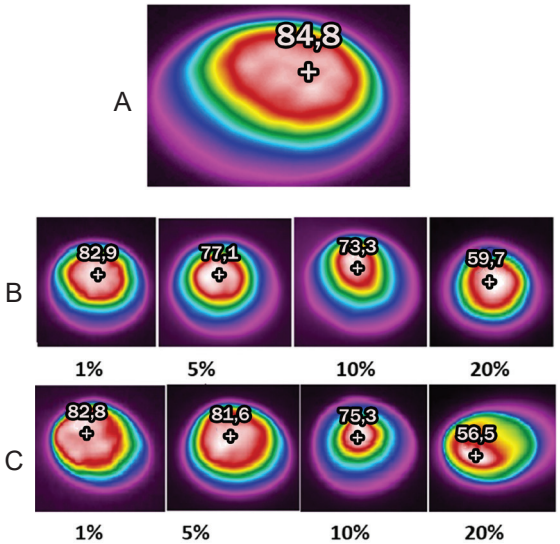

Figure 1. Maximum temperature values of A) unadulterated sample, B) BA addition, C) ZB addition.

finding will open many new possibilities for the medical device design. The thermal stability of the polymers was carried with other polymer characterization tools as well.

3.2. FTIR Results

According to FTIR spectrums in Figure 2A and Figure 2B, the band at 1720 cm^{-1} indicates the presence of the acrylate carboxyl group. All spectrum shows that addition of BA and ZB resulted with decreasing in the transmittance of the band comparison with unadulterated PMMA. The bands at 1434 cm^{-1} can be interpreted to the bending vibration of the C-H bonds of the -CH_3 group and they changed with the alteration of additives percentages. The band at 987 cm^{-1} is the characteristic absorption vibration of PMMA's BO_4 groups, together with the bands at 1062 cm^{-1} and 843 cm^{-1} [28]. The band of 1407 cm^{-1} was related to stretching vibrations of trihedral borate (BO_3) groups. The peak observed between 754 and 650 cm^{-1} wavelengths can be interpreted as in-plane bending vibrations of BO_3 groups [29]. The bands at 2956 cm^{-1} can be interpreted in the C-H bond stress vibrations of the -CH_3 and -CH_2- groups. Moreover, absorption bands at 3490 cm^{-1} can be interpreted to the stretching and bending vibrations of the -OH group. It can be said that these bands at 3490 cm^{-1} increase with boron contribution. Also, FTIR peaks show that full curing was achieved at mild temperatures as well.

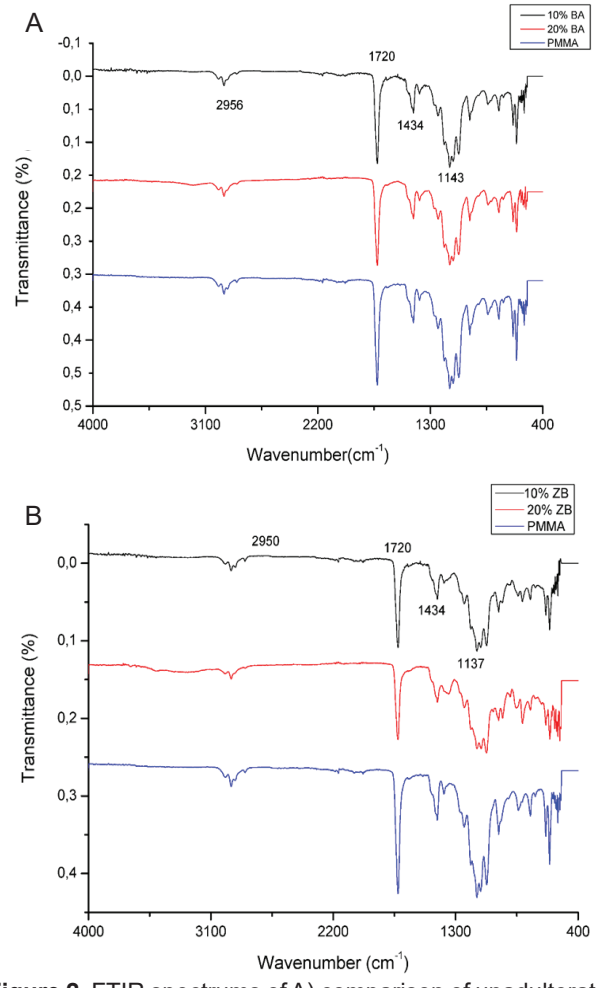

Figure 2. FTIR spectrums of A) comparison of unadulterated PMMA and BA addivites of cement and B) comparison of unadultered PMMA and ZB additive of cement.

3.3. DMA Results

It is seen that in Figure 3 of storage modulus graph, while it was around 900 MPa in the unadulterated sample, it increased to around 1300 MPa with 20% ZB and 20% BA contribution. Storage modulus values at elevated temperatures show another important aspect of thermal processes for these materials. The increase of the storage modulus values was also clearly seen at elevated temperatures which is a very important information we can get with dynamic mechanical analysis [30]. This has been done first time for the bone cement analysis in the literature.

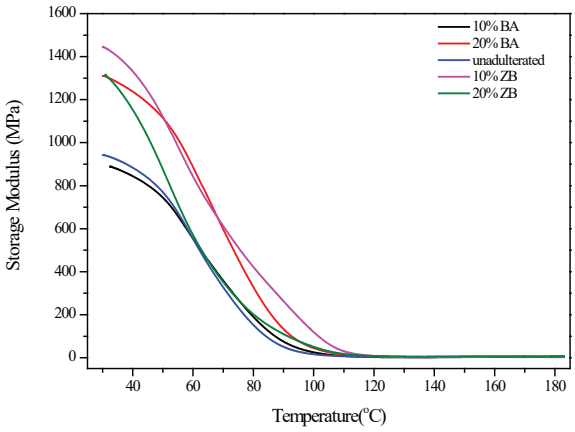

Figure 3. DMA Results of 10% BA, 20% BA, 10% ZB, 20% ZB and unadulterated samples (Storage modulus vs Temperature).

Tan-Delta data can give information about the glass transition temperature. It is seen in Figure 4, glass transition temperature is increased from 100 to 110 with 20% BA contribution and to 120 with 20% ZB contribution. The shift of glass transition temperature

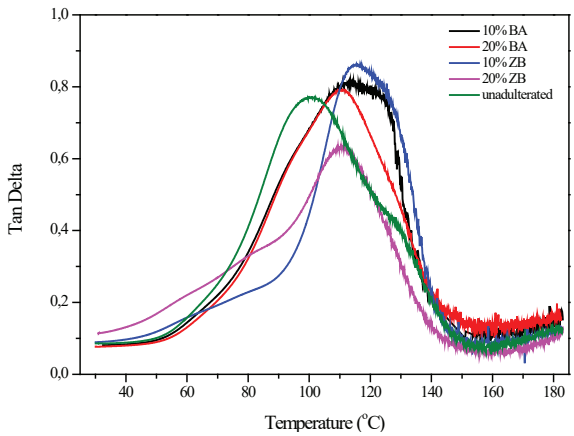

Figure 4. DMA results of 10% BA, 20% BA, 10% ZB, 20% ZB and unadulterated samples (Tan Delta vs Temperature).

shows the bonding and the rigidity of the samples. The addition of boron compounds significantly increased the glass transition temperature which shows that the materials can be stable at higher temperatures. This is also supporting the findings of thermal measurements.

While the curing temperature of the bone cement decreases, the thermal stability of the materials increases as well. This is a very important finding that can shed a light for various biomedical materials research.

3.4. Tensile Test Results

The tensile test was made by preparing a sample in molds in accordance with the "ASTM F451-08 Standard Specification for Acrylic Bone Cement" standard and the results in Figure 5 were obtained. When the shape is interpreted considering the standard deviations, it can be interpreted that the maximum tensile values are approximately the same except for the 20% boric acid addition, and that the boron additive does not change the mechanical properties of the bone cement. Especially, when the standard deviations are taken into consideration, they were almost equal. This kind of result was also presented in one of our studies showing that boron compounds do not alter the mechanical properties of the polymers. This is an important outcome of this study. As we decrease the temperature of the bone cement, the mechanical properties are not altered much.

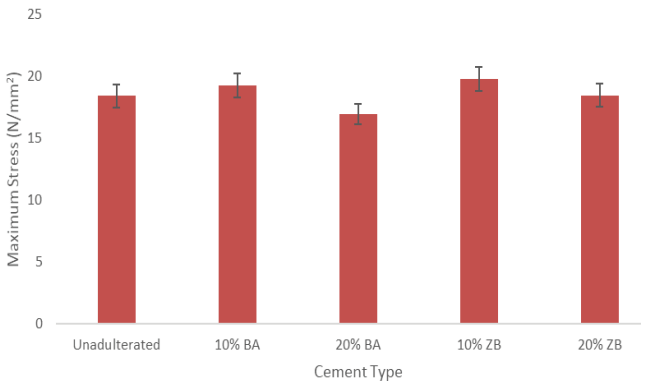

Figure 5. Maximum stress due to cement types.

3.5. Contact Angle Results

In literature, the contact angle value of PMMA has been found as 68-70 degrees, and there are studies suggesting that this value can be made super hydrophobic and increased to 154 degrees [31].

According to measurements, it is seen in Table 1, the average contact angle of the unadulterated bone cement was calculated to be 92.71 degrees, and with the addition of boric acid and zinc borate, this value was slightly decreased to an average of 87°C. It can be said that the (-OH) groups in the boron additive cause hydrophilic properties. Bone cement, which is permanent in the body, is in contact with body fluids such as joint fluid. Considering that this material used in the biomedical field is used in the body, it is advantageous to have hydrophilic properties. For biomaterials used in the body, high hydrophilicity or hydrophobicity is undesirable.

Table 1. Contact angle results.

Sample Name	Average Contact Angle (Degree)
Unadulterated	92.71
1% BA	90.63
5% BA	88.42
10% BA	87.79
20% BA	87.38
1% ZB	90.48
5% ZB	89.57
10% ZB	88.67
20% ZB	87.52

3.6. Scanning Electron Microscope (SEM) Results

According SEM images in Figure 6, boron addition did not cause significant differences in porous structure, morphology, aggregation, heterogeneous distribution. When compared with the control sample, it was interpreted that mechanical properties did not change negatively.

3.7. Antimicrobial Tests

S. epidermidis is very common contamination agent and it is a risk for patients with insufficient immune systems and permanent catheters. This bacterial risk also settles on the surface of medical prostheses and it is resistant to a wide range of antibiotics, including penicillin and methicillin. Antimicrobial test results are listed in Table 2 according to JIS Z 2801 Standard.

According to Table 2, zinc borate addition shows antimicrobial activity against *S.epidermidis* as well as boric acid addition over 5% concentration. These results suggested that boron-added bone cements will be an effective surface coating biomaterial to prevent bacterial growth. Also borate addition to bone cement can be used as an effective bioactive filler in order to increase antibiotic elution from the cement [32].

3.8. In Vitro Cytotoxicity Test With MTT

The results of cell viability obtained by MTT assay showed that 10% BA had no cytotoxic effects on L929 cells at each time point, while 20% BA, 10% ZB had cytotoxic effect on L929 cells at each time point. Although, the cytotoxic effect of 20% BA, 10% ZB, and 20% ZB, it was observed that bone cement formulations have positive effect on cell growth. Cell numbers were increased up to 7 days for each sample. Boric acid can be interpreted as non-toxic up to 10%, while 10%

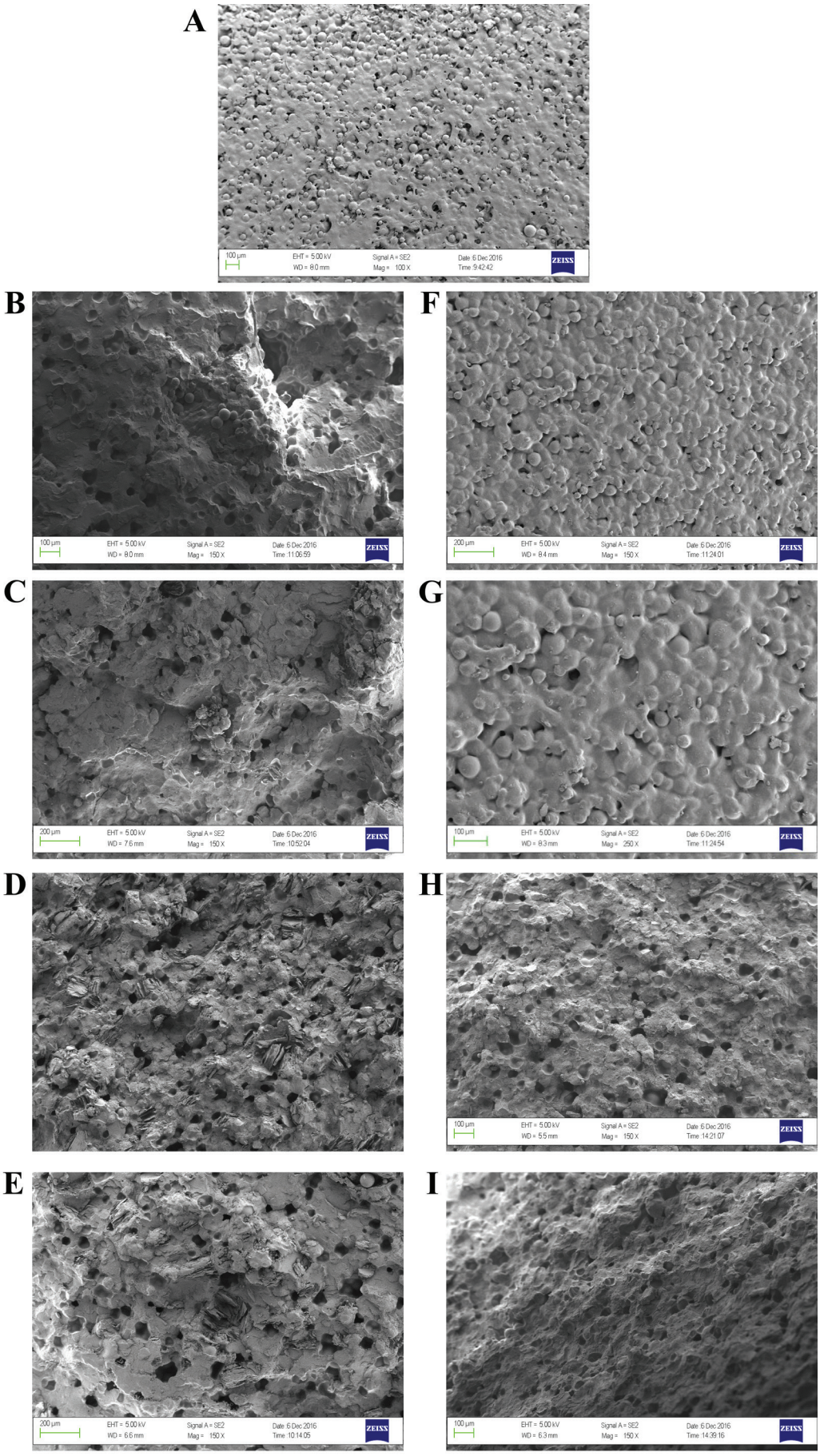

Figure 6. SEM Images of A) unadulterated, B) 1% BA, C) 5% BA, D) 10% BA, E) 20% BA, F) 1% ZB, G) 5% ZB, H) 10% ZB, I) 20% ZB samples in 150 X magnitude.

Table 2. Antimicrobial test results according to JIS Z 2801 Standard.

Sample	Test Organism	Test Sample 24 h (cfu/log)	Control 0 h (cfu/log)	Control 24 h (cfu/log)	R	Acceptance Criteria
5% ZB	*S. epidermidis*	0/0	396/2.60	123/2.09	2,09	≥2 log
5% zinc borate added sample effective on bacteria						
10% ZB	*S. epidermidis*	0/0	396/2.60	123/2.09	2,09	≥2 log
10% zinc borate added sample effective on bacteria						
20% ZB	*S. epidermidis*	0/0	396/2.60	123/2.09	2,09	≥2 log
20% zinc borate added sample effective on bacteria						
5% BA	*S. epidermidis*	81/1.91	396/2.60	123/2.09	0,18	≥2 log
5% boric acid added sample NOT effective on bacteria						
10% BA	*S. epidermidis*	0/0	396/2.60	123/2.09	2,09	≥2 log
10% boric acid added sample effective on bacteria						
20% BA	*S. epidermidis*	0/0	396/2.60	123/2.09	2,09	≥2 log
20% boric acid added sample effective on bacteria						

N (0^{th} hour): The number of live microorganisms in the sample, cfub/cm^2
N (24^{th} hour): The number of live microorganisms in the sample, cfu/cm^2
R: Antibacterial activity (logarithmic reduction)

and 20% zinc borate has toxic effect. Similarly, Hsu et al. evaluated the cytotoxicity of BA on L929 and UMR-106 cell by applying MTT assay and observed that increased BA concentration inhibited cell proliferation in a dose-dependent manner [33]. Furthermore, Uğur et al. reported that although there was no significant difference between zinc borate treated groups and non-zinc borate treated groups, zinc borate addition decreased the cell viability compared to control group [34]. This is the first study to use boron compounds in bone cement. This was a basic research trying to understand the effects of boron compounds in terms cell viability. It was understood that besides reducing temperature boric acid at low concentrations can be used for bone cement applications. It is also realized that zinc borate would not be suitable to use in medical applications due to toxic effects.

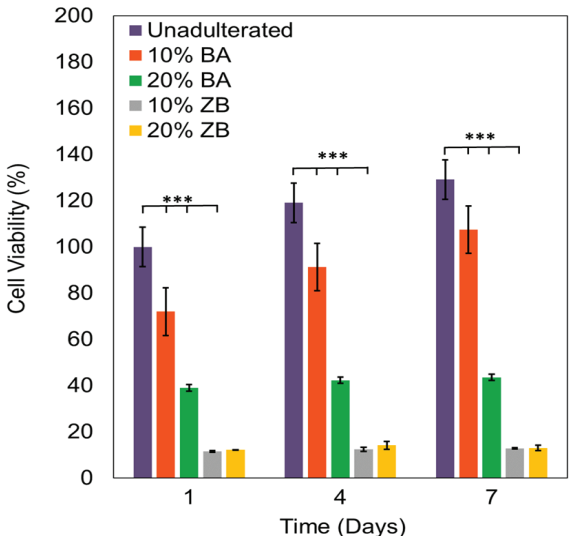

Figure 7. The percentage of increase in cell number at 1, 4 and 7 days after cultivation in extracts of bone cements.

4. Conclusions

Boric acid and zinc borate were added to the bone cement and their effects on polymerization process and characteristic properties were evaluated. In the polymerization process in unadulterated bone cement, the temperature increased to 80-95°C, while this value decreased to 45-65°C with boron additive. This process was monitored and photographed with a thermal camera. In addition, bone cements produced with boron additives were tested for *S. epidermidis* in accordance with the standard of "ISO 22196 Measurement of antibacterial activity on plastics surfaces" and it was found that they show antimicrobial activity. This study was the first study to use boron minerals in the bone cement formulation. We found that the incorporation of bone cement improved the thermal properties by means of reducing the heating of the bone cement. Boron minerals also provided antimicrobial properties and also the biocompatibility studies revealed that boron minerals affect the compatibility very slightly. Boron minerals also improved the hydrophilic character of the bone cement which is very critical for the biomedical applications. SEM images revealed that effective dispersion of the boron compounds was succeeded. Mechanical property measurements at elevated temperatures also proved that boron minerals have positive effect for the reinforcement of the bone cement.

There are many studies about boron-containing bioactive bone cements in the literature. According to these studies, boron addition has positive effects especially enhancing of angiogenesis, wound healing, osteogenesis as well as antimicrobial properties. These developments are quite new and these findings are key of the utilizing of boron-based bone cements in biomedical applications in the future.

Acknowledgement

This study was supported by Izmir Katip Celebi University as 2016-TYL-FEBE-0033 as a master thesis study of Muserref Caka. We would like to thank Prof. Ahmet Murat Bülbül, Prof. Mehmet Emin Erdil, and Dr. Ersin Kuyucu for the great support on initiation of this study. Prof. Seyhun Solakoglu was also very helpful for the biocompability tests. Also we would like to thank research assistant Metehan Atagür for his help during the experiments.

References

[1] Acarali, N. B., Tugrul, N., Derun, E. M., & Piskin, S. (2013). Production and characterization of hydrophobic zinc borate by using palm oil. International Journal of Minerals, *Metallurgy and Materials, 20*(11), 1081-1088.

[2] Alizadeh-Osgouei, M., Li, Y., & Wen, C. (2019). A comprehensive review of biodegradable synthetic polymer-ceramic composites and their manufacture for biomedical applications. *Bioactive Materials, 4*(1), 22-36.

[3] Ananth, H., Kundapur, V., Mohammed, H. S., Anand, M., Amarnath, G. S., & Mankar, S. (2015). A review on biomaterials in dental implantology. *International Journal of Biomedical Science, 11*(3), 113-120.

[4] Arora, M., Chan, E. K. S., Gupta, S., & Diwan, A. D. (2013). Polymethylmethacrylate bone cements and additives: A review of the literature. *World Journal of Orthopaedics, 4*(2), 67-74.

[5] Bailey, P. J., Cousins, G., Snow, G. A., & White, A. J. (1980). Boron-containing antibacterial agents: Effects on growth and morphology of bacteria under various culture conditions. *Antimicrobial Agents and Chemotherapy, 17*(4), 549-553.

[6] Baker, S. J., Ding, C. Z., Akama, T., Zhang, Y. K., Hernandez, V., & Xia, Y. (2009). Therapeutic potential of boron-containing compounds. *Future Medicinal Chemistry, 1*(7), 1275-1288.

[7] Benkovic, S. J., Baker, S. J., Alley, M. R. K., Woo, Y. H., Zhang, Y. K., Akama, T., Mao, W., Baboval, J., Rajagopalan, P. T. R., Wall, M., Kahng, L. S., Tavassoli, A., & Shapiro, L. (2005). Identification of borinic esters as inhibitors of bacterial cell growth and bacterial methyltransferases, CcrM and MenH. *Journal of Medicinal Chemistry, 48*(23), 7468-7476.

[8] Cheng, F., & Jäkle, F. (2011). Boron-containing polymers as versatile building blocks for functional nanostructured materials. *Polymer Chemistry, 2*(10), 2122-2132.

[9] Cook, G. E., Markel, D. C., Ren, W., Webb, L. X., McKee, M. D., & Schemitsch, E. H. (2015). Infection in orthopaedics. *Journal of Orthopaedic Trauma, 29*(Supplement 12), 19-23.

[10] Deliloglu-Gurhan, S. I., Vatansever, H. S., Ozdal-Kurt, F., & Tuglu, I. (2006). Characterization of osteoblasts derived from bone marrow stromal cells in a modified cell culture system. *Acta Histochemica, 108*(1), 49-57.

[11] Duan, G., Zhang, C., Li, A., Yang, X., Lu, L., & Wang, X. (2008). Preparation and characterization of mesoporous zirconia made by using a poly (methyl methacrylate) template. *Nanoscale Research Letters, 3*(3), 118-122.

[12] Funk, G. A., Burkes, J. C., Cole, K. A., Rahaman, M. N., & McIff, T. E. (2018). Antibiotic elution and mechanical strength of PMMA Bone cement loaded with borate bioactive glass. *Journal of Bone and Joint Infection, 3*(4), 187-196.

[13] Gemmell, K. D., & Meyer, D. (2018). Wear of ultra high molecular weight polyethylene against synthetic sapphire as bearing coating for total joint replacements. *Research&Development in Material Science, 6*(2), 560-567.

[14] Green, J. (1996). Mechanisms for flame retardancy and smoke suppression-A review. *Journal of Fire Sciences, 14*(6), 426-442.

[15] Guzzi, E. A., & Tibbitt, M. W. (2020). Additive Manufacturing of precision biomaterials. *Advanced Materials, 32*(13), 1-24.

[16] Hsu, C. F., Lin, S. Y., Peir, J. J., Liao, J. W., Lin, Y. C., & Chou, F. I. (2011). Potential of using boric acid as a boron drug for boron neutron capture therapy for osteosarcoma. *Applied Radiation and Isotopes, 69*(12), 1782-1785.

[17] Kuhn, L. T. (2005). Biomaterials. In J. D. Enderle, S. M. Blanchard, & J. D. Bronzino (Eds.) *Introduction to Biomedical Engineering*, 255-312.

[18] Kumar, S., Nehra, M., Kedia, D., Dilbaghi, N., Tankeshwar, K., & Kim, K. H. (2020). Nanotechnology-based biomaterials for orthopaedic applications: Recent advances and future prospects. *Materials Science and Engineering C, 106*, 110154.

[19] Lewis, G. (2011). Viscoelastic properties of injectable bone cements for orthopaedic applications: State-of-the-art review. *Journal of Biomedical Materials Research - Part B Applied Biomaterials, 98*(1), 171-191.

[20] Ma, Y., Cao, X., Feng, X., Ma, Y., & Zou, H. (2007). Fabrication of super-hydrophobic film from PMMA with intrinsic water contact angle below 90°. *Polymer, 48*(26), 7455-7460.

[21] Obinu, A., Gavini, E., Rassu, G., Riva, F., Calligaro, A., Bonferoni, M. C., Maestri, M., & Giunchedi, P. (2020). Indocyanine green loaded polymeric nanoparticles: Physicochemical characterization and interaction studies with caco-2 cell line by light and transmission electron microscopy. *Nanomaterials, 10*(133).

[22] Penyige, A., Deak, E., Kálmánczhelyi, A., & Barabás, G. (1996). Evidence of a role for NAD+-glycohydrolase and ADP-ribosyltransferase in growth and differentiation of Streptomyces griseus NRRL B-2682: inhibition by m-aminophenylboronic acid. *Microbiology, 142*(8), 1937-1944.

[23] Pivazyan, A. D., Matteson, D. S., Fabry-Asztalos, L., Singh, R. P., Lin, P. F., Blair, W., Guo, K., Robinson, B., & Prusoff, W. H. (2000). Inhibition of HIV-1 protease by a boron-modified polypeptide. *Biochemical Pharmacology, 60*(7), 927-936.

[24] Sheikh, Z., Najeeb, S., Khurshid, Z., Verma, V., Rashid, H., & Glogauer, M. (2015). Biodegradable materials for bone repair and tissue engineering applications. *Materials, 8*(9), 5744-5794.

[25] Shi, L., Li, D., Wang, J., Li, S., Evans, D. G., & Duan, X. (2005). Synthesis, flame-retardant and smoke-suppressant properties of a borate-intercalated layered double hydroxide. *Clays and Clay Minerals, 53*(3), 294-300.

[26] Sokmen, N., & Buyukakinci, B. Y. (2018). The usage of boron/ boron compounds in the textile industry and its situation in Turkey. CBU International Conference Proceedings, *Czechia, 6*, 1158-1165.

[27] Song, W. L., Wang, P., Cao, L., Anderson, A., Meziani, M. J., Farr, A. J., & Sun, Y. P. (2012). Polymer/boron nitride nanocomposite materials for superior thermal transport performance. *Angewandte Chemie, 124*(26), 6604-6607.

[28] Stańczyk, M., & Telega, J. (2002). Modelling of heat transfer in biomechanics - a review. Part II. Orthopaedics. *Acta of Bioengineering and Biomechanics, 4*(2), 3-31.

[29] Japanese Industrial Standard (2010). *Antimicrobial Products-Test for Antimicrobial Activity and Efficacy* (JIS Z Standard No. 2801: 2010).

[30] Ugur, A., Ceylan, O., Boran, R., Ayrikcil, S., Sarac, N., & Yilmaz, D. (2019). A new approach for prevention the oxidations and mutations: zinc borate. *Journal of Boron, 4*(4), 196-202.

[31] Vaishya, R., Chauhan, M., & Vaish, A. (2013). Bone cement. *Journal of Clinical Orthopaedics and Trauma, 4*(4), 157-163.

[32] Wang, Y., Li, H., Yao, J., Wang, X., & Antonietti, M. (2011). Synthesis of boron doped polymeric carbon nitride solids and their use as metal-free catalysts for aliphatic C-H bond oxidation. *Chemical Science, 2*(3), 446-450.

[33] Winkler, H. (2017). Treatment of chronic orthopaedic infection. *EFORT Open Reviews, 2*(5), 110-116.

[34] Yildiz, B., Seydibeyoğlu, M. Ö., & Güner, F. S. (2009). Polyurethane-zinc borate composites with high oxidative stability and flame retardancy. *Polymer Degradation and Stability, 94*(7), 1072-1075.

BOR DERGİSİ
JOURNAL OF BORON
https://dergipark.org.tr/boron

Bakır oksit ince filmlere bor katkısının metil mavisi üzerindeki fotokatalitik etkisinin araştırılması

Süleyman Kerli[1*], Mustafa Kavgacı[2,3]

[1]Kahramanmaras İstiklal Üniversitesi, Enerji Mühendisliği Bölümü, Kahramanmaraş, 46036, Türkiye
ORCID orcid.org/0000-0001-9774-3940
[2]Kahramanmaraş İstiklal Üniversitesi, Elbistan Sağlık Hizmetleri Meslek Yüksekokulu, Optisyenlik Bölümü, Kahramanmaraş, 46036, Türkiye
ORCID orcid.org/0000-0001-8747-0635
[3]Kahramanmaras Sütçü İmam Üniversitesi, Fizik Bölümü, Kahramanmaraş, 46040, Türkiye

MAKALE BİLGİSİ

Makale Geçmişi:
İlk gönderi 21 Eylül 2020
Kabul 20 Nisan 2021
Online 30 Haziran 2021

Araştırma Makalesi

DOI: 10.30728/boron.797645

Anahtar kelimeler:
Bakır oksit
Bor
Fotokatalitik
İnce film
Metil mavisi

ÖZET

Çalışmamızda, bakır oksit ve bor katkılı bakır oksit ince filmler sprey piroliz yöntemi ile sentezlenmiştir. Bu ince filmlerin fiziksel özelliklerini belirlemek için XRD ve SEM ölçümleri yapılmıştır. XRD sonuçları incelendiğinde filmlerin monoklinik yapıda olduğu görülmüştür. Elde edilen bu ince filmlerin fotokatalitik aktiviteleri incelenmiştir. Fotokatalitik inceleme ksenon lamba altında metil mavisi boyar madde kullanılarak yapılmıştır. Elde edilen sonuçlarda ince filmlerin metil mavisi üzerinde yüksek fotokatalitik bozunma oranlarının olduğunu göstermiştir. Fotokatalitik deney sonuçları, bor katkılama miktarının bozunma verimini ve reaksiyon süresini olumlu etkilediğini göstermiştir. Buradan bor katkılı bakır oksit ince filmlerin metil mavisi için etkili bir fotokatalizör olduğunu gösterdi. Sonuç olarak, bor katkılı bakır oksit ince filmlerin metil mavi boya içeren atık sularda fotokatalitik bozunma için potansiyel aday olduğu kabul edilebilir.

Investigation of the photocatalytic effect of boron doping to copper oxide thin films on methyl blue

ARTICLE INFO

Article History:
Received September 21, 2020
Accepted April 20, 2021
Available online June 30, 2021

Research Article

DOI: 10.30728/boron.797645

Keywords:
Copper oxide
Boron
Photocatalytic
Thin film
Methyl blue

ABSTRACT

In our study, copper oxide and boron doped copper oxide thin films were synthesized by spray pyrolysis method. XRD and SEM measurements were made to determine the physical properties of these thin films. When the XRD results were examined, it was seen that the films were in monoclinic structure. The photocatalytic activities of these thin films were investigated. Photocatalytic analysis was carried out under xenon lamp using methyl blue dye. The results obtained showed that thin films have high photocatalytic degradation rates on methyl blue Photocatalytic experiment results showed that the amount of boron doping positively affects the degradation efficiency and reaction time. From this, it has shown that boron doped copper oxide thin films are an effective photocatalyst for methyl blue. As a result, it can be accepted that boron doped copper oxide thin films are potential candidate for photocatalytic degradation in wastewaters containing methyl blue dye.

1. Giriş (Introduction)

Endüstriyel gelişim, beraberinde hava kirliliği, gürültü kirliliği ve su kirliliğine yol açmıştır [1]. Çevre kirliliğinin en önemlilerinden biri atık suların kirliliğidir. Su dünyada hayati bir ihtiyaçtır [2]. Dünyada hayatın devam edebilmesi için su kirliliği problemi çözülmelidir. Tabiatta ki su başta petrokimya, tekstil, ilaç sanayileri olmak üzere birçok endüstrilerin atıkları ile kirletilmektedir [3]. Atık sulardaki boyalar ve ağır metaller, ciddi çevre kirliliğine neden olmaktadır [4]. Tekstil ve diğer endüstrilerde kullanılan boyalar atık sulardaki kirliliğin nedenlerindendir. Tekstil boyaları kendiliğinden kolayca bozunmazlar [5]. Bu boyalar neticede ya çöp sahalarında çamur yığını olarak kalır yada akarsuları kirletir [6]. Bu kirleticiler suyun kalitesini düşürür, ekolojik sistem ve canlı organizmalar için ciddi risk oluşturur [7].

*Corresponding author: suleymankerli@yahoo.com

Geçtiğimiz son on yılda, fotokatalistler; ilaçlar, boyalar ve ağır metaller gibi tehlikeli çevresel kirleticileri güneş enerjisi kullanarak ortadan kaldırmadaki uygulamaları sebebiyle araştırmacıların ilgisini çekmiştir [8]. Metal oksit yarıiletken malzemeler metil mavisi giderimi için birçok araştırmada kullanılmıştır [9-11]. Yarıiletken malzeme olan CuO gaz sensörlerinde, güneş pillerinde, elektrokimyasal hücrelerde ve fotokatalizde yaygın olarak kullanılır [12-15].

Bakır oksit fotokatalist malzemeler, çevreye zarar vermeyen yapıları ve düşük maliyetleri sebebiyle dikkat çekicidir [16]. Bazı çalışmada bakır oksit ince filmlerin fotokatalist olarak kullanıldığı görülmektedir [17]. Wang ve arkadaşları CuO nano yapıların Rodamin B (RhB) boyasının bozunmasına yönelik fotokatalitik aktivitelerini araştırdılar. 20 mg CuO fotokatalizörü 50 ml RhB (10^{-5} mol/l) çözeltisi içerine uyguladılar. CuO nanoyapıların RhB boyasını 9 saat sonunda %96,7 bozduğunu gözlemlediler [18]. Zaman S. ve arkadaşları çiçeksi ve taç yaprak benzeri yapılarda CuO yapılar sentezlediler [19]. Bu yapıların RhB ve Metilen mavisi (MB) boyalarının bozunmasında ki fotokatalitik etkilerini inceledi. Fotokatalitik deneylerde 100 ml RhB ve MB (0,2 g/l) çözeltilerine 20 ml hidrojen peroksit ilave ettiler. Boyar madde çözeltilerinde fotokatalizör olarak 20 mg CuO parçacıkları kullandılar. CuO taç yaprak benzeri ve çiçeksi yapıların varlığında 5 saat sonra RhB'nin %85 ve %81, 24 saat sonra MB'nin %95 ve %72 oranlarında bozunduğunu tespit ettiler. Sahu ve arkadaşları termal buharlaştırma yöntemi ile Au-CuO nanohibrit ince filmler ürettiler. Bu ince filmleri 5 ml hacimde ki 5 µM'lık Malahit yeşili (MG) ve MB boyar madde çözeltilerine daldırdılar. Filmlerin fotokatalitik verimliliklerinin yüksek olduğunu gördüler ve boyar maddelerin 90 dakika içinde tamamen bozunmasına yol açtığını belirlediler [15].

Bakır tabanlı ince filmleri üretmek için; sprey piroliz tekniği, spin kaplama, daldırmalı kaplama, termal buharlaştırma, kimyasal buhar biriktirme, sol-jel, kimyasal banyo yöntemi gibi çeşitli teknikler kullanılmıştır [1,20-25]. Nano yapılı bakır oksit parçacık üretmek için birçok yöntem bulunmasına rağmen, çoğu zaman alıcıdır ve oldukça maliyetlidir [26].

İnce film kaplama yöntemine ve koşullarına bağlı olarak filmin yapısal ve optik özellikleri önemli ölçüde değişebilir [27]. Sprey piroliz yöntemi, geniş alanlı ince filmlerin üretilmesi için basit ve düşük maliyetli bir yöntemdir. Bu yöntem, ince filmlerin kontrol edilebilir bileşim ve mikro yapıya sahip orta sıcaklıklarda (100-500°C) üretilmesini sağlar. Bu yöntem yüksek kaliteli üretim ve vakum gerektirmemesi gibi avantaja da sahiptir [28]. Sprey piroliz yöntemi ile geniş yüzeylerin kaplanması mümkündür. Endüstriyel bir üretim için uygulaması kolaydır. Çalışmamızda bakır oksit ince filmler üretmek için, yukarıda belirtilen avantajları sebebiyle sprey proliz tekniği kullanılmıştır.

Endüstriyel atıklarından kaynaklanan ve tabii yaşamı tehdit eden kirliliklerin bertaraf edilmesi için farklı çözüm yöntemleri geliştirilmiştir. Fotokataliz bu yöntemler arasında ki en etkin metotlardan biridir. Bu çalışmada fotokataliz yöntemi kullanılarak dünya rezervlerinin büyük çoğunluğu ülkemizde bulunan bor elementinin fotokatalist olarak etkinliği incelenmiştir. Üretilen bor katkılı CuO ince filmlerin, metil mavisi boyar madde üzerindeki fotokatalitik performansı araştırılmıştır. Çalışmamızda elde edilen sonuçlar bor katkılı CuO ince filmler kullanılarak yapılabilecek fotokatalitik su arıtma uygulamaları için bir yol gösterici olacaktır.

2. Malzemeler ve Yöntemler (Materials and Methods)

Yapılan bu çalışmada, 50 ml 0,05 M'lık $CuCl_2 \cdot 2H_2O$ (Copper(II) chloride dihydrate 99%, Merck) çözeltisi için saf su kullanıldı. Çözeltilerdeki bor (H_3BO_3, Sigma Aldrich) konsantrasyonları, bakıra göre atomik yüzdesi %0, %10 ve %20 olarak ayarlandı. %0 bor katkılı filmler (CuO), %10 bor katkılı filmler (Cu10B), %20 bor katkılı filmler (Cu20B) olarak adlandırılacaktır. Alkol ve saf su ile temizlenerek, kurutulan cam altlıklar basınçlı havayla püskürtme tabancası ile kaplama yapılmıştır. Cam altlıklar püskürtme tabancasından 35 cm uzaklığa yerleştirildi. Homojen film kalınlığını elde etmek için, hava fırçasının yanal hızı 1 cm/s'ye ayarlandı. Hacimsel püskürtme hızı, hava basıncı düzenlenerek yaklaşık 0,3 ml/s'ye ayarlandı. Hazırlanan çözelti cam altlıklara 8 saniye süresince püskürtülmüş ve 30 saniye bekletilerek kaplama yapılmıştır. Kaplama esnasında taban sıcaklığı 400°C'ye ayarlanmıştır. Üretilen filmler daha sonra 450°C'de 2 saat süreyle tavlama işlemine tabi tutulmuştur.

Üretilen ince filmlerin kırınım deseni Philips X'Pert PRO marka XRD cihazı kullanılarak ölçülmüştür. Sentezlenen malzemelerin kristal boyutları aşağıda verilen Debye-Scherrer denklemi (1) kullanılarak hesaplanmıştır. *D*; kristal boyutu, *λ*: x-ışını dalgaboyu, β: (FWHM) radyan cinsinden değeri, θ: Bragg kırınım açısını göstermektedir.

$$D = 0.9\lambda/\beta cos\theta \quad (1)$$

Numunelerinin latis parametreleri (monoklinik yapı için; a≠b≠c; α=γ=90°; β≠90°) aşağıdaki denklem kullanılarak hesaplanmıştır. *d* düzlemler arası mesafe; *h*, *k*, *l* Miller indisleri; *a*, *b*, *c*, *β* latis parametreleridir.

$$1/d^2 = h^2/(asin^2b) + k^2/b^2 + l^2/(c^2sin^2b) - 2hlcos\beta/acsin^2\beta \quad (2)$$

Malzemelerin morfolojik özellikleri ZEISS EVO LS10 taramalı elektron mikroskobu incelenmiştir. İnce filmlerin optik özellikleri Shimadzu 1800 spektrofotometresi ile ölçülmüştür. Çalışmada üretilen filmlerin fotokatalitik performansı UV-Vis spektroskopi ile 300 W'lık

güneş simülatörü altında incelenmiştir. Fotokatalitik özelliklerinin belirlenebilmesi için boyar madde olarak metil mavisi (Alfa Aesar) kullanılmıştır. Metil mavisi için 425-725 nm arasında absorpsiyon spektrum taraması alınmıştır. Her filmin degradasyon ölçümü için metil mavisi çözeltisi (5 ppm (mg/L)) hazırlandı. 30 mL'lik metil mavisi çözeltilerinin içerisine bırakılan filmler, karanlık ortamda dengeye gelmesi için 30 dk bekletildi. Güneş simülatörü atındaki çözeltiden 2 mL numuneler alınarak ölçümleri gerçekleştirildi. Metil mavisi çözeltisi için maksimum absorbsiyon 598 nm olarak belirlendi.

Numunelerin boyar maddeler üzerindeki bozunma yüzdesi (B) aşağıdaki formülle hesaplanmıştır. C_0 başlangıç, C_t örnekleme zamanındaki ölçümü temsil etmektedir.

$$B = (1 - C_t/C_0) \times 100 \quad (3)$$

3. Sonuçlar ve Tartışma (Results and Discussion)

İnce filmlerin kristal yapısı, X-ışını kırınımı (XRD) cihazı kullanılarak ölçülmüştür. Bakır oksit ve bor katkılı bakır oksit ince filmlerin XRD sonuçları Şekil 1'de görülmektedir. İnce filmlerin XRD sonuçları PDF 00-045-0937 referansı ile uyumludur ve monoklinik yapıdadır. İnce filmlerin kırınım modelleri karşılaştırıldığında, aralarında ciddi fark gözlemlenmedi. İnce filmlerde katkılanan element ve bileşikleri ile ilgili herhangi bir pik tespit edilemedi [29-31]. Bu, tüm ince filmlerde aynı kristal fazın mevcut olduğu gösterir [32].

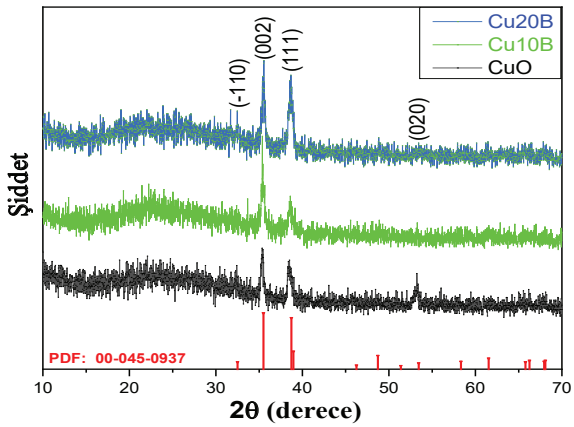

Şekil 1. Bakır oksit ve bor katkılı bakır oksit ince filmlerin XRD desenleri (XRD pattern of copper oxide and boron doped copper oxide thin films).

Debye-Scherrer formülü kullanılarak hesaplanan kristal boyutları Tablo 1'de gösterilmiştir. CuO, Cu10B ve Cu20B ince filmlerin kristal boyutu (002) için yaklaşık olarak sırasıyla 30 nm, 70 nm ve 53 nm olarak bulunmuştur. Genel olarak bor katkısıyla kristal boyutu arttığı görülmektedir. Ayrıca monoklinik yapıya ait latis parametreleri hesaplanmış ve Tablo 1'de gösterilmiştir. Tabloda görüldüğü üzere referans kodla verilen parametrelerle çok yakın değerler bulunmuştur. Bor katkısı ile bu değerlerdeki değişim de gözlenmiştir.

Üretilen bakır oksit ve bor katkılı bakır oksit ince filmlere ait yüzey morfolojisini gösteren SEM görüntüleri Şekil 2'de verilmiştir. SEM görüntülerinden, bor katkısı ile parçacık boyutlarındaki değişimler açıkça gözlenmektedir. CuO için ortalama parçacık boyutu 178 nm, Cu10B için 550 nm, Cu20B için ise 300 nm hesaplanmıştır.

Tablo 1. Kristal boyutu ve latis parametrelerinin değişimi (Change of crystal size and lattice parameters).

Numuneler (Samples)	a (Å)	b (Å)	c (Å)	Beta (°)	Kristal Boyutu (Crystal size, nm)
CuO	4.6948	3.4443	5.1382	99.1634	30
Cu10B	4.6902	3.4267	5.1397	99.2317	70
Cu20B	4.6955	3.4249	5.1218	99.6119	53
Referans kod (Reference code) 00-045-0937	4,6853	3,4257	5,1303	99,5490	

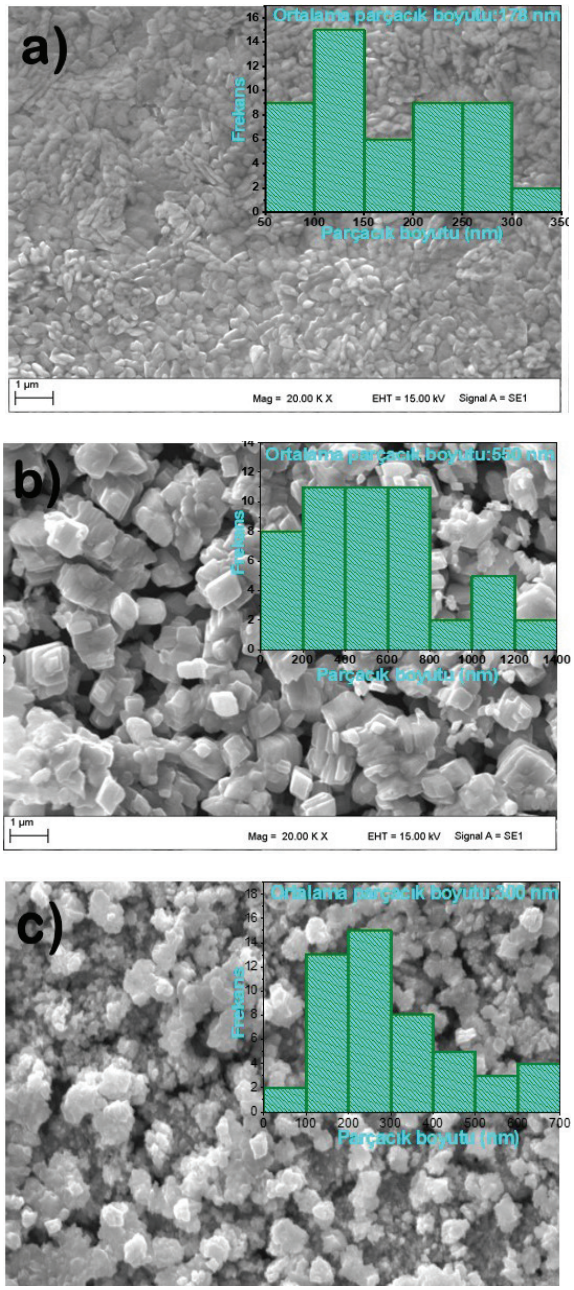

Şekil 2. SEM görüntüleri; a) CuO, b) Cu10B, c) Cu20B (SEM images; a) CuO, b) Cu10B, c) Cu20B).

İnce filmlerin UV-VIS Spektrofotometre ile optik soğurma ölçümleri yapılmıştır. Elde edilen datalar kullanılarak materyallerin $(\alpha h\nu)^2$~$h\nu$ değişim grafikleri çizilmiş ve bu grafikten yararlanılarak yasak enerji aralıkları bulunmuştur (Şekil 3). CuO için 1,96 eV, Cu10B için 1,9 eV ve Cu20B için 1,85 eV olarak bulunmuştur. CuO için bulunan yasak enerji bant aralığı literatürle uyum göstermektedir [13]. Bor katkısı arttıkça, yasak enerji bant aralığı da azalmıştır. Benzer sonuç M. Yuksel ve arkadaşları tarafından SILAR metodu ile bor katkılanmış bakır oksit ince filmler elde edilmiş, bor katkısı ile yasak enerji aralığının azaldığını bulmuşlardır [33].

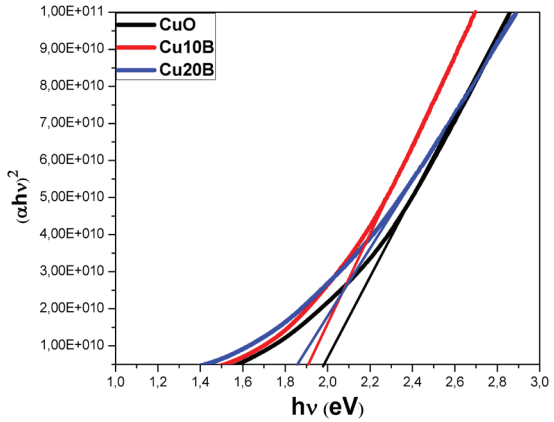

Şekil 3. CuO, Cu10B ve Cu20B filmlerine ait yasak enerji bant aralığı değerleri (Band gap values for CuO, Cu10B and Cu20B films).

İnce filmlerin, metil mavisinin zamana bağlı fotokatalitik bozunması oda sıcaklığında güneş simülatörü altında incelenmiştir. Numuneler için her 20 dakikada bir ölçüm alınmış ve 425-725 nm aralığında UV-Vis spektrofotometresinde taranmıştır. Metil mavisi bozulmaları UV-Vis absorpsiyon spektrumunda maksimum noktası 598 nm'de absorbanstaki düşüşler kaydedilerek belirlenmiştir. Şekil 4'de metil mavisinin güneş simülatörü altında absorbans grafiği görülmektedir. Boyar maddenin güneş simülatörü altında bozunması yaklaşık için %17'dir.

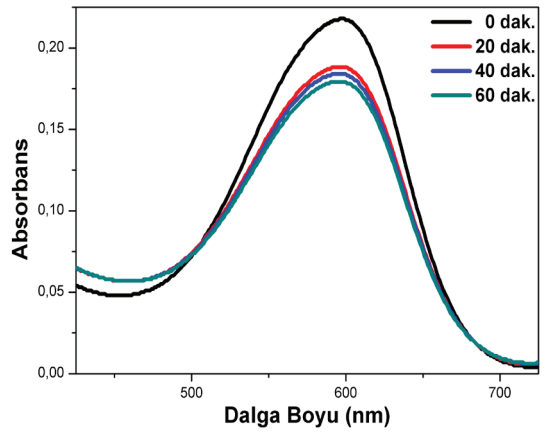

Şekil 4. Metil Mavisi ksenon lamba altında absorbans grafiği (Absorbance graph of Methyl Blue under xenon lamp).

Katkılı ve katkısız ince filmlerin metil mavisi için absorbans grafikleri Şekil 5'de verilmiştir. Şekil 5a'da CuO'in absorbans grafiğinden görüldüğü üzere; metil mavisinin 40. dakikaya kadar oldukça düzenli bir bozunmaya sahip olduğu ve 60. dakikada daha sert bir bozunma olduğu görülmektedir. Şekil 5b'de Cu10B'un absorbans grafiğinden anlaşıldığı üzere; düşüşlerin düzenli olduğu gözlenmektedir. Şekil 5c'de Cu20B'un absorbans grafiğinden incelendiğinde; metil mavisinin ilk 20 dakikada daha hızlı bozunduğu, 20-60 dk arasında daha düzenli bir bozunmaya sahip olduğu anlaşılmaktadır.

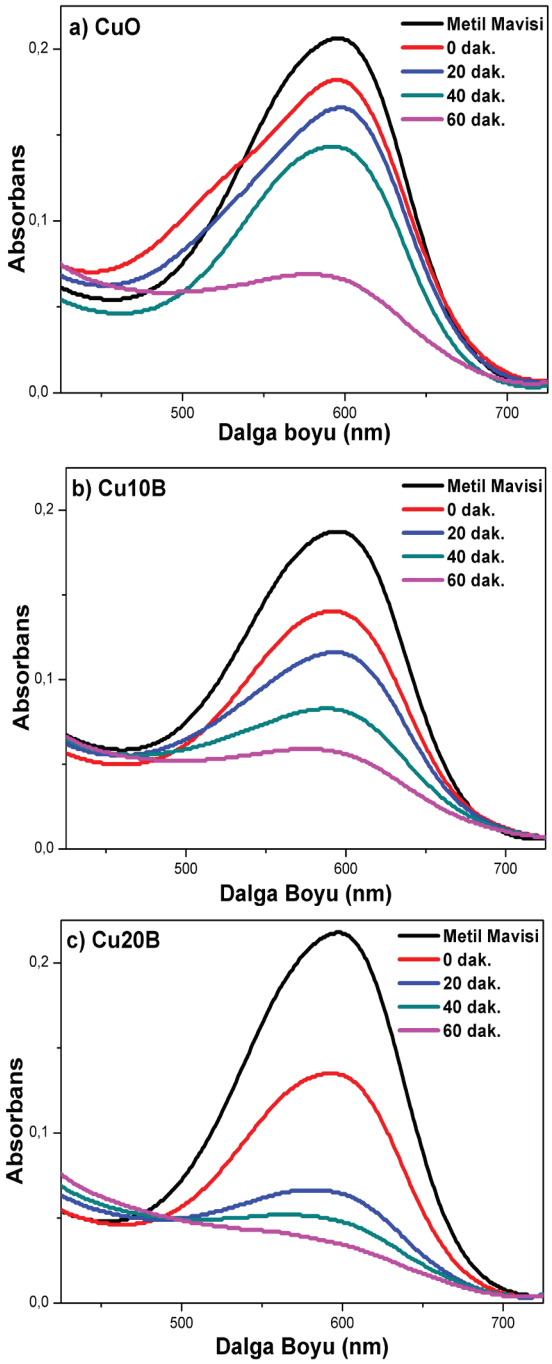

Şekil 5. a) CuO, b) Cu10B ve c) Cu20B ince film fotokatalizörlerinin metilen mavisi içerisindeki absorbans grafikleri (Absorbance plots of a) CuO, b) Cu10B and c) Cu20B thin film photocatalysts in methylene blue).

Şekil 6'da 60 dakika sonunda ince filmlerin metil mavisi boyar madde üzerindeki bozunmaları yaklaşık; CuO için %76, Cu10B için %82, Cu20B için %94 olduğu görülmektedir.

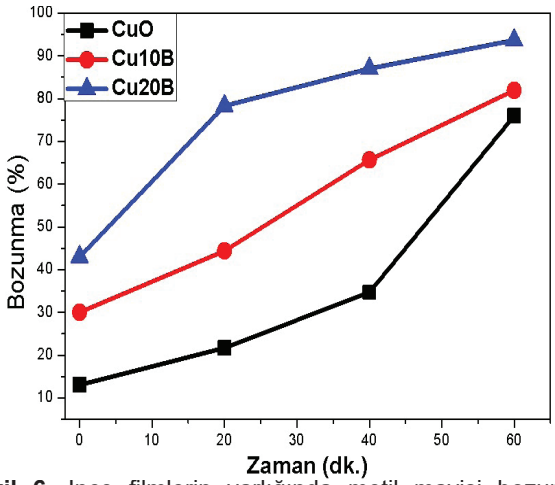

Şekil 6. Ince filmlerin varlığında metil mavisi bozunma yüzdesi grafiği (Degradation percentage plot of methylene blue with presence of thin films).

Şekil 7'de zamana karşı ln (C_0/C_t) grafiği verilmiştir. Grafikte ince filmlerin metil mavisi bozunma yüzdeleri ile uyumlu reaksiyon hız sabitlerine sahip oldukları görülmektedir. Grafik incelendiğinde; %94 ile en yüksek bozunma oranına sahip Cu20B'un reaksiyon hız sabiti açısından da en yüksek k değerine (k=0,057888) sahip olduğu görülmektedir.

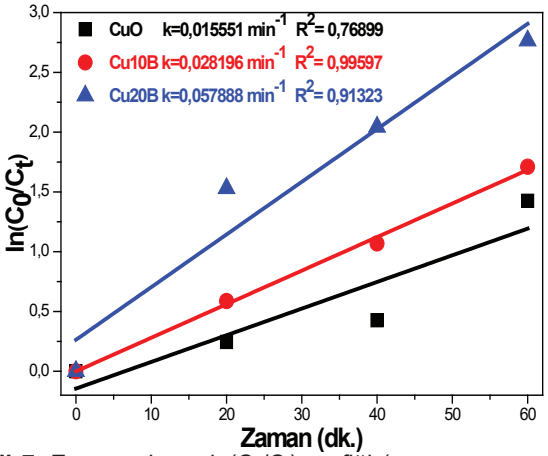

Şekil 7. Zamana karşı ln(C_0/C_t) grafiği (Graph of ln(C_0/C_t) vs time).

Genel olarak bütün ince filmlerin metil mavisinin bozunmasındaki oranın yüksek olduğu görülmekle birlikte bor katkısının artması ile bozunma oranının arttığı görülmektedir. Araştırmalar, hidroksil radikallerinin boyar madde bozunmasındaki en önemli etkenlerden biri olduğunu bildirmektedir. OH^- radikallerinin boya moleküllerini oksitler ve mineralleşmeye sebep olur [9]. Birçok çalışmada bor katkısının hidroksil gruplarını arttırdığı belirtilmiştir [34,35]. Dolayısıyla bu grupların artması ile fotokatalitik etki artmaktadır.

4. Sonuçlar (Conclusions)

Bakır oksit ve bor katkılı bakır oksit ince filmlerin yapısal ve fotokatalitik özellikleri araştırılmıştır. XRD analizinden numunelerin monoklinik yapıda olduğu anlaşılmıştır. Yine XRD sonuçlarından CuO, Cu10B ve Cu20B numunelerine ait kristal boyutları yaklaşık olarak sırasıyla 30 nm, 70 nm ve 53 nm olarak hesaplanmıştır. İnce filmlerin SEM görüntülerinde yapıların yüzeye iyice tutunduğu görülmüştür. İnce filmlerin UV-VIS Spektrofotometre ile optik soğurma ölçümleri yapılmıştır. UV-vis ölçümlerinden sentezlenen filmlerin yasak enerji aralıklarının: CuO için 1,96 eV, Cu10B için 1,9 eV ve Cu20B için 1,85 eV olarak bulunmuştur. Elde edilen sonuçlar, fotokatalitik bozunma oranlarının yüksek olduğunu göstermiştir. İnce filmlerin 60 dakika sonunda metil mavisi üzerindeki bozunumu sırasıyla CuO için %76, Cu10B için %82, Cu20B için %94 olduğu tespit edilmiştir. Bor katkılamanın fotokatalitik etkiye olumlu yönde etkilediği belirlenmiştir.

Kaynaklar (References)

[1] Sahu, K., Choudhary, S., Khan, S. A., Pandey, A., & Mohapatra, S. (2019). Thermal evolution of morphological, structural, optical and photocatalytic properties of CuO thin films. N*ano-Structures & Nano-Objects, 17*, 92-102.

[2] Shah, N. S., Rizwan, A. D., Khan, J. A., Sayed, M., Khan, Z. U. H., Murtaza, B., ... & Zaman, G. (2018). Toxicities, kinetics and degradation pathways investigation of ciprofloxacin degradation using iron-mediated H2O2 based advanced oxidation processes. *Process Safety and Environmental Protection, 117*, 473-482.

[3] Helal, A., Harraz, F. A., Ismail, A. A., Sami, T. M., & Ibrahim, I. A. (2017). Hydrothermal synthesis of novel heterostructured Fe2O3/Bi2S3 nanorods with enhanced photocatalytic activity under visible light. *Applied Catalysis B: Environmental, 213*, 18-27.

[4] Dong, Y., Xing, L., Hu, F., Umar, A., & Wu, X. (2018). Efficient removal of organic dyes molecules by grain-like α-Fe2O3 nanostructures under visible light irradiation. *Vacuum, 150*, 35-40.

[5] Hepel, M., & Hazelton, S. (2005). Photoelectrocatalytic degradation of diazo dyes on nanostructured WO3 electrodes. *Electrochimica Acta, 50*(25-26), 5278-5291.

[6] Sakthivel, S., Neppolian, B., Shankar, M. V., Arabindoo, B., Palanichamy, M., & Murugesan, V. (2003). Solar photocatalytic degradation of azo dye: comparison of photocatalytic efficiency of ZnO and TiO2. *Solar Energy Materials and Solar Cells, 77*(1), 65-82.

[7] Heidari, Z., Alizadeh, R., Ebadi, A., Oturan, N., & Oturan, M. A. (2020). Efficient photocatalytic degradation of furosemide by a novel sonoprecipited ZnO over ion exchanged clinoptilolite nanorods. *Separation and Purification Technology, 242*, 116800.

[8] Zhang, G., Chen, D., Li, N., Xu, Q., Li, H., He, J., & Lu, J. (2019). Fabrication of Bi2MoO6/ZnO hierarchical heterostructures with enhanced visible-light photocatalytic activity. *Applied Catalysis B: Environmental,*

250, 313-324.

[9] Kerli, S., Soğuksu, A. K., & Kavgacı, M. (2020). Production of nickel oxide nanostructure particles and their photocatalytic degradation of different organic dye. International *Journal of Modern Physics B, 34*(09), 2050081.

[10] Kerli, S., Alver, Ü., Eskalen, H., Uruş, S., & Soğuksu, A. K. (2019). Structural and morphological properties of boron doped V2O5 thin films: highly efficient photocatalytic degradation of methyl blue. *Russian Journal of Applied Chemistry, 92*(2), 304-309.

[11] Roza, L., Fauzia, V., Rahman, M. Y. A., Isnaeni, I., & Putro, P. A. (2020). ZnO nanorods decorated with carbon nanodots and its metal doping as efficient photocatalyst for degradation of methyl blue solution. *Optical Materials, 109*, 110360.

[12] Yang, L., Li, L., Yang, Y., Zhang, G., Gong, L., Jing, L., ... & Shi, K. (2013). Facile synthesis of Cu/CuxO nanoarchitectures with adjustable phase composition for effective NOx gas sensor at room temperature. *Materials Research Bulletin, 48*(10), 3657-3665.

[13] Dahrul, M., Alatas, H., & Irzaman. (2016). Preparation and optical properties study of CuO thin film as applied solar cell on LAPAN-IPB Satellite. *Procedia Environmental Sciences, 33*, 661-667.

[14] Morales, J., Sanchez, L., Martin, F., Ramos-Barrado, J. R., & Sanchez, M. (2005). Use of low-temperature nanostructured CuO thin films deposited by spray-pyrolysis in lithium cells. *Thin Solid Films, 474*(1-2), 133-140.

[15] Sahu, K., Choudhary, S., & Mohapatra, S. (2020). Fabrication of Au-CuO hybrid plasmonic nanostructured thin films with enhanced photocatalytic activity. *Materials Research Bulletin, 123*, 110707.

[16] Nguyen, D. C. T., Cho, K. Y., & Oh, W. C. (2019). Mesoporous CuO-graphene coating of mesoporous TiO2 for enhanced visible-light photocatalytic activity of organic dyes. *Separation and Purification Technology, 211*, 646-657.

[17] Dasineh-Khiavi, N., Katal, R., Kholghi-Eshkalak, S., Masudy-Panah, S., Ramakrishna, S., & Jiangyong, H. (2019). Visible light driven heterojunction photocatalyst of CuO-Cu2O thin films for photocatalytic degradation of organic pollutants. *Nanomaterials, 9*(7), 1011.

[18] Wang, L. J., Zhou, Q., Liang, Y., Shi, H., Zhang, G., Wang, B., ... & Wang, W. Z. (2013). Size effect and enhanced photocatalytic activity of CuO sheet-like nanostructures prepared by a room temperature solution phase chemical method. *Applied Surface Science, 271*, 136-140.

[19] Zaman, S., Zainelabdin, A., Amin, G., Nur, O., & Willander, M. (2012). Efficient catalytic effect of CuO nanostructures on the degradation of organic dyes. Journal of *Physics and Chemistry of Solids, 73*(11), 1320-1325.

[20] Saravanan, V., Shankar, P., Mani, G. K., & Rayappan, J. B. B. (2015). Growth and characterization of spray pyrolysis deposited copper oxide thin films: Influence of substrate and annealing temperatures. *Journal of Analytical and Applied Pyrolysis, 111*, 272-277.

[21] Nalbant, A., Ertek, Ö., & Okur, I. (2013). Producing CuO and ZnO composite thin films using the spin coating method on microscope glasses. *Materials Science and Engineering: B, 178*(6), 368-374.

[22] Zhang, H. L., Zhao, G. Y., & Xu, L. Z. (2013). Preparation of the photosensitive copper complex and CuO film pattern. *Applied Surface Science, 274*, 397-400.

[23] Koh, T., O'Hara, E., & Gordon, M. J. (2013). Growth of nanostructured CuO thin films via microplasma-assisted, reactive chemical vapor deposition at high pressures. *Journal of Crystal Growth, 363*, 69-75.

[24] Pugazhendhi, A., Kumar, S. S., Manikandan, M., & Saravanan, M. (2018). Photocatalytic properties and antimicrobial efficacy of Fe doped CuO nanoparticles against the pathogenic bacteria and fungi. *Microbial Pathogenesis, 122*, 84-89.

[25] Durdu, B. G., Alver, U., Kucukonder, A., Söğüt, Ö., & Kavgaci, M. (2013). Investigation on zinc selenide and copper selenide thin films produced by chemical bath deposition. *Acta Physica Polonica, A., 124*(1), 41-45.

[26] Chiang, C. Y., Aroh, K., & Ehrman, S. H. (2012). Copper oxide nanoparticle made by flame spray pyrolysis for photoelectrochemical water splitting–Part I. CuO nanoparticle preparation. *International Journal of Hydrogen Energy, 37*(6), 4871-4879.

[27] Cruz, M. A., Sanchez-Martinez, D., & Torres-Martínez, L. M. (2020). CuO thin films deposited by DC sputtering and their photocatalytic performance under simulated sunlight. *Materials Research Bulletin, 122*, 110678.

[28] Selleswari, D., Meena, P., & Mangalaraj, D. (2019). Design of CuO/SnO2 heterojunction photocatalyst with enhanced UV light-driven photocatalytic activity on congo-red and malachite green dyes. *Journal of the Iranian Chemical Society, 16*(6), 1291-1300.

[29] Mishra, R. K., Kumar, V. B., Victor, A., Pulidindi, I. N., & Gedanken, A. (2019). Selective production of furfural from the dehydration of xylose using Zn doped CuO catalyst. *Ultrasonics Sonochemistry, 56*, 55-62.

[30] Tawfik, W. Z., Khalifa, Z. S., Abdel-Wahab, M. S., & Hammad, A. H. (2019). Sputtered cobalt doped CuO nano-structured thin films for photoconductive sensors. *Journal of Materials Science: Materials in Electronics, 30*(2), 1275-1281.

[31] Molavi, R., & Sheikhi, M. H. (2020). Facile wet chemical synthesis of Al doped CuO nanoleaves for carbon monoxide gas sensor applications. *Materials Science in Semiconductor Processing, 106*, 104767.

[32] Lugo-Ruelas, M., Amézaga-Madrid, P., Esquivel-Pereyra, O., Antúnez-Flores, W., Pizá-Ruiz, P., Ornelas-Gutiérrez, C., & Miki-Yoshida, M. (2015). Synthesis, microstructural characterization and optical properties of CuO nanorods and nanowires obtained by aerosol assisted CVD. *Journal of Alloys and Compounds, 643*, S46-S50.

[33] Yuksel, M., Pennings, J. R., Bayansal, F., & Yeow, J. T. (2020). Effect of B-doping on the morphological, structural and optical properties of SILAR deposited CuO films. *Physica B: Condensed Matter, 599*, 412578.

[34] Liu, Z., Liu, J., Wang, H., Cao, G., & Niu, J. (2016).

Boron-doped bismuth oxybromide microspheres with enhanced surface hydroxyl groups: synthesis, characterization and dramatic photocatalytic activity. *Journal of Colloid and Interface Science, 463*, 324-331.

[35] Wang, W. K., Chen, J. J., Gao, M., Huang, Y. X., Zhang, X., & Yu, H. Q. (2016). Photocatalytic degradation of atrazine by boron-doped TiO2 with a tunable rutile/anatase ratio. *Applied Catalysis B: Environmental, 195*, 69-76.

BOR DERGİSİ
JOURNAL OF BORON
https://dergipark.org.tr/boron

The synthesis of NiO@N-doped reduced graphene oxide and its application for hydrogen generation from ammonia borane

Derya Öncel Özgür[1*]

[1]Gazi University, Department of Chemical Engineering, Ankara, 06570 Turkey,
ORCID orcid.org/0000-0001-5490-0707

ARTICLE INFO

Article history:
Received December 14, 2020
Accepted May 10, 2021
Available online June 30,2021

Research Article

DOI: 10.30728/boron.840655

Keywords:
Ammonia borane
Catalyst
Hydrogen storage
N-doped reduced graphene oxide

ABSTRACT

Ammonia borane (AB) is considered a highly promising candidate among the chemical hydrogen storage compounds. The improvement of efficient and low-cost catalysts is key to comprehending a highly efficient hydrogen generation reaction. In this study, the synthesis of non-noble nickel oxide on nitrogen-doped graphene (NiO@N-rGO) was carried out and its efficiency towards the catalytic dehydrogenation of AB was investigated under mild conditions (25-50°C). The synergic effect between NiO and nitrogen-doped rGO has increased the performance of the catalyst. As a result, the turnover frequency (63 mol H_2 min^{-1} (mol Ni)$^{-1}$ of NiO@N-rGO) is which higher than most of the Ni-based catalyst. The activation energy (E_a) measured to be 48.7 kJ mol^{-1} is among the values of the most active catalysts.

1. Introduction

The fuel cell has been widely recognized as highly favorable for large energy systems for many years, however, the recent concern has focused on the small portable power sources [1]. It was postulated that the hydrogen-based portable or mobile energy systems would be desirable to utilize by using chemical hydrides. Up to now the most of the chemical hydride surveys have been conducted taking into consideration the hydrolysis of $NaBH_4$ due to several advantages [2-6]. Although $NaBH_4$ appears an attractive candidate for portable or mobile devices under mild conditions, it suffers from the requirement of a highly basic NaOH solution which ensures its chemical stability to avoid self-hydrolysis in water [7].

Scientific approaches demonstrated that the most applicable method to overcome the main challenges on the on-board system has been viewed as chemical hydrogen storage [8]. Among them, B-N-H compounds, especially the ammonia-borane complex, (AB, NH_3BH_3) has received increasing attention as a promising for on-board hydrogen application due to having high hydrogen content (19.6 wt%), eco-friendly source, and high stability as opposed to $NaBH_4$ [9]. After the synthesis of AB in 1955 [10], it has been used as the reducing agent [11] and the main precursor to produce the other boron-containing materials, such as metal amidoborane [12], however, the interest in AB has unexpectedly shifted to its capability as a high-capacity of hydrogen storage materials. The electronegativity discrepancy between nitrogen and boron accounts for the polarization of the hydrogens in AB, the hydridic B-H, and protic N-H, readily leading to dissociation of B-N bonding and consequently promoting the hydrogen releasing [13]. The releasing hydrogen from AB in a general approach could be carried out in two methods: (i) thermolysis at a higher temperature (ii) the catalytic release in the non-aqueous solvent or aqueous solvent named the hydrolysis. The hydrolysis reaction could release up to 3 moles hydrogen per 1 mole of AB only in the presence of an appropriate catalyst at the ambient condition.

There appears to be numerous data published up to this point regarding noble metals, transition metals, and their bimetallic or multimetallic hybrids. Among the catalysts tested, it can be made inferences that noble based metal catalysts such as Pt, Rh, Ru, or Pd exhibit the highest activity than that of most transition-based metal catalysts toward AB hydrolysis. Hence, for practical use, the inexpensive and efficient catalytic materials are a favorable substitute for precious-metal-based catalysts. It was recently found that the rational design of the bifunctional or multifunctional combination including transition metals or other counterparts (oxides, hydroxides, and phosphides) and carbon-based materials makes the transition metals competitive for increasing the catalytic reactivity [14].

*Corresponding author: deryaoncel@gazi.edu.tr

Among the transition metals, Ni-based catalyst has been considered as one of the most promising candidates. However, the success of nano-based catalyst strongly depends on the stability of Ni nanoparticles (NPs) since the nano-size particles tend to build-up more stable agglomerates, which could lead to loss of active sites and show somewhat lower catalytic activity. It is well accepted that those kinds of problems could be modified with the incorporation of supports like carbon [15], graphene oxide [16], carbon nanotubes [17]. So far, only a few studies have investigated the effect of nitrogen-doped graphene oxide as a supports [18,19]. The present study aims to offer that the hybrid structured nitrogen-doped reduced graphene oxide (N-rGO) could be an proceeding support for enhancing the catalytic activity of NiO nanoparticles. This perspective for the first time emphasizes the rational design of NiO@N-doped reduced graphene oxide nanoparticles for the hydrogen generation form AB. Regarding the proposed model, NiO can enable the adoption of H_2O (H-OH) with dissociation proceeding favorably, and N-rGO would render electron interactions as an conductive support, thus reveals the synergic effects. A graphene-based assemble has been considered as ideal supporting material due to its outstanding intrinsic properties such as a large surface area with a tunable nanoscale morphology and porosity and good electrical conductivity [19,20]. Furthermore, the surface of nitrogen-doped rGO with extraordinarily electronic and chemical structure could possess a substantially high positive charge on the carbon atoms adjacent to nitrogen dopant. This helps the further improvement of the catalytic performances of NiO-based catalysts. Given the aforementioned design, it would be expected that the NiO@N-rGO would provide kinetically accelerating the hydrogen evaluation rate from AB.

2. Materials and Methods

2.1. Synthesis of Nitrogen-Doped Reduced Graphene Oxide (N-rGO)

The synthesis of graphene oxide (GO) from flake graphite powder was carried out by using a modified Hummers' method [21,22]. As-synthesized GO (100 mg in 50 mL water) was dispersed by sonication for 30 min. Then, 100 mg of urea was added with magnetically stirring for 12 hours. The mixture was then transferred into a Teflon-sealed autoclave and kept at 180°C for 12 hours. The nitrogen-doped graphene sheets were centrifuged and obtained after being washed with deionized water several times. Finally, the collected samples were dried in the oven at 60°C to obtain in powder form and denoted as N-rGO.

2.2. Synthesis of Nickel Oxide Nanocomposites on Nitrogen-Doped Reduced Graphene Oxide (NiO@N-rGO)

As-synthesized 20 mg N-rGO in the previous stage was put into the 30 mL of water in a flask and kept under ultrasound for 30 min. As the percent of Ni content was to be 20% by weight, the required amount of $NiSO_4.6H_2O$ was then added into the mixed solution and heated up to 60°C, and kept at this temperature during the reduction. The pH was adjusted to 10 with 0.5 M NaOH before initiating the reduction with hydrazine hydrate. The reaction started when the 2 mL of hydrazine hydrate was added to the flask with stirring for 6 hours at 60°C. The sample was centrifuged and wash using distilled water at least three times. The final product was named NiO@N-rGO after drying in an oven at 60°C.

2.3. Structural Characterization

The structure of the as-prepaid composites was characterized by X-ray diffraction (XRD) by employing Cu-Kα radiation with λ at 1.5418 Å; and X-ray photoelectron spectroscopy (XPS) data collected on an X-ray photoelectron instrument (K-alpha, Thermofisher Scientific Company) equipped with Al Kα radiation at a power of 150 W and a voltage of 12 kV. FT-IR analaysis was applied on a dry powder equipped with a KBr beam splitter in the frequency range of 4000 to 650 cm^{-1} at room temperature. The surface structure characterizations were performed on a Quanta 400F Field Emission scanning electron microscope.

2.4. Hydrogen Generation Measurements

The volume of hydrogen releasing during the dehydrogenation of AB in the presence of NiO@N-rGO catalysts was determined by monitoring the traditional water-displacement method. In a typical experiment, NiO@N-rGO catalyst (10 mg in 5 mL water) was introduced into the three-necked round-bottom flask and magnetically stirred. The reaction temperature was kept constant at the desired setting during all reaction periods by using a water bath. Once the solution of AB (0.15 M, 10 mL) was inserted into the reaction medium via the pressure equalization apparatus, the hydrolysis reaction simultaneously took place and recorded the volume of the hydrogen.

3. Results and Discussion

3.1. Characterization of NiO@N-rGO

The X-ray diffraction (XRD) patterns of the NiO@N-rGO, GO, and N-rGO are shown in Figure 1a and Figure 1c. The GO has a sharp diffraction peak centered at 2θ=11.1° in Figure 1c, yet, this peak entirely disappeared and a broad peak located at around 24.5° indexed to the (002) plane of graphitic materials was ascertained for both reduced samples (N-rGO and NiO@N-rGO), confirming the arrangement of the graphitic crystal with composed of few-layer stacked graphene nanosheets [23]. Nitrogen doping in graphene leads to consisting of defect site and destructing of carbon lattice, which turns out to be low crystallinity as shown in Figure 1a [24]. The XRD pattern of NiO major diffraction peaks is ascribed to NiO(111),

NiO(200), NiO(220), and NiO(311), respectively [25]. The mean particle size of NiO nanoparticles was calculated by using the Debye-Scherrer's formula [26] (D=0.89/(βcosθ)) where β is the full width at half maximum (FWHM), taken in radians, λ is 1.5418 for Cu-Kα radiations. The mean particle size obtained from the reflection (200) at 43.5° is 2.6 nm and the most intense reflection (220) is 5.4 nm.

FTIR spectroscopy was performed to investigate the functional groups in the NiO@N-rGO hybrids. As shown in Figure 1b, the spectrum of NiO@N-rGO shows (i) a broad peak at 3425 cm^{-1}, and a peak at 1627 cm^{-1} which is a typical stretching vibration and bending vibrations of hydroxyl groups, respectively [27,28] (ii) Absorption peaks at 2923 and 2850 cm^{-1} due to the C-H stretching mode of the CH_2 groups [24] (iii) the peak is at 1265 cm^{-1} belongs to of the C-N bond, indicating that nitrogen atoms were successfully doped into the carbon matrix [29] (iv) the C-N stretching and N-H stretching at 1382 and 1462 cm^{-1} respectively [24] (v) the bands around 624 and 470 cm^{-1} belongs to the Ni-O vibrations and Ni-O-H bending vibrations, individually [30,31]. The FTIR observation indicates both the addition of nitrogen heteroatom in rGO and the evidence of NiO on the surface of N-rGO.

X-ray photoelectron spectroscopy (XPS) was used to search the detailed surface chemical composition and the oxidation state of the NiO@N-rGO hybrid composite (Figure 2). The survey spectrum (Figure 2a) confirms that the as-prepared NiO@N-rGO is comprised of C, N, O, and Ni elements. Corresponding to the survey XPS measurements, the weight percentages of C, N, O, and Ni in the composite are found as 63.11, 1.95, 31.02, and 3.40 wt%, respectively. Figure 2b displays the C 1s spectrum displays the five deconvoluted peaks of C atoms. The main carbon peak at 284.8 eV seems to be predominantly C-C bond with sp^2 hybridization as indicated by the presence of graphene [32]. The other peaks have appeared at 285.8 eV, 286.6 eV, and 287.9 eV coincided with C-N, C═O, C-O (287.9 eV), and O-C═O (289.1 eV) [33] species, respectively. Besides, the N 1s spectrum in Figure 2c exhibits three peaks at 398.1, 399.5, and 400.8 eV, designated to the pyridinic N, pyrrolic N, and graphitic N, which are the typical three sates of N elements incorporated into rGO [32]. The Ni 2*p* XPS spectra (Figure 2d) presents the characteristic $2p_{3/2}$ and $2p_{1/2}$ doublet caused by spin-orbital coupling. Moreover, their satellite at 861.59 eV and 879.78 eV are observed, which proving the existence of NiO [34,35]. As a result, it is sensible to infer that the NiO@N-rGO composite was synthesized.

The scanning electron microscopy (SEM) analysis was utilized to elucidate the surface morphological properties and microstructure of the as-prepaid catalysts. The higher magnification SEM images in Figure 3a clearly demonstrated the existence of the ripped and wrinkled sheets as proof of the nitrogen-doped rGO with exfoliated few layers. Meanwhile, Figure 3b also confirmed that the NiO particle was uniformly anchored onto the graphene sheets.

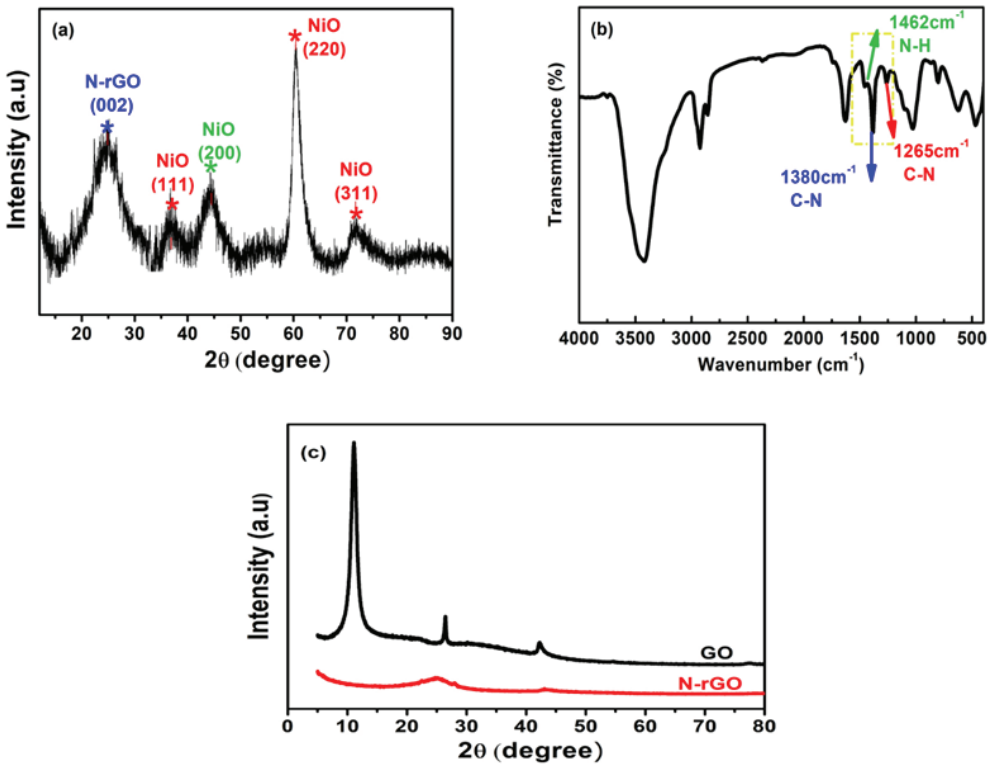

Figure 1. (a) The XRD and (b) FTIR spectra of the NiO@N-rGO (c) XRD spectra of GO and N@rGO.

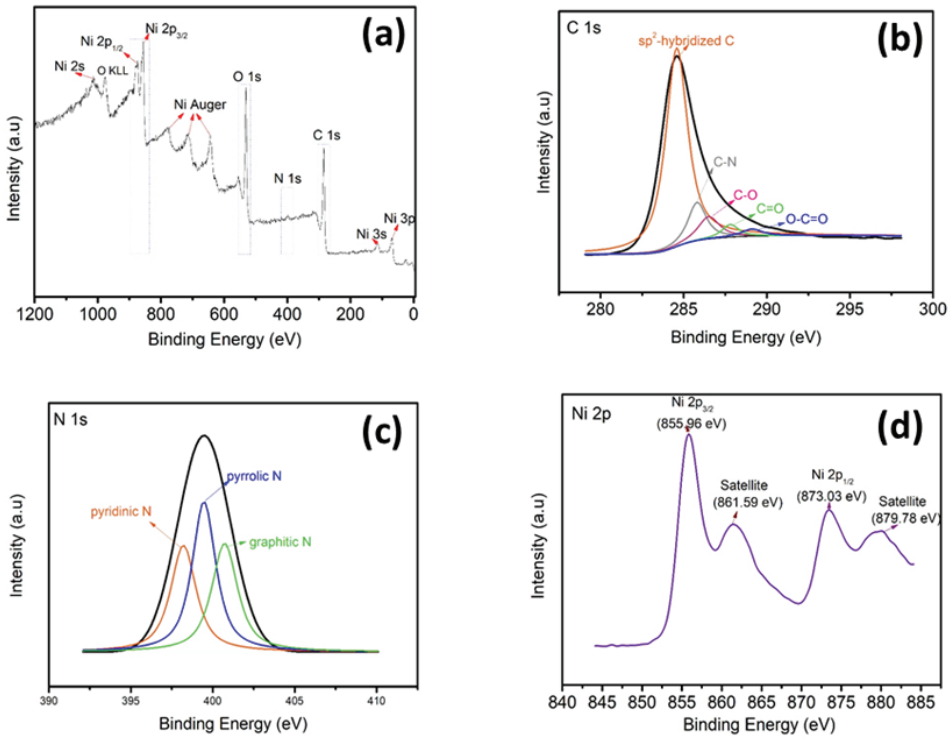

Figure 2. XPS measurements (a) Survey spectra of NiO@N-rGO (b) High resolution C 1s XPS spectra; (c) High resolution N 1s XPS spectra; (d) High resolution Ni 2p XPS spectra.

3.2. Catalytic Activities for Hydrolysis of AB Over NiO@N-rGO

The catalytic activities for hydrolysis of AB were investigated by monitoring the amount of H_2 evaluation at regular intervals. Figure 4a represents the plots of the volume of hydrogen collected gas versus the reaction time in the presence of the as-prepaid NiO@N-rGO catalyst, indicating high catalytic activity for the hydrolysis reaction of AB. Except for the room temperature measurements, it was observed that nearly 3 equivalent of hydrogen per ammonia borane was released in 40 min in Figure 4b, corresponding to the turnover frequency (TOF) value of 63 mol H_2 min^{-1} (mol Ni)$^{-1}$ at temperatures above 25°C. The TOF values and activation energies of the hydrolysis of AB solution catalyzed by previously reported Nickel-based catalysts are summarized in Table 1 for comparison. The TOF value of NiO@N-rGO catalyst is higher than most previously published non-noble Ni metal-based NPs (Table 1) and even many noble metal-based NPs [36-38]. The results confirm that the positive synergistic effect between N-doped rGO and NiO NPs was improved the hydrogen production rate during AB dehydrogenation.

As shown in Figure 5, plotting the initial and final concentration differences versus time result in a straight line under our experimental conditions, implying that the hydrolysis of AB over NiO@N-rGO is a zero-order reaction with regard to AB concentration, and could be described as Eqn. 1. It means that the hydrogen production rate is controlled by the surface reaction. It is well accepted the apparent activation energy is another important factor influencing the reaction kine-

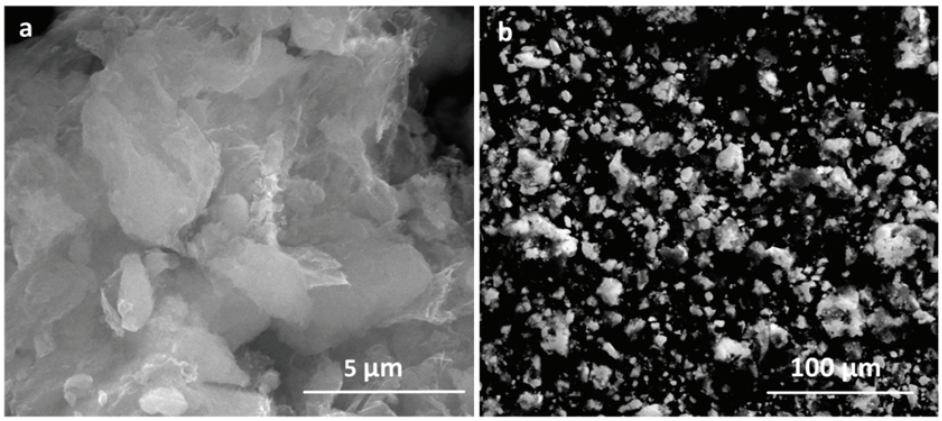

Figure 3. SEM micrographs of the NiO@N-rGO catalyst with a) 5 µm scale b) 100 µm scale.

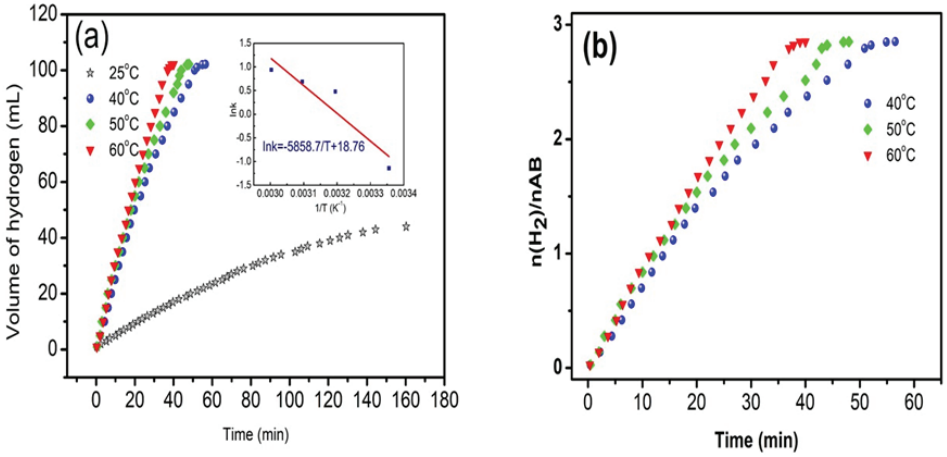

Figure 4. (a) Volume of H_2 during hydrolysis of AB as a function of time over NiO@N-rGO at different temperatures and the Arrhenius equation of ln *k versus* 1/T (b) The curves of equivalents H_2 per mole of AB over NiO@N-rGO at different temperatures.

tics. Moreover, the reaction rate constant k could be associated with activation energy (E_a) by the Arrhenius equation (Eqn. 2). The rate constant k's at various temperatures in the range 25-60°C were determined from the slope of the linear part of each plot (Figure 5). The inset of Figure 4a displays the lnk vs 1/T (Arrhenius plot), from which the activation energy was calculated to be 48.7 kJ·mol^{-1}. The activation energy value of the as-prepaid NiO@N-rGO catalyst is acceptable if compared to that of other Ni-based catalysts in Table 1. A: pre-exponential factor, R: universal gas constant, and T: temperature in K.

$$r = \frac{-3d[NH_3BH_3]}{dt} = \frac{d[H_2]}{dt} = k \qquad (1)$$

$$k = Aexp(-\frac{E_a}{RT}) \qquad (2)$$

The improved activity of the as-prepaid catalyst could be originated from three main reasons: (I) the small size of the particles by calculating the Debye-Scherrer equation, leading to a better dispersion on the graphene support (II) NiO could easily promote the adsorption of water (H-OH), in which hydrogen turns out to be electropositive. This initiation steps forward the reaction into the tempt of electronegative H in AB [14], and help the further hydrolysis to attack the B-N bonds [49] (III) The interaction between NiO and N-rGO could build up a new electronic structure, which differs from their pure states [49]. Meanwhile, it was suggested that with the incorporation of any metallic compound such as Ni, or Pt by acting as a bridge between NiO and graphene layer, the reaction kinetics would further accelerate by facilitating the electron transfers.

4. Conclusions

In summary, this study demonstrated a facile method for the synthesis of nitrogen-doped graphene oxide supported NiO nanocomposites, and their activities against hydrogen production from the AB under mild conditions. The nitrogen-doped rGO was synthesized in a one-pot hydrothermal method by using urea as reducing-doping agents. NiO NPs were anchored onto N-rGO by reduction method with hydrazine hydrate. Moreover, this method can be widespread usage of the other graphene supported NPs for future applicati-

Table 1. Activities in terms of TOF and activation energy values of the Ni-based catalysts used for the hydrolysis of AB.

Catalysts	TOF ($molH_2$ $molcat^{-1}$ min^{-1})	E_a, (kJ/mol)	Reference
NiO@N-rGO	63	48.7	This study
Ni sphere	19.6	27	[39]
Ni/C	8.8	28	[40]
$NiCl_2$	0.40	-	[41]
PVP stabilized Ni NPs	4.5	-	[42]
NiP/rGO	13.3	34.7	[43]
Ni/SiO_2-$CoFe_2O_4$	5.3	68.2	[44]
Ni/BN	1.25	63.2	[45]
Ni/Ni_2P	68.3	44.99	[46]
Ni@TiN-NTs	11.73	52.05	[47]
$Ni_{12}P_5$	23	50.4	[48]

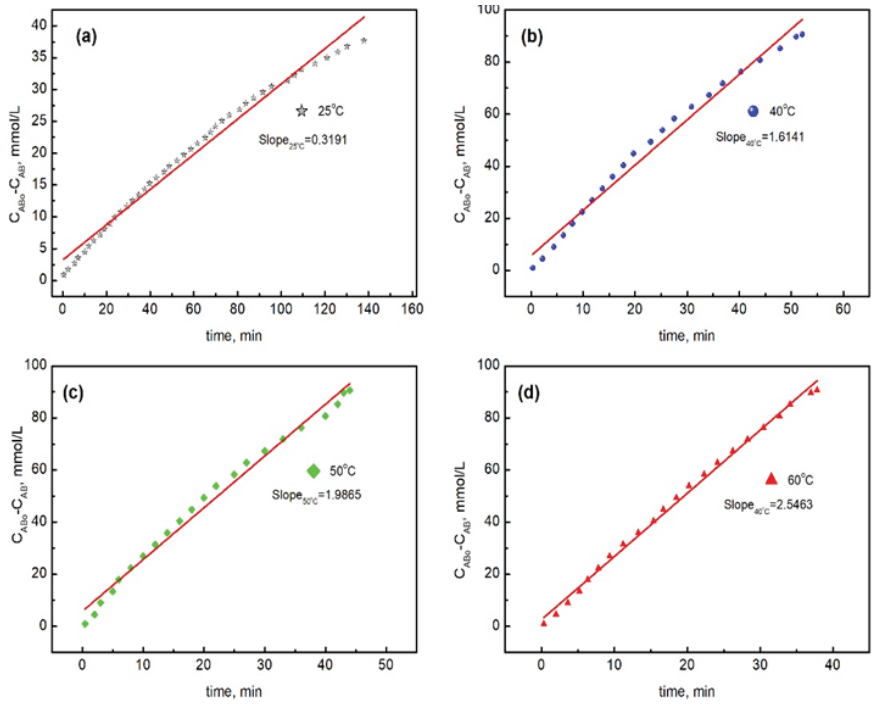

Figure 5. The initial and final ammonia borane concentration differences versus time over NiO@N-rGO at different temperatures.

ons. The as-prepaid NiO@N-rGO exhibits high catalytic performance to the dissociation and hydrolysis of AB at moderate temperature, which is accompanied by a release of up to 3 equivalent H_2 in 40 mins, which could be ascribed to the synergetic effect between NiO NPs and N-rGO. These non-precious metal-free based catalysts with the promoting effect through the nitrogen-doped rGO could open up to find their application not only as promising hydrogen storage materials for onboard systems but also in various other applications.

Acknowledgement

The author thanks Prof. Dr. Hüseyin Çelikkan for his helpful comments.

References

[1] Xu, Q., & Chandra, M. (2006). Catalytic activities of non-noble metals for hydrogen generation from aqueous ammonia–borane at room temperature. *Journal of Power Sources, 163*(1), 364-370.

[2] Barış, M., Şimşek, T., Taşkaya, H., & Chattopadhyay, A. K. (2018). Synthesis of Fe-Fe2B catalysts via solvothermal route for hydrogen generation by hydrolysis of NaBH4. *Journal of Boron, 3*(1), 51-62.

[3] Çakanyıldırım, Ç., Özsaçmacı, G., & Metin, G. (2016). Co-Mn/TiO2 catalyst to enhance the NaBH4 decomposition. *Journal of Boron, 1*(1), 1-5.

[4] Zhang, H., Zhang, L., Rodríguez-Pérez, I. A., Miao, W., Chen, K., Wang, W., Li, Y., & Han, S. (2021). Carbon nanospheres supported bimetallic Pt-Co as an efficient catalyst for NaBH4 hydrolysis. *Applied Surface Science, 540*(1), 148296.

[5] Balbay, A., Selvitepe, N., & Saka, C. (2021). Fe doped-CoB catalysts with phosphoric acid-activated montmorillonite as support for efficient hydrogen production via NaBH4 hydrolysis. *International Journal of Hydrogen Energy, 46*(1), 425-438.

[6] Abdelhamid, H. N. (2020). Salts induced formation of hierarchical porous ZIF-8 and Their Applications for CO2 Sorption and hydrogen generation via NaBH4 hydrolysis. *Macromolecular Chemistry and Physics, 221*(7), 2000031.

[7] Amri, N. E., & Roger, K. (2020). Polyvinylpyrrolidone (PVP) impurities drastically impact the outcome of nanoparticle syntheses. *Journal of Colloid and Interface Science, 576*, 435-443.

[8] Karaca, T., Sevim, M., & Metin, Ö. (2017). Facile synthesis of monodisperse copper–platinum alloy nanoparticles and their superb catalysis in the hydrolytic dehydrogenation of ammonia borane and hydrazine borane. *ChemCatChem, 9*(22), 4185-4190.

[9] Xu, P., Lu, W., Zhang, J., & Zhang, L. (2020). Efficient hydrolysis of ammonia borane for hydrogen evolution catalyzed by plasmonic Ag@ Pd Core–shell nanocubes. *ACS Sustainable Chemistry & Engineering, 8*(33), 12366-12377.

[10] Shore, S. G., & Parry, R. W. (1955). The crystalline compound ammonia-borane, 1 H3NBH3. *Journal of the American Chemical Society, 77*(22), 6084-6085.

[11] Faverio, C., Boselli, M. F., Medici, F., & Benaglia, M. (2020). Ammonia borane as a reducing agent in organic synthesis. *Organic & Biomolecular Chemistry, 18*, 7789-7813.

[12] Li, H., Yang, Q., Chen, X., & Shore, S. G. (2014). Ammonia borane, past as prolog. *Journal of Organometallic Chemistry, 751*, 60-66.

[13] Vijayalakshmi, K. P., & Suresh, C. H. (2017). Ammonia borane clusters: energetics of dihydrogen bonding, cooperativity, and the Role of Electrostatics. *The Journal of Physical Chemistry A, 121*(13), 2704-2714.

[14] Ren, X., Lv, H., Yang, S., Wang, Y., Li, J., Wei, R., ... Liu, B. (2019). Promoting effect of heterostructured NiO/Ni on Pt nanocatalysts toward catalytic hydrolysis of ammonia borane. *The Journal of Physical Chemistry Letters, 10*(23), 7374-7382.

[15] Zhou, L., Zhang, T., Tao, Z., & Chen, J. (2014). Ni nanoparticles supported on carbon as efficient catalysts for the hydrolysis of ammonia borane. *Nano Research, 7*(5), 774-781.

[16] Zhao, B., Liu, J., Zhou, L., Long, D., Feng, K., Sun, X., & Zhong, J. (2016). Probing the electronic structure of M-graphene oxide (M=Ni, Co, NiCo) catalysts for hydrolytic dehydrogenation of ammonia borane. *Applied Surface Science, 362*, 79-85.

[17] Zhang, J., Chen, C., Yan, W., Duan, F., Zhang, B., Gao, Z., & Qin, Y. (2016). Ni nanoparticles supported on CNTs with excellent activity produced by atomic layer deposition for hydrogen generation from the hydrolysis of ammonia borane. *Catalysis Science&Technology, 6*(7), 2112-2119.

[18] Mahyari, M., & Shaabani, A. (2014). Nickel nanoparticles immobilized on three-dimensional nitrogen-doped graphene as a superb catalyst for the generation of hydrogen from the hydrolysis of ammonia borane. *Journal of Materials Chemistry A, 2*(39), 16652-16659.

[19] Du, X., Liu, C., Du, C., Cai, P., Cheng, G., & Luo, W. (2017). Nitrogen-doped graphene hydrogel-supported NiPt-CeO x nanocomposites and their superior catalysis for hydrogen generation from hydrazine at room temperature. *Nano Research, 10*(8), 2856-2865.

[20] Lu, Y., Huang, Y., Zhang, M., & Chen, Y. (2014). Nitrogen-doped graphene materials for supercapacitor applications. *Journal of Nanoscience and Nanotechnology, 14*(2), 1134-1144.

[21] Hummers Jr., W. S., & Offeman, R. E. (1958). Preparation of graphitic oxide. *Journal of the American Chemical Society, 80*(6), 1339-1339.

[22] Tan, Y.Q., Song, Y.H., & Zheng, Q. (2013). Facile regulation of glutaraldehyde-modified graphene oxide for preparing free-standing papers and nanocomposite films. *Chinese Journal of Polymer Science, 31*(3), 399-406.

[23] Long, D., Li, W., Ling, L., Miyawaki, J., Mochida, I., & Yoon, S.H. (2010). Preparation of nitrogen-doped graphene sheets by a combined chemical and hydrothermal reduction of graphene oxide. *Langmuir, 26*(20), 16096-16102.

[24] Ariharan, A., Viswanathan, B., & Nandhakumar, V. (2017). Nitrogen doped graphene as potential material for hydrogen storage. *Graphene, 6*(2), 41-60.

[25] Yung, T.Y., Huang, L.Y., Chan, T.Y., Wang, K.S., Liu, T.Y., Chen, P.T., ... Liu, L.K. (2014). Synthesis and characterizations of Ni-NiO nanoparticles on PDDA-modified graphene for oxygen reduction reaction. *Nanoscale Research Letters, 9*(1), 444.

[26] Klug, H. P., & Alexander, L. E. (1974). *X-ray diffraction procedures: for polycrystalline and amorphous materials*. (2nd Edition). John Wiley&Sons. ISBN: 978-0-471-49369-3.

[27] Naveen, A. N., & Selladurai, S. (2015). Novel low temperature synthesis and electrochemical characterization of mesoporous nickel cobaltite-reduced graphene oxide (RGO) composite for supercapacitor application. *Electrochimica Acta, 173*, 290-301.

[28] Tao, H.C., Yang, X.L., Zhang, L.L., & Ni, S.-B. (2015). One-step synthesis of nickel sulfide/N-doped graphene composite as anode materials for lithium ion batteries. *Journal of Electroanalytical Chemistry, 739*, 36-42.

[29] Li, G., & Zhang, Y. (2019). Highly selective two-electron oxygen reduction to generate hydrogen peroxide using graphite felt modified with N-doped graphene in an electro-Fenton system. *New Journal of Chemistry, 43*(32), 12657-12667.

[30] Salavati-Niasari, M., & Entesari, M. (2012). Controlled synthesis of spherical α-Ni(OH)2 hierarchical nanostructures via a simple hydrothermal process and their conversion to NiO. *Polyhedron, 33*(1), 302-309.

[31] Chen, X. A., Chen, X., Zhang, F., Yang, Z., & Huang, S. (2013). One-pot hydrothermal synthesis of reduced graphene oxide/carbon nanotube/α-Ni(OH)2 composites for high performance electrochemical supercapacitor. *Journal of Power Sources, 243*, 555-561.

[32] Deng, D., Pan, X., Yu, L., Cui, Y., Jiang, Y., Qi, J., ... Xue, Q. (2011). Toward N-doped graphene via solvothermal synthesis. *Chemistry of Materials, 23*(5), 1188-1193.

[33] Liu, L., Chen, R., Liu, W., Wu, J., & Gao, D. (2016). Catalytic reduction of 4-nitrophenol over Ni-Pd nanodimers supported on nitrogen-doped reduced graphene oxide. *Journal of Hazardous Materials, 320*, 96-104.

[34] Su, F., Lv, X., & Miao, M. (2015). High-performance two-ply yarn supercapacitors based on carbon nanotube yarns dotted with Co3O4 and NiO nanoparticles. *Small, 11*(7), 854-861.

[35] McIntyre, N., & Cook, M. (1975). X-ray photoelectron studies on some oxides and hydroxides of cobalt, nickel, and copper. *Analytical Chemistry, 47*(13), 2208-2213.

[36] Zhou, Q., Yang, H., & Xu, C. (2016). Nanoporous Ru as highly efficient catalyst for hydrolysis of ammonia borane. *International Journal of Hydrogen Energy, 41*(30), 12714-12721.

[37] Xi, P., Chen, F., Xie, G., Ma, C., Liu, H., Shao, C., ... Zeng, Z. (2012). Surfactant free RGO/Pd nanocomposites as highly active heterogeneous catalysts for the hydrolytic dehydrogenation of ammonia borane for chemical hydrogen storage. *Nanoscale, 4*(18), 5597-5601.

[38] Amali, A. J., Aranishi, K., Uchida, T., & Xu, Q. (2013). PdPt nanocubes: a high-performance catalyst for hydrolytic dehydrogenation of ammonia borane. *Particle*

& Particle Systems Characterization, 30(10), 888-892.

[39] Cao, C. Y., Chen, C. Q., Li, W., Song, W. G., & Cai, W. (2010). Nanoporous nickel spheres as highly active catalyst for hydrogen generation from ammonia borane. *ChemSusChem, 3*(11), 1241-1244.

[40] Metin, Ö., Mazumder, V., Özkar, S., & Sun, S. (2010). Monodisperse nickel nanoparticles and their catalysis in hydrolytic dehydrogenation of ammonia borane. *Journal of the American Chemical Society, 132*(5), 1468-1469.

[41] Kalidindi, S. B., Indirani, M., & Jagirdar, B. R. (2008). First row transition metal ion-assisted ammonia−borane hydrolysis for hydrogen generation. *Inorganic Chemistry, 47*(16), 7424-7429.

[42] Umegaki, T., Yan, J.M., Zhang, X.B., Shioyama, H., Kuriyama, N., & Xu, Q. (2009). Preparation and catalysis of poly(N-vinyl-2-pyrrolidone) (PVP) stabilized nickel catalyst for hydrolytic dehydrogenation of ammonia borane. *International Journal of Hydrogen Energy, 34*(9), 3816-3822.

[43] Du, X., Yang, C., Zeng, X., Wu, T., Zhou, Y., Cai, P. ... Luo, W. (2017). Amorphous NiP supported on rGO for superior hydrogen generation from hydrolysis of ammonia borane. *International Journal of Hydrogen Energy, 42*(20), 14181-14187.

[44] Manna, J., Akbayrak, S., & Özkar, S. (2017). Nickel(0) nanoparticles supported on bare or coated cobalt ferrite as highly active, magnetically isolable and reusable catalyst for hydrolytic dehydrogenation of ammonia borane. *Journal of Colloid and Interface Science, 508*, 359-368.

[45] Yang, X. J., Li, L. L., Sang, W. L., Zhao, J. L., Wang, X. X., Yu, C. ... Tang, C. C. (2017). Boron nitride supported Ni nanoparticles as catalysts for hydrogen generation from hydrolysis of ammonia borane. *Journal of Alloys and Compounds, 693*, 642-649.

[46] Lin, Y., Yang, L., Jiang, H., Zhang, Y., Cao, D., Wu, C. ... Song, L. (2019). Boosted reactivity of ammonia borane dehydrogenation over Ni/Ni2P heterostructure. *The Journal of Physical Chemistry Letters, 10*(5), 1048-1054.

[47] Liu, Y., Zhang, J., Liu, Q., & Li, X. (2020). TiN nanotube supported Ni catalyst Ni@ TiN-NTs: experimental evidence of structure–activity relations in catalytically hydrolyzing ammonia borane for hydrogen evolution. *RSC Advances, 10*(61), 37209-37217.

[48] Ghosh, S., Kadam, S. R., Houben, L., Bar-Ziv, R., & Bar-Sadan, M. (2020). Nickel phosphide catalysts for hydrogen generation through water reduction, ammonia-borane and borohydride hydrolysis. *Applied Materials Today, 20*, 100693.

[49] Feng, K., Zhong, J., Zhao, B., Zhang, H., Xu, L., Sun, X., & Lee, S. T. (2016). CuxCo1−xO Nanoparticles on graphene oxide as a synergistic catalyst for high-efficiency hydrolysis of ammonia–borane. *Angewandte Chemie, 128*(39), 12129-12133.

BOR DERGİSİ
JOURNAL OF BORON
https://dergipark.org.tr/boron

Bazı ester kompleks sentezlerinde kullanılacak borik asit, monoetilen glikol ve gliserol moleküllerinin kuramsal ve deneysel olarak incelenmesi

Cihat Hilal[1*], Müşerref Önal[2]

[1]Ankara Üniversitesi, Fen Fakültesi, Kimya Bölümü, Ankara, 06100, Türkiye, ORCID orcid.org/0000-0002-6966-6711
[2]Ankara Üniversitesi, Fen Fakültesi, Kimya Bölümü, Ankara, 06100, Türkiye, ORCID orcid.org/0000-0002-1540-8389

MAKALE BİLGİSİ

Makale Geçmişi:
İlk gönderi 10 Mart 2021
Kabul 10 Mayıs 2021
Online 30 Haziran 2021

Araştırma Makalesi

DOI: 10.30728/boron.894787

Anahtar kelimeler:
Borik asit
Gliserol
Hesaplamalı kimya
Kompleks ester
Monoetilen glikol

ÖZET

Bor kompleksleri üzerine kondenzasyon tepkimeleriyle yapılan deneysel çalışmalar incelendiğinde; borik asitle (H_3BO_3) genellikle polivinil alkolün veya mannitolün kullanıldığı görülmektedir. Yaygın literatür kullanımının aksine bu çalışmada monoetilen glikol ($C_2H_6O_2$) ve gliserol ($C_3H_8O_3$) molekülleri çalışılmıştır. Moleküllerin teorik olarak incelenmesi sonucu elde edilen verilerden yararlanılarak bor kompleksi sentezi için en ideal molekülün seçilmesi, ayrıca teorik sonuçlara deneysel katkı sağlaması amacıyla borik asit ve diğer iki molekül arasında 1:1 mol oranı göz önüne alınarak deneysel bir çalışmanın yürütülmesi amaçlanmıştır. Teorik çalışmalarda Spartan 14 ve Gaussian 03W paket programları kullanılmıştır. Metot olarak B3LYP karma yoğunluk fonksiyonu kuramı ve 6-31+G** dağınık çift polarize olmuş split valans baz seti tercih edilmiştir. İncelenen moleküllere ilişkin toplam molekül enerjisi (E_T), E_{HOMO}, E_{LUMO}, elektron ilgisi (A), iyonlaşma enerjisi (I), sertlik (η), yumuşaklık (σ), elektronegativite (χ), kimyasal potansiyel (CP) ve elektrofilisite (ω) gibi bazı yapı tanımlayıcıları hesaplanmıştır. Yapılan teorik çalışmalardan elde edilen sonuçlara göre, kompleks ester oluşum reaksiyonunda gliserol molekülünün monoetilen glikol molekülünden, yapısında daha fazla hidroksil grubu (üç hidroksil grubu) içermesi, enerji boşluğunun (8,51) daha düşük olması, daha yumuşak (0,23502) ve daha elektronegatif (2,775) molekül olması nedenleriyle kompleks ester oluşumunda daha etkin olacağı öngörülmüştür. Deneysel çalışmalar ise 1 atm basınç, 100°C sıcaklık ve spiralli geri soğutucu altında yürütülmüştür. Yapı aydınlatmaları amaçlanmadığından ürünler üzerinde karakterizasyon çalışmaları yapılmamış, çözeltilerin zamana bağlı pH değişimleri izlenerek kaydedilmiştir. Elde edilen pH değerleri incelendiğinde borik asit-gliserol karışımının daha asidik bir çözelti oluşturduğu sonucuna varılmıştır.

Theoretical and experimental investigation of boric acid, monoethylene glycol and glycerol molecules to be used in some ester complex synthesis

ARTICLE INFO

Article history:
Received March 10, 2021
Accepted May 10, 2021
Available online June 30, 2021

Research Article

DOI: 10.30728/boron.894787

Keywords:
Boric acid
Glycerol
Computational chemistry
Complex ester
Monoethylene glycol

ABSTRACT

When looking at the experimental research on boron complex condensation reactions, it appears that polyvinyl alcohol or mannitol is often used with boric acid (H_3BO_3). Contrary to the common literature use, monoethylene glycol ($C_2H_6O_2$) and glycerol ($C_3H_8O_3$) molecules were studied in this study. It is intended to choose the ideal molecule to synthesis the boron complex using the data obtained from the theoretical analysis of molecules, In addition, it was aimed to conduct an experimental study considering the 1:1 molar ratio between boric acid and the other two molecules in order to make an experimental contribution to the theoretical results. Spartan 14 and Gaussian 03W package programs were used in theoretical studies. As methods, the B3LYP mixed density function theory and the 6-31+G ** diffuse bipolar split valence base set were chosen. Investigation on the molecules, some structure descriptors such as total molecular energy (E_T), E_{HOMO}, E_{LUMO}, electron affinity (A), ionization energy (I), hardness (η), softness (σ), electronegativity (χ), chemical potential (CP) and electrophilicity (ω) have been calculated. According to the results obtained from the theoretical studies,in the complex ester formation reaction, the glycerol molecule contains more hydroxyl groups (three hydroxyl groups), the energy gap (8.51) is lower, the softer (0.23502) molecule and it is more electronegative (2.775) in its structure than the monoethylene glycol molecule, was predicted to be more effective. Experiments were carried out at a pressure of 1 atm, at a temperature of 100°C, and with a Graham condenser. Since the products were not intended for use in a structure, no characterization tests were conducted on them, but pH changes over time were observed and reported. The obtained pH values revealed that the boric acid-glycerol solution was more acidic.

*Corresponding author: chilal@ankara.edu.tr

1. Giriş (Introduction)

Bor ve türevlerine ilişkin literatürde çok sayıda bilimsel çalışma bulunmaktadır. Bor atomları azot atomları ile koordine kovalent bağlar, oksijen atomları ile ise kovalent bağlar oluşturmaktadır. Bu durum bor atomlarının farklı kompleks bileşikler oluşturmasına yol açmaktadır. Borik asit çok hidroksilli organik bileşiklerin (poliollerin) sulu çözeltileri ile karıştırıldığında kondenzasyon tepkimeleri ile değişik kompleks esterler oluşmaktadır [1-4]. Poliollerden bazıları glikol, gliserol, poli(vinil) alkol, sorbitol, mannitol ve ksilitol olarak sıralanabilir. Günümüzde bor bileşiklerinin/komplekslerinin kullanım alanları çok geniştir. Bor komplekslerinin bazılarının asitliği borik asidin zayıf asitliğinden daha yüksektir. Bu nedenle, borik asit yerine borik asidin poliollerle ile yaptığı kompleksin sulu çözeltisi kuvvetli bir baz olan sodyum hidroksidin sulu çözeltisi ile titre edilerek borik asit miktarı belirlenir [5]. Tuzlu sular, sulu çözeltiler, atık sular ve ters ozmoz membranlarında yer alan bor bileşikleri ester oluşturularak uzaklaştırılmaktadır [6-14]. Diğer taraftan, bu türden bileşikler makrosiklik kimyada [15,16], supramoleküler kimyada [17], floresanslı materyallerde [18], optik materyallerde [19,20], radyasyona karşı önleyici olarak nükleer reaktörlerin kontrolünde [21], bor ve nötron yakalama terapisinde ve tıpta biyoaktif materyallerde [22], tarım, biyokimya, ilaç sanayii ve malzeme bilimi gibi çok çeşitli alanlarda [23,24] kullanılmaktadır. Bor komplekslerinin 400°C civarında ısıtılmasıyla elde edilen önceller 1000-1400°C sıcaklık aralığında ve argon atmosferinde piroliz edilerek bor karbür tozları elde edilebilmektedir [25-28]. Elmas ve kübik bor nitrürden sonra en sert malzeme olarak bilinen bor karbürde savunma sanayi ve nükleer santraller başta olmak üzere diğer bor bileşikleri gibi endüstride birçok alanda kullanılmaktadır.

Yukarıda sunulan detaylı literatür göz önüne alındığında bor karbür üretiminde öncel, atık sulardan bor uzaklaştırmak için bileşik ve borik asitin asitliğini artırarak kuvvetli bazlarla titrasyona imkan sağlayacak bileşik elde etmek için daha çok mannitol ve polivinil alkolün tercih edildiği görülmektedir. Bor kompleksleri sentezinde mannitol veya polivinil alkol yanı sıra diğer bazı hidroksilli bileşiklerin kullanılmasının araştırılarak en uygun olanının belirlenmesi amaçlanmıştır. Bunun için, daha küçük moleküllü ve daha az sayıda hidroksil grubuna sahip monoetilen glikol ve gliserol ile borik asit arasındaki mümkün esterleşme tepkimeleri hesaplamalı kimya yöntemleri ile belirlenecektir. Spartan ve Gaussian gibi programlarla yürütülen hesaplamalı kimya yöntemleriyle kimyasal moleküllerinin yapı incelemeleri [29], yapısal özelliklerin aydınlatılması [30] ve moleküler modelleme çalışmaları yapılmaktadır [31]. Bor-poliol kompleks sentezi için kullanılan bileşiklerden en ideal molekülün belirlenmesine yönelik olan bu çalışmada; Spartan ve Gaussian programları kullanılarak hesaplamalı kimya yöntemleriyle borik asitin molekül yapısı teorik olarak incelenecek ve bazı literatür değerleriyle karşılaştırılıp seçilen hesaplamalı kimya yönteminin geçerliliği test edilecektir. Tepkimeye giren bileşenlerin yapılarından yola çıkılarak oluşacak esterinlerin mümkün teorik yapıları belirlenerek, molekül enerjileri hesaplanacaktır. Deneysel çalışmada ise borik asit-monoetilen glikol, borik asit-gliserol çözeltilerinin pH değişimleri izlenecektir.

1.1. Borik Asit, Monoetilen Glikol ve Gliserol Moleküllerinin Bazı Özellikleri ve Kompleks Oluşum Mekanizmaları (Some Properties and Complex Formation Mechanisms of Boric Acid, Monoethylene Glycol and Glycerol Molecules)

Kimyasal bileşiminin %56,3 B_2O_3 ve %43,7 H_2O molekülü olan borik asit; boranik asit (H_3BO_3), ortoborik asit ve hidrojen borat olarak da isimlendirilmektedir. Parlak ve beyaz kristalleri suda çözünebilen bir asittir [32]. Boraks, kernit, tinkal, üleksit ve kolamanit gibi bor minerallerinin sülfürik asitle reaksiyonunundan elde edilmektedir [33]. Borik asit sulu çözeltilerde (pH=5,1) diol, triol veya poliol gibi hidroksil gruplarına sahip moleküllerle kondenzasyon reaksiyonları verir [4,34-38]. Sulu çözeltilerde elektron ilgisi yüksek ve Bronsted asidi [39] olarak davranan borik asit; elektron eksikliği bulunması nedeniyle suyun iyonlaşması ile oluşan OH^- iyonunu yapısına alır ve Eş. 1'deki reaksiyon üzerinden borat anyonunu oluşturur. Bu sırada, borat anyonu ve hidroksilli moleküller arasında kondenzasyon reaksiyonu ile kompleks ester molekülleri oluşur [40,41]. Kompleks oluşumunda farklı stokiyometrik oranlarda gerçekleşebilecek muhtemel reaksiyonlar Eş. 2, Eş. 3, Eş. 4 ve Eş. 5'deki gibi sembolize edilebilir. "L" simgesi hidroksilli molekülleri ifade etmektedir.

$$B(OH)_3 + 2H_2O \leftrightarrow H_3O^+ + [B(OH)_4]^- \quad (1)$$

(1:1 mol oranı) $$B(OH)_4^- + H_2L \leftrightarrow [B(OH)_2L]^- + 2H_2O \quad (2)$$

(1:2 mol oranı) $$B(OH)_4^- + 2H_2L \leftrightarrow [BL_2]^- + 4H_2O \quad (3)$$

(2:1 mol oranı) $$2B(OH)_4^- + H_4L \leftrightarrow [B_2(OH)_4L]^{2-} + 4H_2O \quad (4)$$

(2:2 mol oranı) $$2B(OH)_4^- + 2H_2L \leftrightarrow [B_2(OH)_4L]^{2-} + 4H_2O \quad (5)$$

1,2 etandiol olarak da bilinen monoetilen glikol (MEG) renksiz, kokusuz, tatlı ve su ile her oranda karışabilen bir sıvıdır. Dietilen glikol (DEG) ve trietilen glikol (TEG) gibi diğer türevleri içinde en küçük molekül yapısına sahip glikoldür. Polietilen tereftalat (PET) gibi polimerlerin öncüsü olarak yaygın kullanıma sahip olan MEG; antifrizin bileşenlerinden biridir [42]. Gliserol (1,2,3-propantriol) ise oda sıcaklığında viskoz, saydam, suda çözünen ve polar bir sıvıdır [43]. Biyogaz ve polimer üretimi gibi birçok alanda kullanılmaktadır [44]. Borik asit, monoetilen glikol ve gliserol moleküllerinin yapıları Şekil 1' de verilmiştir.

1.2. Hesaplamalı Kimya, Moleküler Geometri ve Bazı Yapı Tanımlayıcıları (Computational Chemistry, Molecular Geometry and Some Structure Descriptors)

Hesaplamalı kimya yöntemleri aracılığıyla matematiksel veriler kullanılarak teorik ve deneysel veriler arasında bağlantı kurulmaya çalışılır [47-53]. Moleküllerin

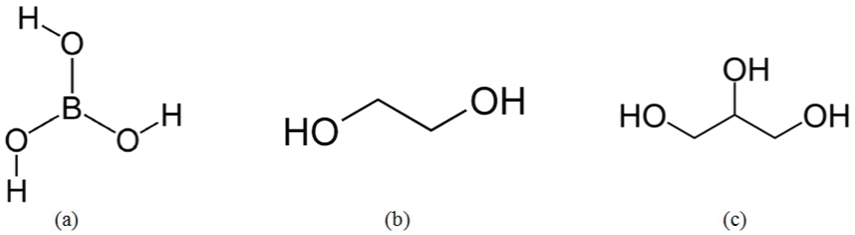

Şekil 1. Borik asit (a) [45], monoetilen glikol (b) ve gliserol (c) [46] moleküllerinin molekül yapısı (Molecular structure of boric acid (a), monoethylene glycol (b) and glycerol (c) molecules).

fiziksel ve kimyasal özelliklerinin geometrileri ile ilişkili olduğu bilinmektedir. Teorik çalışmalarla elde edilen optimize yapılar ve optimize yapılara ait elektronik yapı tanımlayıcıları moleküllerin kimyasal aktivitesi hakkında bilgi edinilmesini sağlar. Teorik olarak elde edilebilecek olan bazı yapı tanımlayıcılarına; molekülün toplam enerjisi (E_T), homo enerjisi (E_{HOMO}), lumo enerjisi (E_{LUMO}), enerji boşluğu (ΔE), elektron ilgisi (A), iyonlaşma enerjisi (I), elektrofilisite indeksi (ω), elektroaktiflik (χ), sertlik (η) ve yumuşaklık (σ), kimyasal potansiyel (CP), dipol moment (μ) ve polarizibilite örnek olarak verilebilir [54-56].

2. Malzemeler ve Yöntemler (Materials and Methods)

Hesaplamalı kimya çalışmalarında kuantum mekaniksel yöntemlerden olan Ab-initio yöntemleri tercih edilmiştir. Ab-initio yönteminde ise molekül içi elektron-elektron etkileşimlerinin göz önüne alındığı yoğunluk fonksiyonu teorisi kullanılmıştır. Ayrıca sistemlerin enerjilerinin hesaplanmasında yoğunluk fonksiyonel teorisi (YFT) ve Hartree-Fock (HF) teorilerini birlikte kapsayan Becke tipi 3 parametreli Lee-Yang-Parr (B3LYP) [57] karma yoğunluk fonksiyonu kuramı tercih edilmiştir. Temel set olarak ise daha çok uyarılmış durum ve anyonlar için tercih edilen ağır atomlara d, hidrojene p ve ayrıca her iki atom çeşidine birden dağınık fonksiyonların ilave edildiği 6-31+G** dağınık çift polarize olmuş split valans baz seti kullanılmıştır. Tercih edilen yöntem kullanılarak tüm teorik hesaplamalar marka/model bilgisi HP/ Pro 3400 Series MT olan bilgisayara kurulumları yapılan Gaussian 03W [58] ve Spartan 14 paket programları aracılığıyla, 298,15 K sıcaklık, 1 atm basınç ve vakum ortamı şartları seçilerek iki bölümde gerçekleştirilmiştir.

Deneysel çalışmalar ise atmosfer basıncı altında 100°C sıcaklıkta üç boyunlu cam balonda ve spiralli geri soğutucu altında gerçekleştirilmiştir. Borik asit (H_3BO_3: Merck, Cas-No 10043-35-3), monoetilen glikol ($C_2H_6O_2$: Merck, Cas-No 107-21-1) ve gliserolün ($C_3H_8O_3$: Merck, Cas-No 56-81-5) 2.5 M stok çözeltileri ultra saf su (New Human Power I) ile 80°C sıcaklıkta hazırlanmıştır. Stok çözeltiler hazırlanırken sıvı halde bulunan monoetilen glikolün (1,11 g/mol) ve gliserolün (1,26 g/mol) yoğunlukları göz önüne alınmıştır. Sıcaklığı 100°C' de bulunan borik asit çözeltisine 1/1 mol oranına göre hazırlanan monoetilen glikol çözeltisi damla damla ilave edilmiş ve karışım yarım saat süreyle manyetik karıştırıcılı ısıtıcıda (Heidolph MR Hei-Tec) sabit sıcaklıkta karıştırılmıştır. Sonrasında elde edilen çözelti yarım saat süreyle 250 rpm' de çalkalanmıştır (GFL-3017 Shaker). Isıtma işlemine son verildiği andan itibaren 15. dk, 30. dk, 45. dk, 60. dk ve 120. dakikalarda çözeltinin pH ölçümleri (Adwa AD12) yapılmış ve not edilmiştir. Aynı işlemler gliserol içinde tekrar edilmiştir.

Yapılan bu çalışmada; öncelikle borik asit molekülüne ilişkin teorik çalışmalar yürütülmüş, elde edilen bazı sonuçlar literatür verileriyle kıyaslanarak yöntemin güvenilirliği sınanmıştır. Aynı çalışmalar monoetilen glikol ve gliserol molekülleri için yapılmış ve toplam enerjileri, optimize geometri yapıları, homo ve lumo enerjileri, enerji boşlukları, elektrostatik yüzey haritaları, elektron ilgileri, iyonlaşma enerjileri, yumuşaklık, sertlik, elektronegativite, elektrofilisite ve kimyasal potansiyelleri hesaplanmış ve Tablo 2'de verilmiştir. Ulaşılan verilerden yola çıkılarak bor komplekslerinin sentezlenebilmesi için kullanılan moleküllerden hangi molekülün daha uygun olacağı tartışılmıştır. Eş. 2, Eş. 3 ve Eş. 5 göz önüne alınarak borik asit ve diğer iki molekül arasında oluşabilecek olası esterlere ilişkin optimize molekül yapıları belirlenerek üç boyutlu yapıları çizilmiştir.

3. Sonuçlar ve Tartışma (Results and Discussion)

3.1. Borik Asit İçin Elde Edilen Teorik Veriler ve Bazı Literatür Verileriyle Kıyaslanması (Comparison of Theoretical Data with Some Literature Data Obtained for Boric Acid)

Borik asit molekülü üzerine yapılan teorik çalışma sonucu elde edilen verilerin bazıları bulunabilen literatür verileriyle karşılaştırılmıştır. Tablo 1'de teorik veriler sütununda verilen yapılarda sarı renk bor atomunu, kırmızı renk oksijen atomunu ve beyaz renk ise hidrojen atomunu temsil etmektedir. Sunulan veriler incelendiğinde hesaplanan toplam molekül enerjisi başta olmak üzere; molekülün optimize yapısının, oksijen-bor, oksijen-hidrojen bağ uzunluklarının, oksijen-bor-hidrojen bağ açılarının ve molekülün lumo yapılarının literatür verileriyle uyuştuğu belirlenmiştir. Bu tespitlerle seçilen teorik yöntem literatür verileriyle doğrulanmış ve diğer moleküller üzerinde hesaplamalı çalışmalara geçilmiştir.

Tablo 1. Borik asit molekülünün bazı teorik ve literatür verileri (Some theoretical and literature data of the boric acid molecule)

	Hesaplanan Teorik Veriler	Literatür verileri
E_T, Toplam Molekül Enerjisi*(au)*	-252,49	-249,8094[a] -252,5602[b]
ZPE, Sıfır Noktası Enerjisi*(kJ/mol)*	129,25	133,52[a]
S, Entropi*(J/mol.K)*	270,35	268,99[a]
V, Hacim*(A^3)*	55,39	55,76[a]
A, Alan*(A^2)*	78,56	79,37[a]
Polarizasyon	43,46	41,25[a]
C_v, Sabit hacimdeki özgül ısı*(J/mol)*	56,59	61,26[a]
Optimize molekül yapısı	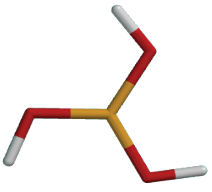	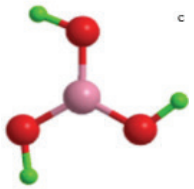
Bağ uzunlukları ve bağ açıları*(Å)*	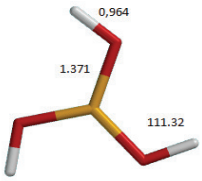	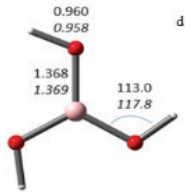
Lumo yapıları	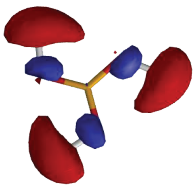	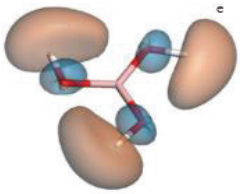

[a]: [59], [b]: [60], [c]: [61], [d]: [62], [e]: [63]

3.2. Gliserol İçin Elde Edilen Teorik Veriler (Theoretical Data Obtained for Glycerol)

Moleküllerin yük yoğunlukları, dipol momentleri, reaktiflikleri, bazı makroskopik özellikleri ve moleküller arası etkileşim yerleri elektrostatik potansiyel haritaları hesaplanarak öngörülebilir. Farklı renklenmelerin görüldüğü bu haritalarda kırmızı renk negatif (elektrofilik), mavi renk pozitif (nükleofilik), yeşil renk ise sıfır potansiyelli bölgeleri temsil eder. Kırmızı renkten mavi renge doğru gidilirken elektron yoğunluğu da azalır. Şekil 2(b), Şekil 3(b) ve Şekil 4(b) incelendiğinde üzerinde çalışılan tüm moleküller için elektron yoğunluklarının oksijen atomları üzerinde kümelendiği görülmektedir. Tespit edilen bu bölgelerin moleküllerin kimyasal aktifliklerinde önemli bir rol oynayacağı bilinmektedir. Bu doğrultuda; Şekil 3(b) ve Şekil 4(b) ayrıntılı incelendiğinde üç hidroksil grubuna sahip gliserolün monoetilen

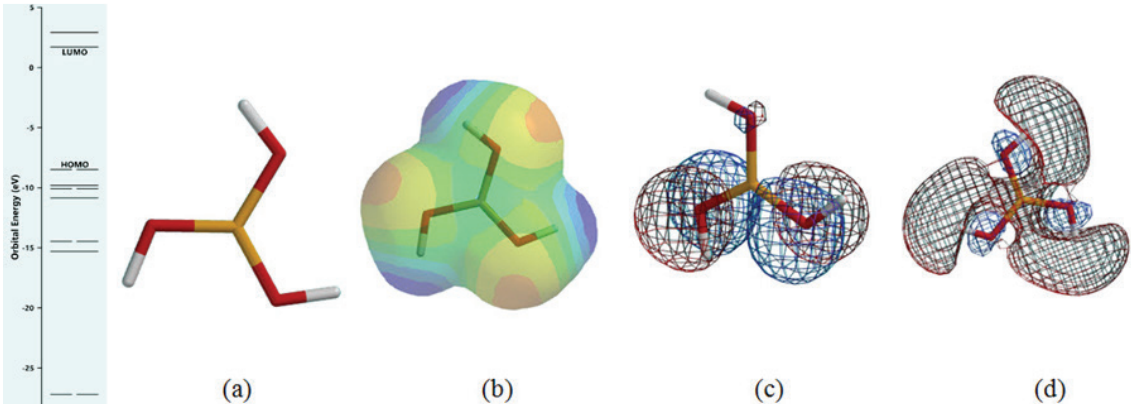

Şekil 2. Borik asit molekülünün hesaplanan optimize molekül yapısı (a), transparent elektrostatik yüzey haritası (b), mesh homo (c) ve mesh lumo (d) çizimleri (IsoVal 0.002) (Computed optimized molecular structure of boric acid molecule (a), transparent electrostatic surface map (b), mesh homo (c) and mesh lumo (d) plots (IsoVal 0.002)).

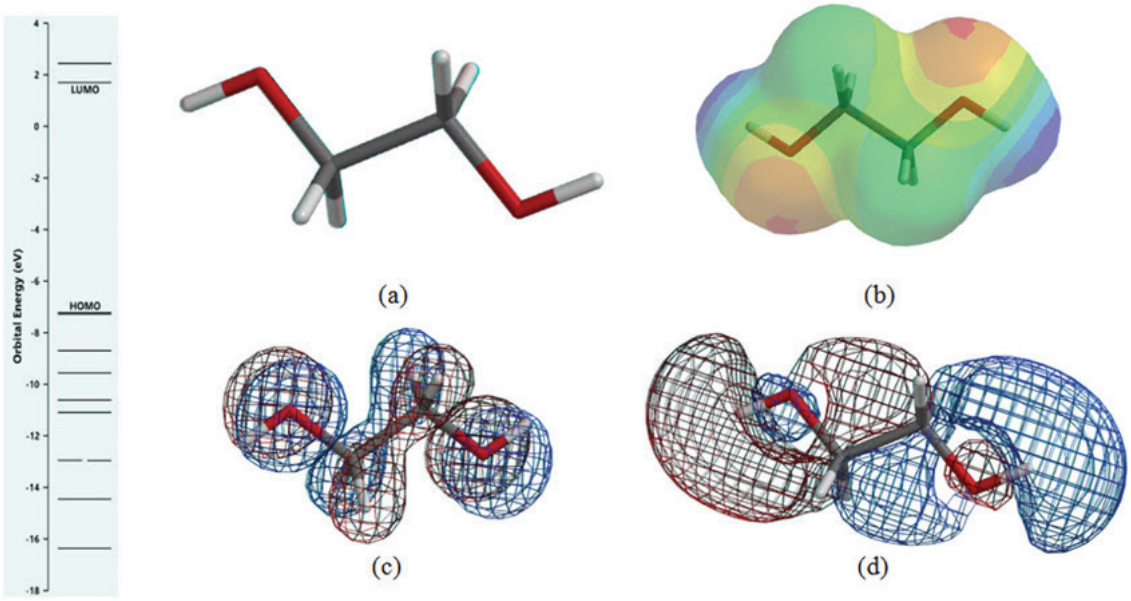

Şekil 3. Mono etilen glikol molekülünün hesaplanan optimize molekül yapısı (a), transparent elektrostatik yüzey haritası (b), mesh homo (c) ve mesh lumo (d) çizimleri (IsoVal 0.002) (Calculated optimized molecular structure of mono ethylene glycol molecule (a), transparent electrostatic surface map (b), mesh homo (c) and mesh lumo (d) plots (IsoVal 0.002)).

glikole göre daha elektrofilik olduğu değerlendirilmektedir.

Elektron vericisi olarak davranan "E_{HOMO}" elektronlarla dolu en dış orbitali ifade ederken, elektron alıcısı olarak davranan "E_{LUMO}" elektronlarla dolu olmayan en iç orbitali ifade eder. Molekülün E_{HOMO} değeri yüksekse bu molekül düşük enerjili boş moleküler orbitali bulunan moleküle kolayca elektron transfer edebilir. Düşük E_{LUMO} değeri ise yüksek enerjili dolu moleküler orbitale sahip olan molekülden kolayca elektron alabilir. Tablo 2'de yer alan E_{HOMO} ve E_{LUMO} değerleri göz önüne alındığında gliserolün monoetilen glikol molekülüne göre daha aktif olduğu sonucuna ulaşılabilir.

E_{HOMO} ve E_{LUMO} arasındaki enerji boşluğu (ΔE) moleküllerin kimyasal kararlılığa işaret eder. Yani enerji boşluğu yüksek olan molekül daha kararlıdır, daha az aktiftir. ΔE enerji farkı küçüldükçe etkileşim artacak, reaksiyon daha kolay olacaktır [64]. Eğer, ΔE büyük ise sert moleküller, küçük ise yumuşak moleküller olarak adlandırılır. Moleküllerin aktiflikleri sertlik değerinin azalmasıyla veya yumuşaklık değerinin artmasıyla artar. Tablo 2'de yer alan ΔE değerleri incelendiğinde monoetilen glikol gliserol molekülüne göre daha sert bir moleküldür. Başka bir deyişle, gliserol daha yumuşak karakterli bir moleküldür. Aynı tablodan, moleküllere ait sertlik (η) ve yumuşaklık (σ) değerlerinin de bu öngörüyü doğruladığı görülmektedir.

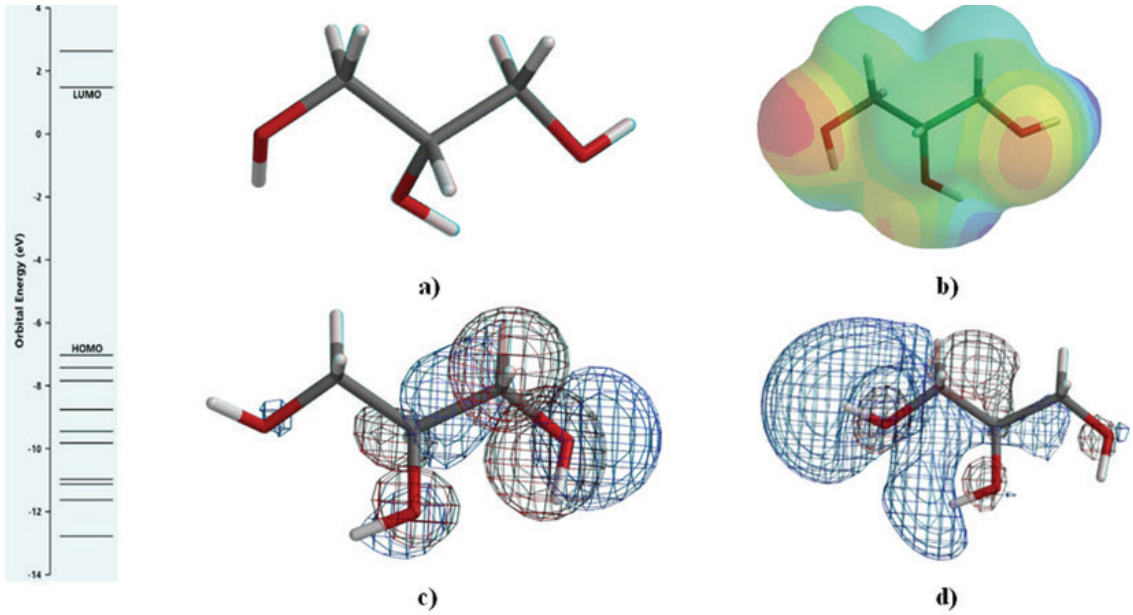

Şekil 4. Gliserol molekülünün hesaplanan transparent optimize molekül yapısı (a), elektrostatik yüzey haritası (b), mesh homo (c) ve mesh lumo (d) çizimleri (IsoVal 0.002) (Calculated transparent optimized molecular structure (a), electrostatic surface map (b), mesh homo (c) and mesh lumo (d) plots of the glycerol molecule (IsoVal 0.002)).

Tablo 2. Borik asit, monoetilen glikol ve gliserol moleküllerine ait hesaplanan bazı yapı tanımlayıcıları(Some calculated structure descriptors of boric acid, monoethylene glycol and glycerol molecules).

	Borik Asit	MEG	Gliserol
E_T, Toplam Molekül Enerjisi *(au)*	-252,49	-230,25	-344,79
E HOMO *(ev)*	-8,49	-7,22	-7,03
E LUMO *(ev)*	1,71	1,69	1,48
ΔE *(ev)*	10,2	8,91	8,51
ZPE, Sıfır Noktası Enerjisi *(kJ/mol)*	129,25	222,77	312,68
H, Entalpi *(kJ/mol)*	143,21	238,83	332,79
S, Entropi *(J/mol.K)*	270,35	291,99	334,29
G, Serbest Enerji *(kJ/mol)*	62,605	151,773	233,121
A, Elektron ilgisi *(ev)*	-1,71	-1,69	-1,48
I, İyonlaşma enerjisi *(ev)*	8,49	7,22	7,03
η, Sertlik *(ev)*	5,1	4,455	4,255
σ, Yumuşaklık *(ev^{-1})*	0,19608	0,22447	0,23502
χ, Elektronegativite *(ev)*	3,39	2,765	2,775
CP, Kimyasal Potansiyel *(ev)*	-3,39	-2,765	-2,775
ω, Elektrofilisite *(ev)*	1,12668	0,85805	0,90489

Moleküllerin elektronegativite (χ) değerinin azalmasıyla, kimyasal potansiyel (CP) değerinin ise artmasıyla aktiflikleri artar. Tablo 2 incelendiğinde monoetilen glikolün gliserole göre daha aktif bir molekül olduğu bilgisi edinilebilir. Ancak, monoetilen glikol ve gliserolün elektronegativite ve kimyasal potansiyel değerlerinin birbirlerine çok yakın olduğu görülmektedir. Yukarıda belirtilen ve Tablo 2'de yer alan sonuçların tamamı birlikte değerlendirildiğinde; gliserolün monoetilen glikole göre daha reaktif bir molekül olduğu söylenebilir.

3.3. Borik Asit-Monoetilen Glikol Kompleksleri Üzerine Yapılan Teorik Hesaplamalar (Theoretical Calculations on Boric Acid-Monoethylene Glycol Complexes)

Şekil 5 ve Şekil 6'da molekül yapılarının üstlerinde bulunan sayılar borik asit/hidroksil grubuna sahip moleküllerin stokiyometrik oranlarını, altlarında bulunan sayılar molekül numaralarını, parantez içerisinde bulunan sayılar ise bağ atomlarını ifade etmektedir. Moleküler yapılardaki sarı renkli atomlar "bor" atomlarını, kırmızı renkli atomlar "oksijen" atomlarını, gri renkli atomlar "karbon" atomlarını, beyaz renkli atomlar ise "hidrojen" atomlarını simgelemektedir.

Borik asit ve monoetilen glikol molekülleri arasında Eş. 1, Eş. 2 ve Eş. 4'e göre farklı stokiyometrik oranlarda muhtemel kompleksleşme reaksiyonları sonucu elde edilebilecek ürünlerin molekül yapıları Şekil 5'de, bu yapılara ait toplam enerji değerleri ise Tablo 3'de sunulmuştur.

Şekil 5 ve Tablo 3 birlikte değerlendirildiğinde borik asit ve monoetilen glikol arasında farklı stokiyometrik oranlarda üç farklı kompleks yapının oluşabileceği değerlendirilebilir. Matematiksel olarak en küçük enerji değerine sahip yapı en stabil yapıdır [65,66]. Bu yapılardan en düşük enerjili (toplam molekül enerjisi = -813,3788) ve dolayısıyla en stabil/kararlı olması sebebiyle 2:2 mol oranında teorik olarak "1(1,1/2,2)" şeklinde ifade edilen yapının sentezlenme ihtimalinin diğerlerine nazaran daha yüksek olduğu sonucuna varılabilir. Molekül yapıları göz önüne alındığında atom sayısı arttıkça matematiksel ifadeyle moleküllerin toplam enerjilerinin azaldığı tespit edilmiştir. Uygun analiz

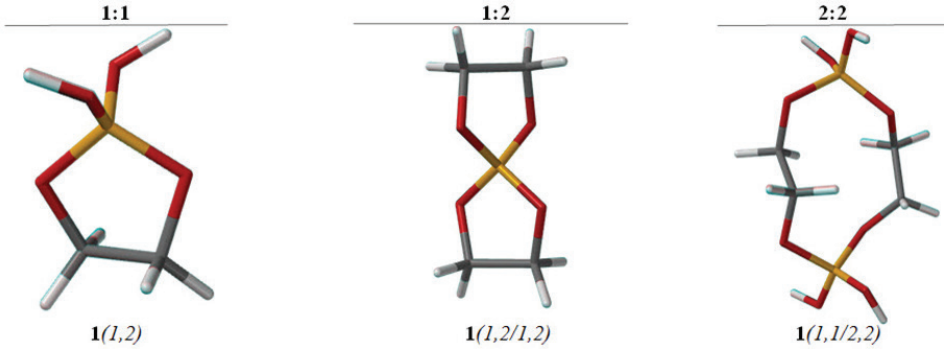

Şekil 5. Borik asit-monoetilen glikol komplekslerinin optimize molekül yapıları (Optimized molecular structures of boric acid-monoethylene glycol complexes).

Tablo 3. Borik asit-monoetilen glikol komplekslerinin hesaplanan toplam enerji değerleri (Calculated total energy values of boric acid-monoethylene glycol complexes).

Borik Asit-monoetilen glikol					
Borik asit/MEG oranı*(mol)*	**Numara**	**Bağ atomları**	**Anyon yükü**	**Toplam molekül enerjisi *(hartree/au)***	**Enerji ortalaması *(hartree/au)***
1:1	1	1,2	1	-405,5953	-405,5953
1:2	1	1,2/1,2	1	-483,0527	-483,0527
2:2	1	1,1/2,2	2	-813,3788	-813,3788

koşullarında gerçekleştirilecek deneysel çalışmalarda sentezlenecek ürün, tespit edilen üç farklı yapının karışımını da içerebilir. Bu aşamada hangi molekül yapısının elde edildiğinin tespiti için ürün üzerinde detaylı enstrümantal analiz metotları uygulanması gerekecektir. Çalışmamızın amacı dışında kaldığından bu husus bu çalışmada irdelenmemiştir.

3.4. Borik Asit-Gliserol Kompleksleri Üzerine Yapılan Teorik Hesaplamalar (Theoretical Calculations on Boric Acid-Glycerol Complexes)

Borik asit ve gliserol molekülleri arasında farklı stokiyometrik oranlarda kompleksleşme reaksiyonları sonucu elde edilebilecek muhtemel ürünlerin molekül yapıları Şekil 6'da, bu yapılara ait toplam enerji değerleri ise Tablo 4'de sunulmuştur.

Şekil 6 ve Tablo 4 birlikte değerlendirildiğinde borik asit ve gliserol molekülleri arasında farklı stokiyometrik oranlarda toplam sekiz farklı kompleks yapının oluşabileceği değerlendirilebilir. Bu yapılardan matematiksel olarak en küçük enerji değerine sahip olması (toplam molekül enerjisi = -1042,4638) ve dolayısıyla en kararlı yapı olması sebebiyle 2:2 mol oranında üç numaralı, teorik olarak "3(1,2/3,3)" şeklinde ifade edilen yapının sentezlenme ihtimalinin diğerlerine nazaran daha yüksek olduğu sonucuna ulaşılmıştır.

3.5. Ürünler Üzerine Elde Edilen Deneysel Veriler (Experimental Data on Products)

Saf haldeki borik asidin sulu çözeltesinin pH değeri 5,1'dir. Şekil 7'den pH değerinin iki çözeltide de düştüğü, 120. dk sonunda iki çözelti arasında yaklaşık 1 birim pH farkı olduğu görünmektedir. Sonuç olarak; borik asit+monoetilen glikol çözeltisine göre, borik asit+gliserol çözeltisinin pH değerinin daha düşük dolayısıyla asitliğinin daha yüksek olduğu tespit edilmiştir. Buna göre, zayıf borik asitin titrasyonu için monoetilen glikol yerine gliserolün kullanımının daha elverişli olacağı sonucuna varılmıştır. Diğer taraftan, bu veriler kompleks oluşumu için teorik olarak gliserolün önerilmesini destekler niteliktedir.

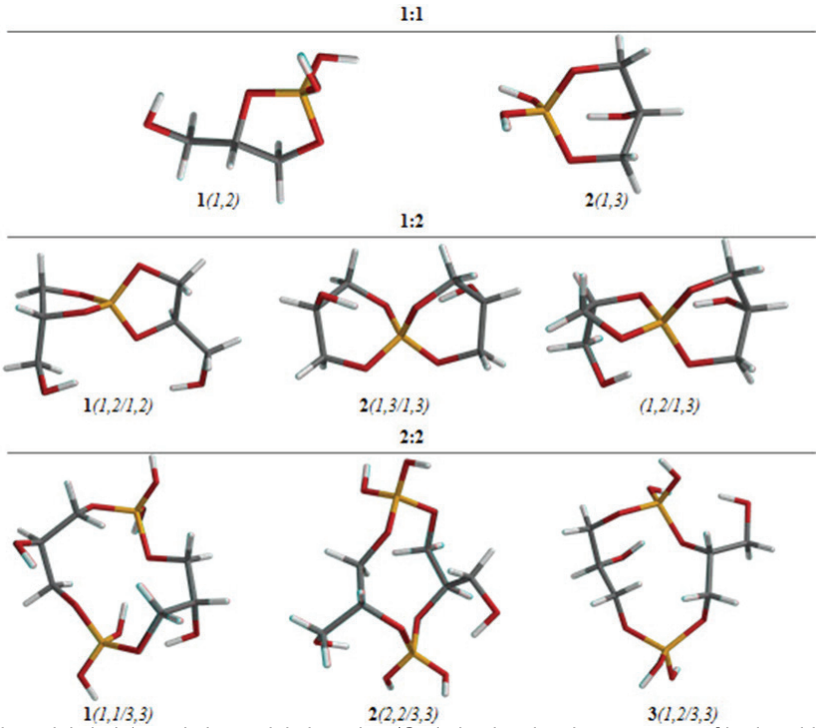

Şekil 6. Borik asit-gliserol komplekslerinin optimize molekül yapıları (Optimized molecular structures of boric acid-glycerol complexes).

Tablo 4. Borik asit-gliserol komplekslerinin hesaplanan toplam enerji değerleri (Calculated total energy values of boric acid-glycerol complexes).

Borik Asit-Gliserol					
Borik asit/Gliserol oranı *(mol)*	**Numara**	**Bağ atomları**	**Anyon yükü**	**Toplam molekül enerjisi** *(hartree/au)*	**Enerji Ortalaması** *(hartree/au)*
1:1	1	1,2	1	-520,1405	-520,1411
	2	1,3	1	-520,1417	
1:2	1	1,2/1,2	1	-712,1311	-712,1108
	2	1,3/1,3	1	-712,0951	
	3	1,2/1,3	1	-712,1061	
2:2	1	1,1/3,3	2	-1040,6762	-1041,7666
	2	2,2/3,3	2	-1042,1597	
	3	1,2/3,3	2	-1042,4638	

4. Sonuçlar (Conclusions)

Çalışmanın ilk basamağında borik aside ilişkin bazı teorik veriler elde edilmiştir. Tablo 1'de görüldüğü gibi elde edilen bu teorik sonuçlardan bazıları literatür verileriyle kıyaslanmıştır. Ulaşılan değerler literatür verileriyle uyuştuğundan yöntemin güvenilirliği sağlanmıştır. Aynı yöntemle incelenen borik asit, monoetilen glikol ve gliserol moleküllerine ilişkin sonuçlar Şekil 2, Şekil 3, Şekil 4'de verilmiştir. Bu moleküllerin kimyasal aktivitelerine ilişkin bazı yapı tanımlayıcıları Koopmans teoremi [67] ile hesaplanarak Tablo 2'de verilmiştir. Farklı mol oranlarında borik asit ve polioller arasındaki kondenzasyon tepkimeleri ile oluşan kompleks esterlere ilişkin optimize edilen molekül geometrileri ve bu geometrilere ilişkin hesaplanan toplam enerjiler sırayla Şekil 5, Şekil 6, Tablo 3 ve Tablo 4'de verilmiştir. Monoetilen glikol ve gliserolün molekül yapısında yeteri kadar hidroksil grubu bulunmadığından verilen şekil ve tablolarda Eş. 4'e göre (2 mol borik asit: 1 mol poliol) ürün tahmini yapılmamıştır.

Elde edilen teorik ve deneysel veriler bir arada değerlendirildiğinde; borik asit ile bor kompleksi sentezlenmesi amacıyla yapılacak çalışmalarda gliserolün monoetilen glikole göre daha elverişli olacağı değerlendirilmektedir. Ancak sıcaklık, basınç, değişken kütlesel bileşimler gibi farklı etkenlerin değiştirilmesiyle alternatif ve daha verimli sentez koşulları geliştirilebilir. Bu doğrultuda elde edilecek komplekslerin uygun enstrümantal analiz yöntemlerle (NMR, SEM, XRD, FTIR vb.) karakterizasyonu ürünler üzerine şüphesiz daha sağlıklı yorumlar yapılmasını sağlayacaktır

References

1. Springsteen, G., & Wang, B. (2002). A detailed examination of boronic acid–diol complexation. *Tetrahedron, 58*(26), 5291-5300.
2. Shvarts, E., Ignash, R., & Belousova, R. (2005). Reactions of polyols with boric acid and sodium monoborate. *Russian Journal of General Chemistry, 75*(11), 1687-1692.
3. Fujita, N., Shinkai, S., & James, T. D. (2008). Boronic acids in molecular self-assembly. *Chemistry-An Asian Journal, 3*(7), 1076-1091.
4. Peters, J.A. (2012). Interactions between boric acid derivatives and saccharides in aqueous media: Structures and stabilities of resulting esters. *Coordination Chemistry Reviews, 268*, 1-22.
5. Azevedo, M. C. C., & Cavaleiro, A. M. (2012). The

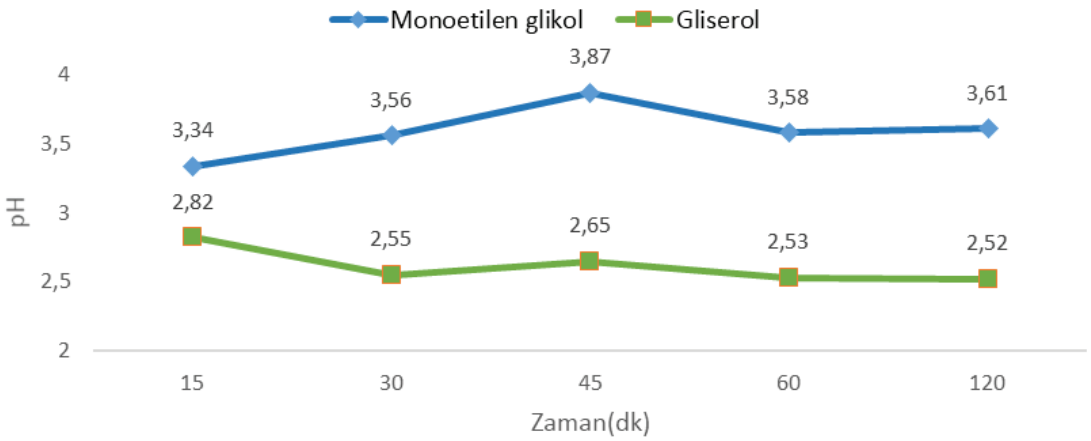

Şekil 7. Borik asit + monoetilen glikol ve borik asit + gliserol çözeltilerinin zamana bağlı pH değerleri (Time-dependent pH values of boric acid + monoethylene glycol and boric acid + glycerol solutions).

acid–base titration of a very weak acid: boric acid. *Journal of Chemical Education, 89*(6), 767-770.

6. Hilal, N., Kim, G., & Somerfield, C. (2011). Boron removal from saline water: A comprehensive review. *Desalination, 273*(1), 23-35.
7. Dydo, P. (2013). The influence of d-mannitol on the effectiveness of boric acid transport during electrodialytic desalination of aqueous solutions. *Journal of Membrane Science, 429*, 130-138.
8. Dydo, P., Turek, M., & Milewski, A. (2014). Removal of boric acid, monoborate and boron complexes with polyols by reverse osmosis membranes. *Desalination, 334*(1), 39-45.
9. Bai, C., Guo, M., Liu, Z., Wu, Z., & Li, Q. (2018), A novel method for removal of boron from aqueous solution using sodium dodecyl benzene sulfonate and d-mannitol as the collector. *Desalination, 431*, 47-55.
10. Geffen, N., Semiat, R., Eisen, M. S., Balazc, Y., Katz, I., & Dosoretz, C. G. (2006). Boron removal from water by complexation to polyol compounds. *Journal of Membrane Science, 286*(1-2), 45-51.
11. Dydo, P., Nems, I., & Turek, M. (2012). Boron removal and its concentration by reverse osmosis in the presence of polyol compounds. *Separation and Purification Technology, 89*, 171-180.
12. Zhou, R., Dı, L., Wang, C., Fang, Y., Wu, J., & Xu, Z. (2014). Surface functionalization of microporous polypropylene membrane with polyols for removal of boron acid from aqueous solution. *Chinese Journal of Chemical Engineering, 22*(1), 11-18.
13. Du, X., Meng, J., Xu, R., Shi, Q., & Zhang, Y. (2015). Polyol-grafted polysulfone membranes for boron removal: Effects of the ligand structure. *Journal of Membrane Science, 476*, 205-215.
14. Wang, Z., Wu, Z., Zhang, Z., & Meng, J. (2017). Hyperbranched-polyol-tethered poly (amic acid) electrospun nanofiber membrane with ultrahigh adsorption capacity for boron removal. *Applied Surface Science, 402*, 21-30.
15. Christinat, N., Scopelliti, R., & Severin, K. (2004). A new method for the synthesis of boronate macrocycles. *Chemical Communications, 10*, 1158-1159.
16. Barba, V., Höpfl, H., Farfan, N., Santillan, R., Beltran, H. I., & Zamudio, L.S. (2004). Boron–nitrogen macrocycles: A new generation of calix [3] arenes. *Chemical Communications, 24*, 2834-2835.
17. D'Souza, F., Smith, P. M., Zangler, M. E., McCarty, A. L., Itou, M., Araki, Y., & Ito, O. (2004). Energy transfer followed by electron transfer in a supramolecular triad composed of boron dipyrrin, zinc porphyrin, and fullerene: A model for the photosynthetic antenna-reaction center complex. *Journal of the American Chemical Society, 126*(25), 7898-7907.
18. Liu, Z. Q., Fang, Q., Cao, D. X., Wang, D., & Xu, G. B. (2004). Triaryl boron-based A-π-A vs triaryl nitrogen-based D-π-D quadrupolar compounds for single-and two-photon excited fluorescence. *Organic Letters, 6*(17), 2933-2936.
19. Reyes, H., Munoz, B., Farfan, N., Santillan, R., Lima, S. R., Lacroix, P. G., & Nakatani, K. (2002). Synthesis, crystal structures, and quadratic nonlinear optical properties in a series of push–pull boronate derivatives. *Journal of Materials Chemistry, 12*(10), 2898-2903.
20. Entwistle, C. D., & Marder, T. B. (2002). Boron chemistry lights the way: Optical properties of molecular and polymeric systems. *Angewandte Chemie International Edition, 41*(16), 2927-2931.
21. Rivera, J.M., Rincon, S., Farfan, N., & Santillan, R. (2011). Synthesis, characterization and X-ray studies of new chiral five-six-membered ring, [4.3.0] heterobicyclic system of monomeric boronates. *Journal of Organometallic Chemistry, 696*(11-12), 2420-2428.
22. Hawthorne, M. F., & Lee, M. W. (2003). A critical assessment of boron target compounds for boron neutron capture therapy. *Journal of Neuro-Oncology, 62*(1), 33-45.
23. Yumatov, V. D., Il'inchik, E. A., & Volkov, V. V. (2003). X-Ray spectra and electronic structure of boron compounds. *Russian Chemical Reviews, 72*(12), 1011-1034.
24. Marco-Dufort, B., & Tibbitt, M. (2019). Design of moldable hydrogels for biomedical applications using dynamic covalent boronic esters. *Materials Today Chemistry, 12*, 16-33.
25. Suri, A. K., Subramanian, C., Sonber, J. K., & Murthy, C. (2010). Synthesis and consolidation of boron carbide: A review. *International Materials Reviews, 55*(1), 4.
26. Pekdemir, A. D. (2018). *Preparation and characterization of boron carbide at low-temperature from boric acid and polyols* [Ph. D. Thesis, Ankara University]. Council of Higher Education Thesis Center (Thesis Number 507934).
27. Gao, S., Li, X., Wang, S., Xing, P., Kong, J., & Yang, G. (2019). A low cost, low energy, environmentally friendly process for producing high-purity boron carbide. *Ceramics International, 45*(3), 3101-3110.
28. Sivkov, A., Rakhmatullin, I., Shanenkov, I., & Shanenkova, Y. (2019). Boron carbide B4C ceramics with enhanced physico-mechanical properties sintered from multimodal powder of plasma dynamic synthesis. *International Journal of Refractory Metals and Hard Materials, 78*, 85-91.
29. Öztürk, F., & Aycan, T. (2021). Çinko (II)–sulfatiyazol-dietilentriamin kompleksinin hesaplamalı kimya yöntemi ile spektroskopik özelliklerinin incelenmesi: Moleküler modelleme çalışması. [Investigation of spectroscopic properties of Zinc (II)- sulfathiazole-diethylenetriamine complex by computational chemistry method: molecular modeling study]. *Afyon Kocatepe University Journal of Science and Engineering, 21*(1), 65-83.
30. Kızak, H. (2021). *Investigation of structural and spectroscopic properties of newly synthesized disazo dyes materials by theoretical calculatons* [M. Sc. Thesis, Pamukkale University]. Graduate School of Natural and Applied Sciences (Thesis Number 1006).
31. Direm, A., El Bali, B., Sayın, K., Abdelbaky, M. S. M., & Granda, S. G. (2021). Experimental and in silico studies of dichloro-tetrakis (1H-pyrazole)-cobalt (II): Structural description, photoluminescent behavior and molecular docking. *Journal of Molecular Structure*, *1235*,130266.
32. Elbeyli, İ. Y. (2000). *Evaluation of solid wastes that are formed during the borax and boric acid production in*

cement industry [M. Sc. Thesis, Yıldız Technical University]. Council of Higher Education Thesis Center (Thesis Number 95086).

33. Uyar, T., & Aksoy, S. (2008). *Genel Kimya İlkeler ve Modern Uygulamalar.* [General Chemistry Principles and Modern Applications] (Volume 2).

34. Bai, C., Wu, Z., Ye, X., Liu, H., Liu, Z., Zhang, H., Liu, Q & et al. (2019). Influence of the pH in reactions of boric acid/borax with simple hydroxyl compounds: investigation by raman spectroscopy and DFT calculations. *ChemistrySelect, 4*(48), 14132-14139.

35. Wolska, J., & Bryjak, M. (2013). Methods for boron removal from aqueous solutions-A review. *Desalination, 310*, 18-24.

36. Pappin, B., Kiefel M. J., & Houston T.A. (2012). *Boroncarbohydrate interactions, Carbohydrates-comprehensive studies on glycobiology and glycotechnology.* Chang C. F. (Ed.) IntechOpen. ISBN: 978-953-51-4264-5.

37. Ståhlberg, T., Rodriguez, S., Fristrup, P., & Riisager, A. (2011). Metal-free dehydration of glucose to 5-(hydroxymethyl) furfural in ionic liquids with boric acid as a promoter. *Chemistry - A European Journal, 17*(5), 1456-1464.

38. Hansen, T. S., Mielby, J., & Riisager, A. (2011). Synergy of boric acid and added salts in the catalytic dehydration of hexoses to 5-hydroxymethylfurfural in water. *Green Chemistry, 13*(1), 109-114.

39. Tunalı, N. K., & Özkar, S. (2011). *Anorganik Kimya*. [*Inorganic Chemistry*] (9th Ed.). Gazi Bookstore. ISBN-10 6053445347

40. Schmidt, M.P., Siciliano, S.D., & Peak, D. (2021). The role of monodentate tetrahedral borate complexes in boric acid binding to a soil organic matter analogue. *Chemosphere, 276*, 130150.

41. Xu, X., Fei, J., Xu, Y., Li, G., Dong, W., Xue, H., & Li, J. (2021). Boric acid-fueled ATP synthesis by FoF1 ATP synthase reconstituted in a supramolecular architecture. *Angewandte Chemie, 133*(14), 7695-7698.

42. Van Hal, J. W., Ledford, J. S., & Zhang, X. (2007). Investigation of three types of catalysts for the hydration of ethylene oxide (EO) to monoethylene glycol (MEG). *Catalysis Today, 123*(1-4), 310-315.

43. Pagliaro, M., & Rossi M. (2008). *The future of glycerol*. (2nd Edition). RSC Publishing. ISBN 978-1-84973-046-4.

44. Yalçınsoy, Ö. (2020), *Hydrogen-rich gas production by the catalytic thermochemical conversion of glycerol* [M. Sc. Thesis, Eskişehir Technical University]. Graduate School of Natural and Applied Sciences (Thesis Number 697693).

45. Pizzorno, L. (2015). Nothing boring about boron. *Integrative Medicine: A Clinician's Journal, 14*(4), 35.

46. Pagliaro, M., Criminna, R., Kimura, H., Rossi, M., & Pina, C. D. (2007). From glycerol to value-added products. *Angewandte Chemie International Edition, 46*(24), 4434-4440.

47. Sayın, K. (2014). *The investigation of structural and molecular properties of some platin(II) oxime complexes with computational chemistry methods* [M. Sc. Thesis, Sivas Cumhuriyet University]. Council of Higher Education Thesis Center (Thesis Number 363971).

48. Sayın, K. (2017). *Investigations of structures and electronic properties of some boron complexes with computational chemistry methods* [Ph. D. Thesis, Sivas Cumhuriyet Uniersity]. Council of Higher Education Thesis Center (Thesis Number 465242).

49. Ayşakar, E. (2019). *Investigation of cranberry, turmeric and strawberry fruits with calculative chemistry method* [M. Sc. Thesis, Sakarya University]. Council of Higher Education Thesis Center (Thesis Number 611714).

50. Örnek, M. (2019). *Illimunation of the crystal structures including tetrazole, thiazole, triazine and cyclobutyl by experimental and computational chemistry methods* [M. Sc. Thesis, Çankırı Karatekin University]. Council of Higher Education Thesis Center (Thesis Number 553918).

51. Tutar, N. N. (2019). *Investigation of corrosion inhibition efficiencies Of 6,7-Dihydroxy- 4-Methyl-8-(Arylazo) coumarin derivatives by computational chemistry methods* [M. Sc. Thesis, Sivas Cumhuriyet University]. Council of Higher Education Thesis Center (Thesis Number 580673).

52. Zaim, Z. (2019). *Investigation of [Tp(CO)2Mo≡C-Ph)]2+ and [L(CO)2Mo≡C-Ph)]+ alkylidyne complexes with computational chemistry* [M. Sc. Thesis, Sivas Cumhuriyet University] Council of Higher Education Thesis Center (Thesis Number 547732).

53. Ölüç, İ.B. (2020). *Antioxidant activity of the hazelnut plant determination by computational chemistry methods* [M. Sc. Thesis, Üsküdar University] Council of Higher Education Thesis Center (Thesis Number 625461).

54. Erdem, S.S. (2006). *Hesapsal Organik Kimya Ders Notları* [Computational Organic Chemistry Lecture Notes, PDF]. Retrieved from https://www.google.com/url?sa=t&rct=j&q=&esrc=s&source=web&cd=&ved=2ahUKEwjfsL2s6eTwAhWOgf0HHcXiDzMQFjABegQIAxAD&url=https%3A%2F%2Fmimoza.marmara.edu.tr%2F~erdem%2Fpdf%2FHesapsal_Organik_Kimya.pdf&usg=AOvVaw0CO9uupWQbGJL9PAQBGUum.

55. Sayın, K., & Karakaş, D. (2017). Theoretical study on the antitumor properties of Ru (II) complexes containing 2-pyridyl, 2-pyridine-4-carboxylic acid ligands. *Journal of Molecular Structure, 1149*, 473-486.

56. Sayın, K., Karakaş, D., Kariper, S. E., & Sayın T. A. (2018). Computational study of some fluoroquinolones: Structural, spectral and docking investigations. *Journal of Molecular Structure, 1156*, 172-181.

57. Becke, A. D., Density-functional thermochemistry. II. The effect of the Perdew-Wang generalized-gradient correlation correction. *The Journal of Chemical Physics, 97*(12), 9173-9177.

58. Frisch, M., Trucks, G., Schlegel, H., Scuseria, G. E., Robb, M. A., Cheeseman, J. R., ... & Pople, A. J. (2004). Gaussian 03, revision C. 02.

59. Heydari, Z. (2018). The study of dissolution boric acid in different temperatures: A DFT study. International *Journal of New Chemistry, 5*(4), 140-147.

60. Tian, S. X., Xu K. Z., Huang M. B., Chen X. J., Yang J. L., & Jia C. C. (1999). Theoretical study on infrared vibrational spectra of boric-acid in gas-phase using density functional methods. *Journal of Molecular Structure: THEOCHEM, 469*(1-3), 223-227.

61. Zhou, Y., Fang C., Fang Y., & Zhu F. (2011). Polybo-

rates in aqueous borate solution: A Raman and DFT theory investigation. *Spectrochimica Acta Part A: Molecular and Biomolecular Spectroscopy, 83*(1), 82-87.

62. Pichierri, F. (2017). Molecular triskelions: structure and bonding in the perhalogenated analogues of boric acid, X3BO3 (X=F, Cl, Br, I). *Structural Chemistry, 28*(1), 213-223.

63. Da Silva, M.B., dos Santos R. C. R., Cunha A. M., Valentini A., Pessoa O. D. L., Caetano E. W. S., & Freire V. N. (2016). Structural, electronic, and optical properties of bulk boric acid 2A and 3T polymorphs: experiment and density functional theory calculations. *Crystal Growth&Design,16*(11), 6631-6640.

64. Günay, N., Pir, H., & Atalay, Y. (2011). L-asparaginyum pikrat molekülünün spektroskopik özelliklerinin teorik olarak incelenmesi. [Theoretical investigation of spectroscopic properties of L-asparaginium picrate molecule]. *Sakarya University Journal of Science, 1*, 15-32.

65. Türker, L., & Varış, S. (2014). A possible complex between TNT and epinephrine-A DFT study. *Zeitschrift für anorganische und allgemeine Chemie, 640*(2), 334-338.

66. Türker, L., Variş, S., & Bayar, Ç.Ç. (2013). A theoretical study of JP-10 hydroperoxidation. *Fuel,104*, 128-132.

67. Koopmans, T. (1934). Über die zuordnung von wellenfunktionen und eigenwerten zu den einzelnen elektronen eines atoms [About the assignment of wave functions and eigenvalues to the individual electrons of an atom]. *Physica, 1*(1-6), 104-113.

BOR DERGİSİ
JOURNAL OF BORON
https://dergipark.org.tr/boron

Improvement on flame retarding performance: Preparation and characterization of water-based indoor paints with addition of boric acid

Berk Uslu[1,2], Ş. Melda Eskitoros-Togay[3,4], Nursel Dilsiz[5*]

[1]Gazi University, Engineering Faculty, Chemical Engineering Department, Ankara, 06570, Turkey
ORCID orcid.org/0000-0002-8117-9537
[2]Turkish Industrial Property Valuation, Engineering and Consultancy Services, Ankara, 06560, Turkey
[3]Gazi University, Engineering Faculty, Chemical Engineering Department, Ankara, 06570, Turkey
ORCID orcid.org/0000-0002-7473-8417
[4]Turkish Medicines and Medical Devices Agency, Ankara, 06520, Turkey
[5]Gazi University, Engineering Faculty, Chemical Engineering Department, Ankara, 06570, Turkey
ORCID orcid.org/0000-0002-6496-0487

ARTICLE INFO

Article history:
Received January 20, 2021
Accepted May 11, 2021
Available online June 30, 2021

Research Article

DOI: 10.30728/boron.865316

Keywords:
Boric acid
Fire protection
Flame retardancy
Limiting oxygen index
Water-based indoor paint

ABSTRACT

With the increasing population, a fire-protection of buildings has become necessary. Therefore, water-based indoor paints, which reduce the rate of the fire and offer the chance to intervene before the flames spread, have received attention; however, the performance and flame retardant property of these paints need to be improved. In this study, boric acid (H_3BO_3), which is the product of boron (B), was used as an additive for a flame retardant in the prepared water-based indoor paints. In order to investigate the effect of different weight ratios of H_3BO_3, the paints have been prepared with the addition of 5%, 10%, and 20% (w/w) of H_3BO_3. In addition, the synergistic effect of H_3BO_3 and melamine ($C_3H_6N_6$) on the flame retarding performance of the prepared paints was also investigated. The physicochemical properties, flammability characteristics and thermal properties were analyzed by Fourier transform infrared spectroscopy (FTIR), limiting oxygen index (LOI), and thermogravimetric analysis (TGA), respectively. The results demonstrated that the characteristic peaks of H_3BO_3 were observed in the prepared paints. When the flammability behavior of the paint samples were compared, the sample (P6) containing 20% (w/w) of H_3BO_3 showed the highest fire resistance property. Moreover, the results of the thermogravimetric analysis demonstrated that the prepared paints containing H_3BO_3 decomposes into B_2O_3 and water, which suppresses the fire. It can be concluded that the prepared paint (P6) can be used as a suitable alternative for the water-based indoor paints.

1. Introduction

With the developing technology and the increase in urbanization, the risk of a fire has been a growing threat. In order to diminish this possible serious risk, fire protection in construction materials has become crucial with the increasing requirements for safety regulations [1]. These regulations make the most urgent need to develop new materials that can provide flame retardancy at high temperatures in the construction industry.

Recent innovations on fire-protection of construction materials cost more in terms of labor, raw materials, and coating, etc. Therefore, in order to lower this burden, the current research has moved towards the development of new products with a sustainable design in construction [2]. The design of a fire-protection of the construction materials for buildings can be performed actively or passively. While the active strategy is composed of mechanical and electrical systems, the passive one refers to limit the spread of flames within the elements of the buildings such as columns, coating, etc. [3].

The paint and coating industry has been changing with technology. This industry is separated into three groups such as architectural coatings, industrial coatings, and maintenance coatings. The architectural coatings include all paints, varnishes, and lacquers [4]. During a fire, to extend the time of interfering with a building, indoor paints have taken attention among other elements [2].

Indoor paints are chemical materials that create protective and decorative thin layers at different surfaces with several application methods [5]. However, most of these paints, composed of halogen- or phosphor-

*Corresponding author: ndilsiz@gazi.edu.tr

based flame retardants in formulations, are inflammable, not ecologically friendly, and release toxic gases and smoke in case of fire [2]. Thus, considerable attention to phosphor-or halogen-free paints should be given to solve these disadvantages [6].

Turkey has the highest boron (B) reserves in the world with 73.4% of the total reserves [7,8]. Many countries that have taken it as a raw material from Turkey transform this raw material into remarkable refined boron products, and then, they sell it back into the global market with higher prices [9]. Therefore, there will always be an increasing need for boron demand [10], and in order to obtain higher economic benefits from these reserves, Turkey should sell refined boron products.

Current interest in flame retardants has focused on developing nontoxic and environmentally-friendly systems as well as preventing further spreading of fire [11]. It is well known that boron compounds like H_3BO_3 and borax are flame retardants and smoke suppressants [6]. During combustion, boron-based flame retardants generate a protective intermediate layer between a surface and a heat source. This impenetrable layer, named char, covers the surface and acts as an oxygen barrier preventing further fire propagation [12]. Moreover, boron compounds have low toxicity compared to toxic halogen-or phosphorus-based flame retardants and are also odorless and colorless [6]. However, there are fewer studies done on boron and its compounds. Xu et al. have found that the addition of 10% of H_3BO_3 as a flame retardant agent into their product increased the value of the limiting oxygen index (LOI) by 33.1% [13]. Uddin et al. have shown that the addition of H_3BO_3 into chitosan films enhanced the fire retarding property when compared to single chitosan films [14]. On the other hand, one of the flame retardants is melamine ($C_3H_6N_6$), which has low cost and is nontoxic during combustion [15].

The aim of this study is to improve the effect of H_3BO_3 on the flame retarding performance of water-based indoor paints. In order to compare its effect, $C_3H_6N_6$ and also calcium carbonate ($CaCO_3$) were utilized in the prepared paints. The physicochemical properties, flammability characteristics and thermal properties were investigated and characterized by Fourier transform infrared spectroscopy (FTIR), limiting oxygen index (LOI), and thermogravimetric analysis (TGA), respectively. The findings of this study contribute to the construction industry as a suitable option to halogen-based paints for the enhancement of the flame retardancy of the water-based indoor paints.

2. Materials and Methods

2.1. Materials

Water-based indoor paints (P1-P6) were prepared with the help of Ortaç Boya Ltd. Sti. (Ankara, Turkey) according to the standards of ISO and the Turkish Standard Institute (TSE). $CaCO_3$, used as filling material in the paint, was obtained from NİDAŞ A.Ş. (Niğde, Turkey) by 99.6% pure and at 3μ of the particle size. H_3BO_3 was kindly supplied from Eti Maden (Ankara, Turkey) as almost 99.9% pure. $C_3H_6N_6$ was purchased from OCI (Netherlands) by 99.8% pure.

2.2. Preparation of the Samples

Figure 1 represents the preparation procedure of the samples. Firstly, in order to prepare P1, 0.005 g of pH regulator, 0.04 g of hardness modifier, 0.015 g of thickener, 0.024 g of the other auxiliary chemicals, and 1.88 g of water were mixed thoroughly in the mixer at 25°C with a speed of 800 rpm for 6 min. Then, 1.18 g of TiO_2, which is used to provide the balance of the white color of the paints for the filling process, was added to the mixer with the addition of 0.1 g of the matting agent and 0.24 g of the stabilizer. After the speed of the mixer was reduced to 700 rpm, the inhibitors of mold/fungus and antifreezing agent were also added, and the solution was mixed for 8 min. In the last step, 1.33 g of the binder and 0.01 g of defoaming agent were added to the mixer whose speed was reduced to 600 rpm and the final mixture was mixed thoroughly for 6 min. This composition of the sample (P1) is the basic formulation, which the compositions and the speed of the mixer in each step were determined by Ortaç Boya Ltd. Sti. with respect to TSE and ISO standarts.

In order to prepare the other samples from P2 to P6, the same procedure was followed at 25°C. However, when the speed of the mixer was reduced to 700 rpm, $CaCO_3$, H_3BO_3 and $C_3H_6N_6$ were added to the mixer. This step was repeated for all the prepared samples at different percentages of H_3BO_3, 5%, 10%, 20%, respectively, and the mixture containing 10% H_3BO_3 and 10% $C_3H_6N_6$. In the last stage, 0.933 g of the binder and 0.01 g of the defoaming agent were again added to the mixer at 25°C with a speed of 600 rpm for 6 min. During the whole process, the temperature was kept constant at 25°C.

The basis of the compositions was determined according to the preliminary studies in Ortaç Boya Ltd. Sti. The value of the compositions of all the other chemicals except $CaCO_3$, H_3BO_3 and $C_3H_6N_6$ were kept constant for all the samples. However, in order to prepare from P2 to P6, the compositions of $CaCO_3$, H_3BO_3 and $C_3H_6N_6$ were changed according to the composition of H_3BO_3 used at different percentages of 5, 10 and 20% wt. In our preliminary stability tests performed at different temperatures (at room temperature and in the oven at 52±1°C), at above 20% wt. of H_3BO_3, the prepared paints showed more viscous nature and started to dry much fast. Therefore, the highest value of H_3BO_3 was chosen as 20% wt. Table 1 shows the

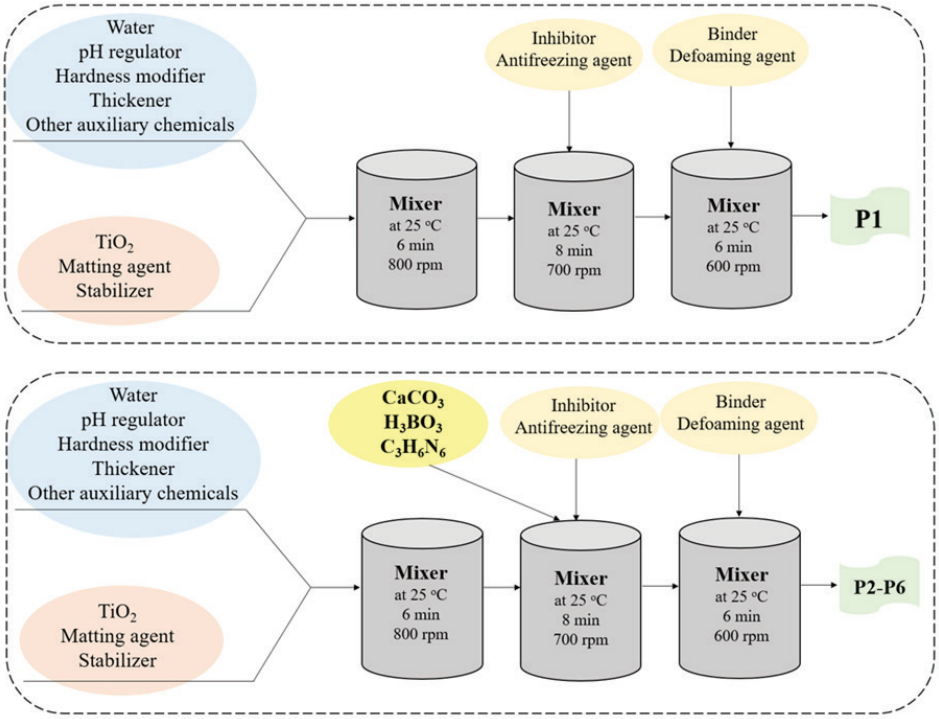

Figure 1. The preparation procedure of the samples.

compositions of each prepared sample, which gives 100% for each sample.

2.3. Characterization of the Samples

The mixing process of the paint and the additives were performed by Sozer/SM 1-130 machines (Sozer Makina, Kocaeli, Turkey), and then, the prepared paints were kept at KP-EY11 boxes for storage.

The chemical bonding of the samples was characterized by a Fourier-transform infrared spectroscopy (FTIR, Nicolet Avatar 370; Thermo Fisher Scientific, Inc., Waltham, MA, USA) in the range of 4000-400 cm^{-1} at room temperature.

Limiting oxygen index (LOI) measurements were performed using a Dynisco Polymer Test Limiting Oxygen Index Chamber (Dynisco Europe, Heilbronn, Germany) according to ASTM D 2863-19. In the test, each sample was dried and placed in templates of 10 cm x 1 cm x 0.4 cm according to TS EN ISO 4589-2 for three days at 35°C, and then gas flow was adjusted to confirm the standard test technique.

The thermal characterization of the samples was determined by thermogravimetric analysis (TGA, Perkin Elmer, Inc., Simultaneous Thermal Analyzer STA 6000, Waltham, MA, USA) in the temperature range of 25-800°C under nitrogen atmosphere at a heating rate of 10°C min^{-1}.

Table 1. The compositions of each prepared sample.

Composition (weight ratio %)	Sample Code					
	P1	P2	P3	P4	P5	P6
Water	38.5	17.6	17.6	17.6	17.6	17.6
TiO_2	23.6	15.7	15.7	15.7	15.7	15.7
Binder	26.6	19.0	19.0	19.0	19.0	19.0
Defoaming agent	0.2	0.2	0.2	0.2	0.2	0.2
Other auxiliary chemicals	11.1	11.1	11.1	11.1	11.1	11.1
$CaCO_3$	-	36.4	31.4	26.4	16.4	16.4
H_3BO_3	-	-	5.0	10.0	10.0	20.0
$C_3H_6N_6$	-	-	-	-	10.0	-

3. Results and Discussion

3.1. Characterization of the Samples

The chemical bonding of the prepared paints was characterized by FTIR from 4000 to 400 cm^{-1} in wavenumber in Figure 2. The FTIR spectra of pure paint (P1) without any additives or filling materials revealed that O-H stretching, C-H stretching vibrations, C=O stretching, C-H bending, C(=O)-O asymmetric stretching vibration was at about 3700 cm^{-1}, between 2900 and 2800 cm^{-1}, between 1800 and 1700 cm^{-1}, about 1400 cm^{-1}, between 1270 and 1200 cm^{-1}, respectively [16]. In case of P1, the stretching vibration peak at 3500-4000 cm^{-1}, which ascribed to OH bonds, likely owing to the absorption of moisture from the atmosphere, was more intense than the other paints. A broad and a sharp absorption bands owing to asymmetric stretching band of CO_3^{2-} between 1400-1500 cm^{-1} and at 877 cm^{-1}, respectively, were the specific peaks of $CaCO_3$ that was added in all the prepared samples [17]. The intensity of this peak was decreased with decreasing the addition amount of $CaCO_3$ in the prepared paints from P2 to P6. On the other hand, in the FTIR spectra of H_3BO_3, the broad band at 3200 cm^{-1} and the narrow band at 1190 cm^{-1} were referred to the absorption of B-OH; the band at about 1400 cm^{-1} was assigned to B-O vibration absorption [6,18]. In Figure 2, FTIR spectra of the samples containing only H_3BO_3 additive among with the sample without any additives or filling materials are shown. As seen in Figure 2, the intensity of characteristic H_3BO_3 peaks increased by increasing the amount of H_3BO_3 in the paints prepared.

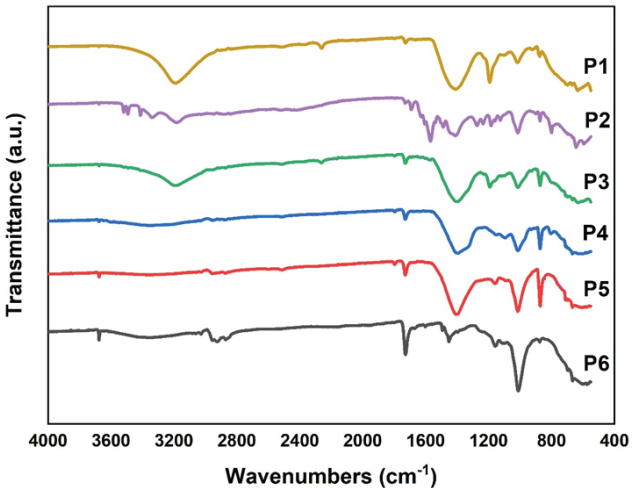

Figure 2. FT-IR spectra of the prepared samples (from P1 to P6).

3.2. LOI Test

Limiting Oxygen Index (LOI) is the most primary, fast and effective technique for investigating the flammability characteristics of the prepared samples [19]. The instrument of the limiting oxygen chamber determines the minimum oxygen requirement to burn these samples, and the results are displayed in Figure 3. The LOI value of P1, which contains no additives and no filling materials, was measured and found to be 24%, and it had the lowest value. When the filling material, $CaCO_3$, was only added to the pure paint, the LOI value of P2 increased and reached an LOI value of 27%. However, when the LOI value of the samples is lower than 28%, these samples are defined as flammable [19]. Thus, the sample P2 was found as flammable. On the other hand, besides $CaCO_3$, with the addition of 5% of H_3BO_3, the LOI value of P3 increased to 30%. In addition, with the increasing amount of H_3BO_3 from 5% to 10%, the LOI value of P4 rose from 30% to 33%. With the addition of 10% of H_3BO_3 and 10% of $C_3H_6N_6$, the LOI value of P5 demonstrated a moderate increase to 39%. Yildirim and Celik examined the flame retardant properties of their prepared composite coatings reinforced with H_3BO_3 according to the pure paint. They reported that whereas the combustion reaction was observed in the coating containing 1% of H_3BO_3, the other coatings including 3%, 5%, 10%, and 15% of H_3BO_3 were not shown any combustion reactions [20]. Furthermore, Figure 3 obviously represents that the LOI value of P6 displayed a surprising boom from 39% to 55%, which contains 20% of H_3BO_3. It can be concluded from the data that P6 is a highly effective flame retardant and can provide excellent flame retardancy to the water-based indoor paints at 20% of H_3BO_3 content. These findings are consistent with the literature where the fire resistance increased when H_3BO_3 is used as a fire retardant material [11,21].

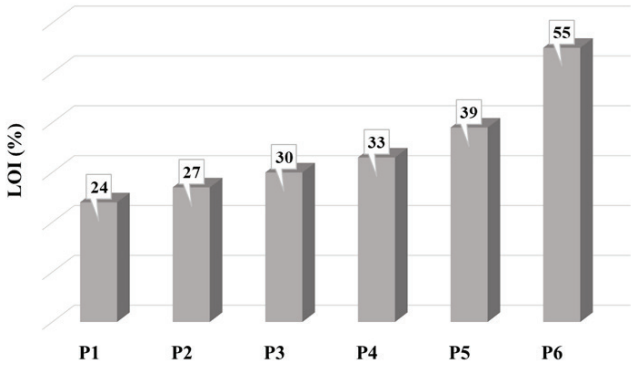

Figure 3. The results of LOI of the prepared paints (from P1 to P6).

3.3. Thermal Analysis

The thermal analysis of all the prepared samples was examined by the thermogravimetric analysis system. Figure 4 shows the TGA curve of P1, which contains no additives and no filling materials, and P2, which contains only $CaCO_3$ as a filling material.

As shown in Figure 4, the first prepared sample, P1, showed about 30% weight loss below 403.7°C; however, P2 sample showed three decomposition stages:

a weight loss of 2% at about 116.1°C by the evaporation of water in the matter, 15% at 400.7°C by losing volatile components in the paint, and a large weight loss of about 40% at about 772.6°C indicating the decomposition of $CaCO_3$ to CaO and CO_2. This was defined by Deepika et al. [22].

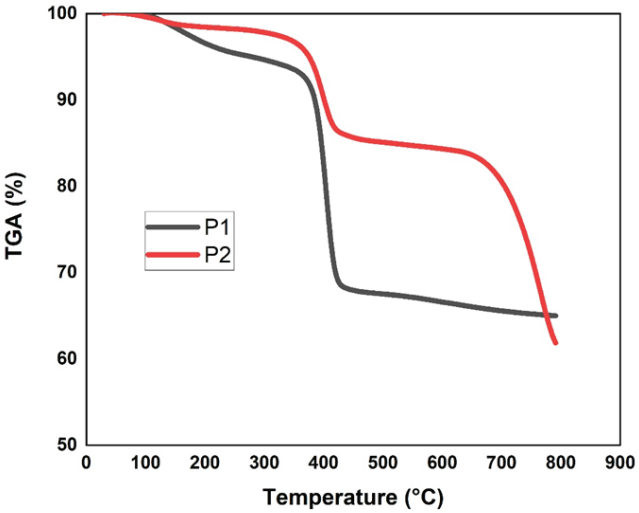

Figure 4. The thermal decomposition patterns for P1 and P2.

Figure 5 shows the TGA curve of the prepared samples from water-based indoor paints that contain different amounts of H_3BO_3 as an additive (P3, P4 and P6). There were three mass-losses in TGA profiles of all the prepared paints. However, the decomposition temperatures and the amounts of weight loss were different due to the different amounts of H_3BO_3 in the prepared paints. When compared to the thermal decomposition patterns of P3, P4 and P6, the first decomposition temperature was obtained as almost 1% at about 155.4°C for P3; however, the first weight losses of P4 and P5 were found at 116.2 and 112.5°C as 2% and 10%, respectively. This slightly weight reduction at an early stage was attributed to the desorption of physically bound water molecules [23]. Then, a sharp decrease in weight loss of P3, P4 and P6 were about 15%, 20% and 30% between 300-400°C, respectively due to the thermal decomposition of the auxiliary chemicals [22]. In addition, when the heating temperature was higher than 720°C, the TGA curve of all the samples demonstrated a final third weight loss due to the thermal decomposition of $CaCO_3$. It can be clearly seen from Figure 5 that the weight loss of the samples increased directly as the amount of H_3BO_3 increased. It can be explained that there might be the conversion reaction of H_3BO_3 to HBO_2 and then into boron oxide (B_2O_3). This result was confirmed by the study carried out by Uner and coworkers [24]. They reported that the H_3BO_3 is transformed into HBO_2 when there is due to dehydration happened below 150°C. Then, metaH_3BO_3 is transformed into B_2O_3 after all water is removed. Whereas crystalline boron oxide melts at a specific temperature (at 450°C), amorphous boron oxide does not, but only softens at 325°C [24]. Therefore, the peaks at 300-400°C may be defined as the transition of crystalline boron oxide to amorphous B_2O_3 [25].

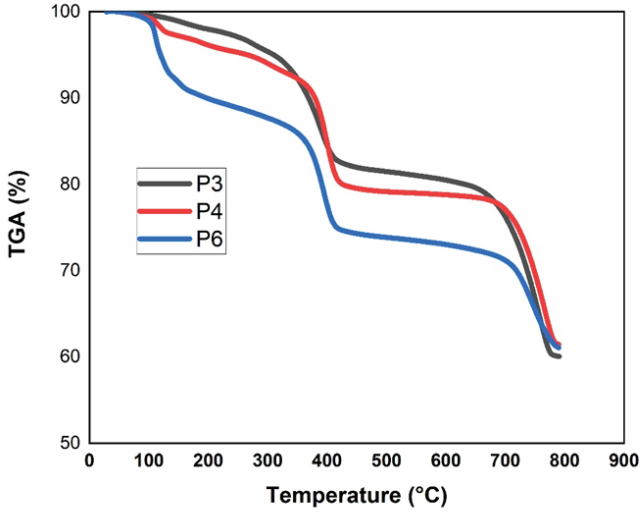

Figure 5. The thermal decomposition patterns for P3, P4 and P6.

On the other hand, Figure 6 illustrates the TGA mass-loss profiles of the prepared samples with H_3BO_3 (P4 and P6), and $H_3BO_3/C_3H_6N_6$ (P5). It can be seen that above 400°C, decomposition of $C_3H_6N_6$ occurs and releases ammonium and water, which then sublimes or decays [26]. Furthermore, the study of Ullah et al. [27] showed that the addition of $C_3H_6N_6$ increased the expansion of a char layer up to 1100% at 375°C while the addition of H_3BO_3 increased to 300%. Therefore, the addition of both additives (H_3BO_3 and $C_3H_6N_6$) as flame retardancy increased the decomposition stages of the samples. This result confirms that $C_3H_6N_6$ has the positive effect on the property of flame retardancy of indoor paints.

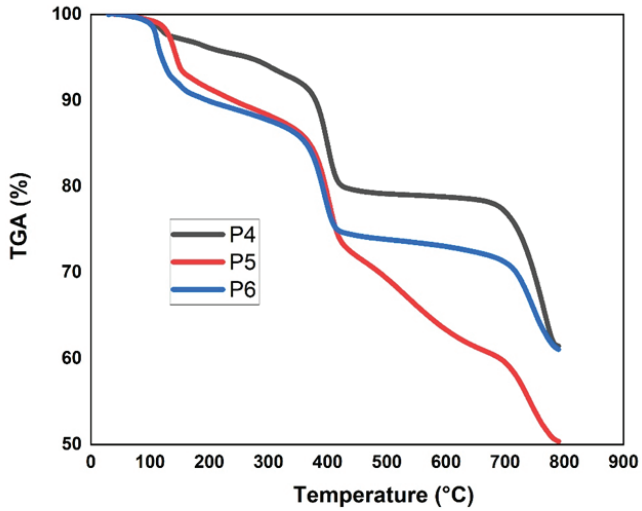

Figure 6. The thermal decomposition patterns for P4, P5 and P6.

Table 2. The maximum decomposition temperatures of each prepared sample.

Sample Code	Decomposition Temperature (°C)			
	Stage 1	Stage 2	Stage 3	Stage 4
P1	192.5	403.7	-	-
P2	116.1	400.7	772.6	-
P3	155.4	273.8	389.4	760.5
P4	116.2	304.3	400.5	764.8
P5	142.7	401.6	513.8	730.9
P6	112.5	147.2	394.6	739.0

4. Conclusions

The indoor paint samples containing $CaCO_3$, $C_3H_6N_6$, and H_3BO_3 were successfully prepared, and the characterization of the prepared paints was performed by FTIR. The addition of these potential flame retardant additives in the paints resulted in an enhancement in the flammability characteristic and thermal property characterized by LOI test and TGA, respectively. The characteristic peaks of $CaCO_3$, $C_3H_6N_6$, and H_3BO_3 were observed in the FTIR spectra of the prepared paints. When H_3BO_3 was added at 20% (w/w) weight fraction, the prepared paint showed more significant enhancement in flammability behavior from 24% to over 55% than that of containing $C_3H_6N_6$ and H_3BO_3. In addition, in the thermogravimetric analysis, the prepared paints containing H_3BO_3 decomposes into boron oxide and water, which suppresses the fire. Based on these results, it can be said that the prepared paint, P6, that contains 20% of H_3BO_3, can be used as a suitable alternative in the water-based indoor paints.

Acknowledgements

The authors are immensely grateful to Ortaç Boya Ltd. Sti. (Ankara, Turkey) for preparing the paints.

References

[1] [1] Hu, X., Zhu, X., & Sun, Z. (2019). Efficient flame-retardant and smoke-suppression properties of MgAl-CO3-LDHs on the intumescent fire retardant coating for steel structures. *Progress in Organic Coatings, 135*, 291-298.

[2] Nasir, K. M., Sulong, N. H. R., Johan, M. R., & Afifi A. M. (2020). Synergistic effect of industrial- and bio-fillers waterborne intumescent hybrid coatings on flame retardancy, physical and mechanical properties. *Progress in Organic Coatings, 149*, 105905.

[3] Triantafyllidis, Z., & Bisby L. A. (2020). Fibre-reinforced intumescent fire protection coatings as a confining material for concrete columns. *Construction and Building Materials, 231*, 117085.

[4] Weiss, K. D. (1997). Paint and coatings: A mature industry in transition. *Progress in Polymer Science, 22*(2), 203-245.

[5] Ceyhan, L. (2001). *Examination of paint industry and sectorial analysis* [M. Sc. thesis, Hacettepe University, Graduate School of Social Science]. Council of Higher Education Thesis Center (Thesis Number 100456).

[6] Cheng, X. W., Wu, Y. X., Huang, Y. T., Jiang, J. R., Xu, J. T., & Guan, J. P. (2020). Synthesis of a reactive boron-based flame retardant to enhance the flame retardancy of silk. *Reactive and Functional Polymers, 156*, 104731.

[7] Eti Maden İşletmeleri Genel Müdürlüğü [Eti Mining Operations General Directorate]. (2014). *Bor Sektör Raporu 2013* [*Boron Sector Report 2013*].

[8] Özkan, Ş. G., Tombal, T. D., Kurşun Ünver, İ., & Osmanlioğlu, A. E. (2016). Bor bileşiklerinin özellikleri, üretimi, kullanımı ve nükleer reaktör teknolojisinde önemi [Properties, production, uses of boron compounds and their importance in nuclear reactor technology]. *Journal of Boron, 1*(2), 86-95.

[9] Yılmaz Aydın, D. (2015). *Synthesis of zinc fluoroborate and usability as flame retardant* [M. Sc. thesis, Gazi University Graduate School of Natural and Applied Science]. Council of Higher Education Thesis Center (Thesis Number 395758).

[10] Özkul, C., Çiftçi, E., Tokel, S., & Savaş, M. (2017). Boron as an exploration tool for terrestrial borate deposits: A soil geochemical study in Neogene Emet-Hisarcık basin where the world largest borate deposits occur (Kütahya-western Turkey). J*ournal of Geochemical Exploration, 173*, 31-51.

[11] Donmez Cavdar, A., Mengeloğlu, F., & Karakus, K. (2015). Effect of boric acid and borax on mechanical, fire and thermal properties of wood flour filled high density polyethylene composites. *Measurement, 60*, 6-12.

[12] Alongi, J., Horrocks, A. R., Carosio, F. & Malucelli, G. (2013). *Update on Flame Retardant Textiles: State of the Art, Environmental Issues and Innovative Solutions* (1st Ed.). Smithers Rapra Publishing. ISBN 9781909030176.

[13] Xu, W., Chen, R., Xu, J., Wang, G., Cheng, C., & Yan, H. (2019). Preparation and mechanism of polyurethane prepolymer and boric acid co-modified phenolic foam composite: Mechanical properties, thermal stability, and flame retardant properties. *Polymers for Advanced Technologies, 30*, 1738-1750.

[14] Uddin, K. M. A., Ago, M., & Rojas, O. J. (2017). Hybrid films of chitosan, cellulose nanofibrils and boric acid: Flame retardancy, optical and thermo-mechanical properties. *Carbohydrate Polymers, 177*, 13-21.

[15] Członka, S., Strąkowska, A., Strzelec, K., Kairytė, A., & Kremensas, A. (2020). Melamine, silica, and ionic liquid as a novel flame retardant for rigid polyurethane foams with enhanced flame retardancy and mechanical properties. *Polymer Testing, 87*, 106511.

[16] Ortiz-Herrero, L., Cardaba, I., Setien, S., Bartolomé, L., Alonso, M. L., & Maguregui, M. I. (2019). OPLS multivariate regression of FTIR-ATR spectra of acrylic paints for age estimation in contemporary artworks. *Talanta, 205*, 120114.

[17] Germinario, G., van der Werf, I. D., & Sabbatini, L. (2016). Chemical characterisation of spray paints by a multi-analytical (Py/GC–MS, FTIR, μ-Raman) approach. *Microchemical Journal, 124*, 929-939.

[18] Zhang, J., Koubaa, A., Xing, D., Liu, W., Wang, Q., Wang, X. M., & Wang, H. (2020). Improving lignocellulose thermal stability by chemical modification with boric acid for incorporating into polyamide. *Materials and Design, 191*, 108589.

[19] Saba, N., Jawaid, M., Alrashed, M. M., & Alothman, O. Y. (2019). Oil palm waste based hybrid nanocomposites: Fire performance and structural analysis. *Journal of Building Engineering, 25*, 100829.

[20] Yildirim, S., & Celik, E. (2020). Production and characterization of the halogen-free and nanostructured flame retardant reinforced composite coatings. *Journal of the Australian Ceramic Society, 56*, 683-695.

[21] Boran Torun, S., Donmez Cavdar, A., & Ozdemir, T. (2020). The synergistic effect of intumescent coating containing titanium dioxide and antimony trioxide onto spruce and alder wood species. *Journal of Building Engineering, 31*, 101407.

[22] Deepika, Hait, S. K., Christopher, J., Chen, Y., Hodgson, P., & Tuli, D. K. (2013). Preparation and evaluation of hydrophobically modified core shell calcium carbonate structure by different capping agents. *Powder Technology, 235*, 581-589.

[23] Abeywardena, M. R., Elkaduwe, R. K. W. H. M. K., Karunarathne, D. G. G. P., Pitawala, H. M. T. G. A., Rajapakse, R. M. G., Manipura, A., & Mantilaka, M. M. M. G. P. G. (2020). Surfactant assisted synthesis of precipitated calcium carbonate nanoparticles using dolomite: Effect of pH on morphology and particle size. *Advanced Powder Technology, 31*(1), 269-278.

[24] Uner, I. H., Deveci, I., Baysal, E., Turkoglu, T., Toker, H., & Peker, H. (2016). Thermal analysis of oriental beech wood treated with some borates as fire retardants. *Maderas: Ciencia y Tecnologia, 18*(2), 293-304.

[25] Sevim, F., Demir, F., Bilen, M., & Okur, H. (2006). Kinetic analysis of thermal decomposition of boric acid from thermogravimetric data. *Korean Journal of Chemical Engineering, 23*(5), 736-740.

[26] Nyambo, C., Kandare, E., & Wilkie, C. A. (2009). Thermal stability and flammability characteristics of ethylene vinyl acetate (EVA) composites blended with a phenyl phosphonate-intercalated layered double hydroxide (LDH), melamine polyphosphate and/or boric acid. *Polymer Degradation and Stability, 94*(4), 513-520.

[27] Ullah, S., Ahmad, F., & Yusoff, P. S. M. M. (2013). Effect of boric acid and melamine on the intumescent fire-retardant coating composition for the fire protection of structural steel substrates. *Journal of Applied Polymer Science, 128*, 2983-2993.